ulm university universität ulm

Three-dimensional InGaN/GaN based Light Emitters with Reduced Piezoelectric Field

DISSERTATION

to obtain the academic degree of

DOKTOR-INGENIEUR

(DR.-ING.)

from the Faculty of Engineering and Computer Science
Ulm University

by

Junjun Wang
from Huaian, Jiangsu, China

Regensburg, 20, February, 2018

1st Referee:	Prof. Dr. Ferdinand Scholz
2nd Referee:	Prof. Dr. Andreas Hangleiter
Dean of the Faculty:	Prof. Dr. Frank Kargl
Date of Oral Exam:	12, December, 2017

Parts of this dissertation have already been published in the journal articles below and the corresponding permission to reuse in a dissertation has been obtained from publishers:

J. Wang, D. Zhang, R.A.R. Leute, T. Meisch, D. Heinz, I. Tischer, M. Hocker, K. Thonke, F. Scholz. *InGaN/GaN based semipolar green converters.* J. Cryst. Growth **370**, 120, 2013.

J. Wang, Y. Gao, S. Alam, F. Scholz. *Mg doping of 3D semipolar InGaN/GaN-based light emitting diodes.* Phys. Status Solidi A **211**, 2645, 2014.

J. Wang, T. Meisch, D. Heinz, R. Zeller, F. Scholz. *Internal quantum efficiency and carrier injection efficiency of c-plane,* $\{10\bar{1}1\}$ *and* $\{11\bar{2}2\}$ *InGaN/GaN-based light-emitting diodes.* Phys. Status Solidi B **253**, 174, 2016.

Contents

1. Introduction

The first high-brightness blue light emitting diode (LED) was developed in 1993 thanks to the realization of p-conductivity of Mg-doped GaN grown in MOVPE (metalorganic vapor phase epitaxy) followed by low energy electron irradiation [Ama89] or thermal annealing [Nak92]. This invention was honored by the Nobel Prize in physics for the year 2014. LEDs have many applications in full color displays and the electricity-thirsty fields like automobile head lamps, mobile phone display, LCD backlight and so on. The spectrum of a single LED is narrower than the solar spectrum in the range of visible light. Phosphor powder is most often used to convert the blue light of the GaN-based LED chip partially to yellow and the mixture of the remaining LED light and the downconverted yellow one is perceived as white light by human eyes. During the last years, such commercial LEDs packed with phosphor powder have been replacing the traditional light sources for general lighting, e.g. incandescent and fluorescent lamps, due to their high efficiency and long lifetime. Color rendering index (CRI) is a quantitative measure of the ability of the light sources to reveal the color of any objects as compared to the sunlight. The usage of a combination of phosphor powders enables CRI $>$ 80 [Mil05]. However, LEDs emitting all the primary colors of red, blue and green would be the eventual solution for white light source with a dynamically-controlled CRI as well as full color displays and projectors. Nowadays, it is still challenging to achieve efficient operation of green devices.

Whereas III-nitrides and III-phosphides are suitable material systems for the fabrication of blue and red LEDs, respectively, the efficiency of the III-nitride LEDs decreases with increasing emission wavelength and gets quite low at the emission wavelength of the green light. The III-phosphide LEDs suffer from the mirrored problem at the long wavelength side, not as a good candidate for the green light emission either. In a word, the material system for efficient green emitters is missing. This phenomenon is known as *the green gap*.

The polar character of the nitride semiconductors is discussed as one main reason for the green gap by the scientific community. Typically, a heterostructure of InGaN/GaN quantum wells (QWs) is employed as the active region of III-nitride LEDs. In such structures, strain occurs in the InGaN/GaN QWs due to the lattice mismatch leading to huge internal electric fields. Consequently, electrons and holes in the QWs are locally separated resulting in a reduced recombination probability. In order to avoid the huge internal electric field in the InGaN/GaN QWs, many groups are making efforts to fabricate semipolar/nonpolar structures following different approaches. The investigations

go mainly in three directions. One is to grow GaN layers on foreign substrates, e.g., $\{11\bar{2}0\}$ GaN on r-plane sapphire [Kim13, Jeo13]. However, the material quality is inferior compared to that of the standard c-plane GaN. The nonradiative recombination leads to the bad performance of the devices again. Alternatively, GaN substrates sliced from the c-plane GaN bulk crystal grown by HVPE (Hydride Vapor Phase Epitaxy) are employed for the nonpolar or semipolar GaN homoepitaxy which demonstrates great potential in crystal quality improvement [Fuj08, Zha10a, Zha10b, Kos10, Zha11]. However, the GaN substrate is not cost-effective and its size is fairly small. Two methods are included in the third investigation direction. Either three-dimensional (3D) GaN structures are obtained via Selective Area Epitaxy (SAE) on (0001)-oriented GaN with the semipolar facet as the stable surface [Wun06] or GaN growth starts from c-plane-like sidewall of the structured sapphire and coalesces into a semipolar planar surface [Sch12, Uch13]. Both methods take the experience of the GaN growth on c-plane sapphire and are suitable for full wafer fabrication. This work focuses on the 3D GaN structures realized by SAE whereas the semipolar planar GaN structure on patterned sapphire is only discussed in chapter 7 in terms of LED analysis by ABC model fitting.

Obviously, reasonable electrical performance is crucial for high efficiency of the semipolar LEDs besides the advantage of reduced internal electrical field in the QWs. It is addressed in Chapter 4 how the electrical properties of the semipolar LED are affected by each individual functional layer: epi-mask, spacer (the intentionally undoped layer lying directly on top of the active region), main p-GaN layer and p-contact layer. Any current flowing through the epi-mask bypasses the pn-junction. The epi-mask is checked exprimentally to confirm its electrical insulation. Mg atoms in the p-(Al)GaN layers diffuse backward into the spacer approaching the active region at the high temperature during the crystal growth leading to a diffusive interface of the Mg profile. Therefore, the spacer layer should be thick enough to prevent the Mg atoms from diffusing into the active region acting as nonradiative recombination centers and meanwhile not too thick to reduce hole injection efficiency. Therefore, we have optimized the spacer layer for our semipolar LEDs. Good conductivity of both, n-type and p-type GaN is essential to obtain effcient GaN-based LEDs. The doping problem proves to be more challenging in the case of p-type GaN. We optimized the Mg concentration in the main p-GaN layer to achieve high efficiency of the semipolar LEDs by varying the ratio between precusors Cp_2Mg and TMGa. The p-type contact performance was improved by excessive Mg doping in the p-contact layer. What is more, we have tried to determine the Mg concentration of 3D semipolar p-GaN, both of the main p-GaN layer and the p-contact layer.

Injection efficiencies of electrons and holes differ strongly from the n- and the p-side of the diode. The droop effect gets severe since most of the charge carriers accumulate in the QW closest to the p-GaN causing high carrier density there. This issue can be circumvented by optical excitation of carriers leading to the idea of luminescence conversion structures with green light emitting InGaN QWs optically pumped with a

highly efficient blue LED which will be discussed in chapter 5. In this work, we investigate luminescence conversion structures with semipolar InGaN/GaN QWs based on our 3D inverse pyramidal structure. The facet formation of the GaN inverse pyramids, $\{10\bar{1}1\}$, $\{11\bar{2}2\}$ or coexistence of both facets, and its effect on the QW quality is discussed. These structures have been mainly characterized by an optical transmission experiment, which enables the determination of the conversion ratio. Moreover, degraded InGaN material quality with high indium content plays also an important role for the low QW efficiency. We enhanced the green emission of the conversion structure under optical excitation focusing mainly on the optimization of the InGaN growth conditions.

Despite of systematic investigations of our semipolar LEDs, the electroluminescence (EL) output power of the semipolar LED is still inferior as compared to the c-plane ones. Two LED evaluation methods, fitting of the EL data according to the well-known ABC model and electron beam induced current (EBIC) are introduced in Chapter 6 to find out reasons. By analyzing the EL data, one acquires more information beyond the EL output power, such as the internal quantum efficiency (IQE) and the carrier injection efficienc (CIE). Therefore, optical performance of the QWs and charge carrier transport into the QWs can be evaluated separately. The analysis of EBIC applied in a SEM is a powerful LED analysis tool, capable to reveal the position and the material quality of the buried pn-junction as well as the minority carrier properties [Han81, Don83]. Two important aspects of the LED structure, the pn-junction quality and the QW quality, are collected enabling a good understanding which issue is essential to improve the LED performance.

2. Basics of Group III-Nitrides

III-nitrides are suitable materials to realize LEDs for green light emission based on their material properties. It is explained in this chapter which factors affect the emission wavelength of InGaN/GaN QWs as the luminescence core of our LEDs. However, we are facing two challenges to achieve high-efficient green LEDs: reduce the defect density and suppress the piezoelectric field within the QWs. The origin of different types of defects and how they deteriorate the LED performance will be discussed in this chapter. Owing to the polar character of the nitride semiconductors, the strain in the InGaN/GaN QWs leads to an internal electrical field resulting in a local separation of electrons and holes, reducing their radiative recombination probability and hence decreasing the InGaN/GaN QW efficiency. This motivates our investigation of semipolar LEDs with the active region deposited on the crystal facets with reduced piezoelectric polarization.

2.1. Crystal structure

There are three types of crystal structures for III-nitrides: wurtzite, zincblende and rocksalt. The wurtzite structure is thermodynamically the most stable for bulk III-nitrides. Throughout this work, the crystal structure of all the samples is the wurtzite type. Such a crystal structure has a hexagonal unit cell and therefore is described by the in-plane lattice constant a and the out-of-plane lattice constant c (Fig. 2.1). It consists of two inter-penetrating hexagonal close packed (HCP) sublattices, each with one type of atoms offset along the c-axis by $3/8$ of the cell height, i.e., $3c/8$. The ratio between the lattice constants $c/a = \sqrt{8/3} = 1.633$ if this crystal structure is centrosymmetric. However, the ratio of the lattice constants c/a is 1.626, 1.601 and 1.609 for GaN, AlN and InN with the wurtzite structure, respectively. (Table 2.1). The wurtzite structure lacks inversion symmetry firstly giving rise to the piezoelectric polarization of materials with the wurtzite structure, responsible for the inferior quantum efficiency of high indium-content InGaN/GaN QWs. This will be discussed in details in section 2.6.2 as an important motivation of this work. Secondly, it becomes necessary to distinguish the (0001) and $\left(000\bar{1}\right)$ planes which have different chemical properties. Typically MOVPE epitaxial growth using an AlN nucleation layer enables the fabrication of high quality GaN layers grown in the $\langle 0001 \rangle$ orientation.

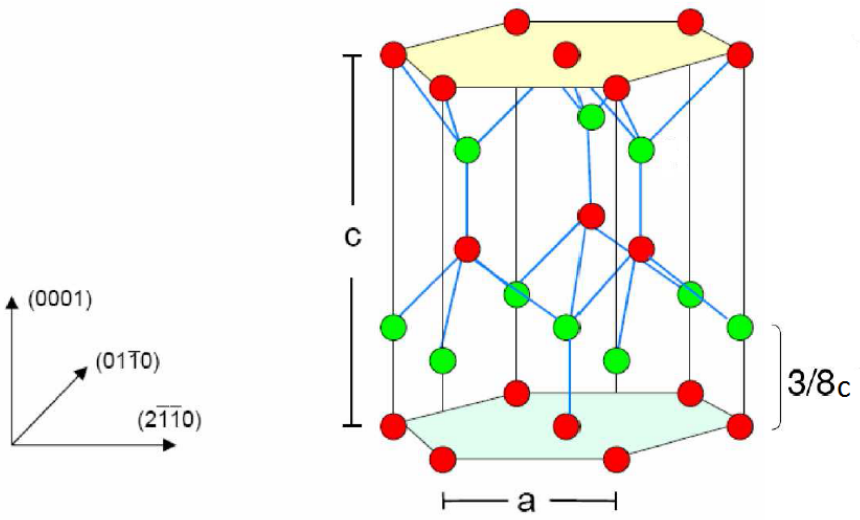

Figure 2.1.: The stick and ball representation of the wurtzite structure. The group-III atoms are represented by red balls whereas the nitrogen atoms by the green ones.

Table 2.1.: Crystal lattice constants for group III-nitride binaries at room temperature (RT) [Vur03].

Property	Symbol (unit)	InN	GaN	AlN
in-plane lattice constant	a (nm)	0.3545	0.3189	0.3112
out-of-plane lattice constant	c (nm)	0.5703	0.5185	0.4982

In the hexagonal system, 4 indices are used to denote the crystalline planes, i.e., $hkil$. Three vectors, $\vec{a_1}$, $\vec{a_2}$ and $\vec{a_3}$ corresponding to h, k, i, respectively, lie in the basal plane and are oriented with an angle of 120 ° to each other. Consequently h, k and i are not independent of each other but follow the relationship $-i = h + k$. In this way, equivalent crystal planes are identified by the permutation of the first three indices. Important planes for this work are shown in Fig. 2.2: the polar (0001) plane (c-plane) as the surface plane of the conventional III-nitride films, the nonpolar $\{10\bar{1}0\}$, $\{11\bar{2}0\}$ planes perpendicular to the c-plane and the semipolar $\{10\bar{1}1\}$, $\{11\bar{2}2\}$ planes with a tilting angle of ∼60 °C according to the c-plane. "polar", "semipolar" and "nonpolar" are referred to the piezoelectrical polarity of variable crystal planes.

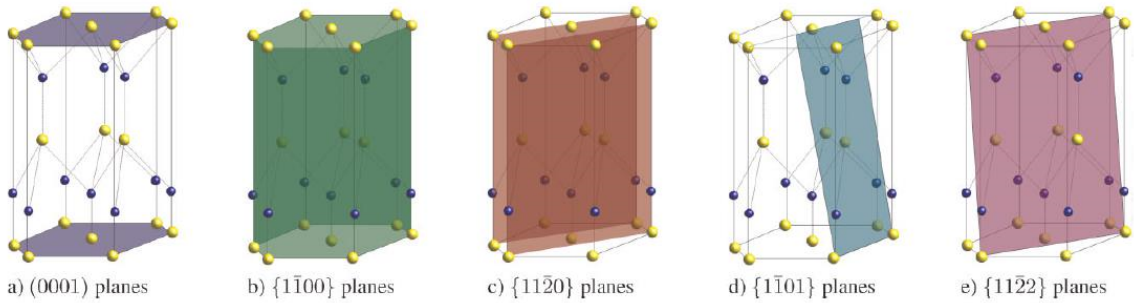

Figure 2.2.: Schematic drawing of the examplary crystal planes in wurtzite structure [Sch11b].

2.2. Band structure

The band structure helps to understand the optoelectronic properties of semiconductors. The band structure of wurtzite GaN within the first Brillouin zone is shown in Fig. 2.3 (left) calculated by the $k \cdot p$ method. The first Brillouin zone is the corresponding Wigner-Seitz cell in the reciprocal space containing one lattice point in the center.

The optoelectronic properties of the semiconductors are mainly dependent on a small portion of the band structure close to the minimum of the conduction band and the maximum of the valence band. The maximum of the valence band stays at the Γ point ($k_x = 0, k_y = 0, k_z = 0$) in the reciprocal space. In most of the compound semiconductors, the minimum of the conduction band occurs at the same point as well. Such a semiconductor is denoted as direct semiconductor interacting strongly with photons. Therefore, it is well suitable for light emission devices like LEDs or LDs. In contrary, the minimum of the conduction band occurs at some other points than the Γ point in an indirect semiconductor. All of the element semiconductors belong to this group.

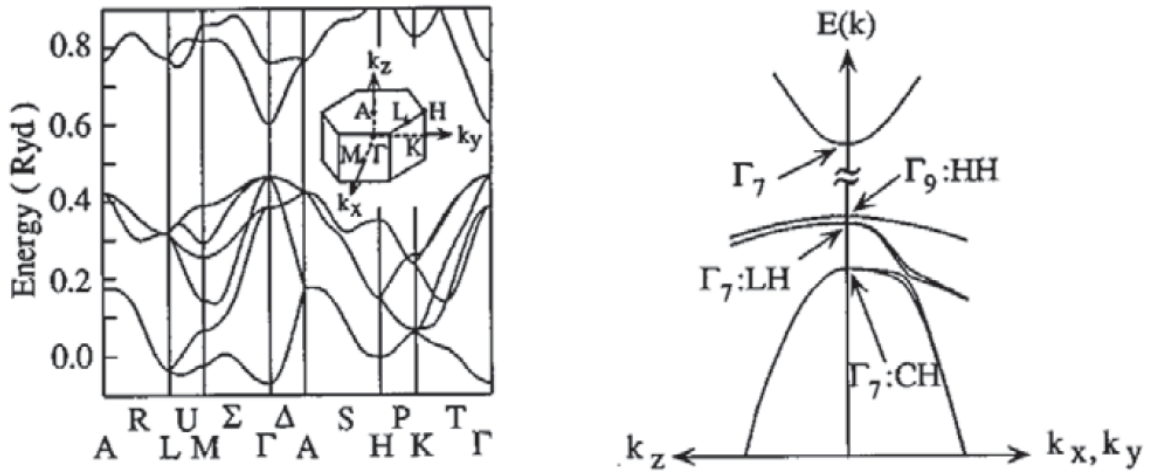

Figure 2.3.: The band structure of wurtzite GaN calculated according to the pseudopotential method with the part close to the Γ point amplified [Blo74] (right).

In wurtzite GaN, the conduction band follows the parabolic dispersion relation around the Γ point (Fig. 2.3, right). The three degenerated valence bands at $\vec{k} = 0$ split into the heavy hole (HH) and light hole (LH) bands and a split-off (SO) band by the spin-orbit interaction and the crystal potential splitting. The three valence bands are anisotropic along the $k_{x,y}$ and k_z directions due to the low symmetry of the wurtzite structure.

The band gap E_g varies with the temperature T which can be described by Varshni's formula:

$$E_g(T) = E_g(0\,\mathrm{K}) - \frac{\alpha_\mathrm{v} \cdot T^2}{\beta_\mathrm{v} + T} \tag{2.1}$$

where α_v is an empirical constant and β_v is associated with the Debye temperature. Above the Debye temperature, the band gap changes almost linearly with the temperature due to linear changes of lattice parameters and electron-phonon interaction [Pow93]. The band gap E_g and the Varshni parameters α_v and β_v for group III-nitride binaries are listed in Table 2.2.

2.3. Ternary alloy

Ternary or even quaternary alloys can be formed based on the group III-nitride binaries GaN, AlN and InN. This opens many possibilities to choose material properties suitable for different applications. The material properties, e.g., the lattice constant and the band gap, of the ternary alloy can be determined based on those of the binaries.

Table 2.2.: Band gap E_g, Varshni parameters α_v, β_v and bowing parameter b for group III-nitride binaries [Pip07].

	E_g (eV) ($T = 0\,\mathrm{K}$)	E_g (eV) ($T = 300\,\mathrm{K}$)	α_v (meV/K)	β_v (K)	b (eV)
AlN	6.10	6.00	2.63	2082	
GaN	3.510	3.437	0.914	825	
InN	0.69	0.608	0.414	154	
AlGaN					0.8
GaInN					1.4
AlInN					3.4

2.3.1. Lattice constant

The lattice constant of the alloys can be determined by the linear interpolation from those of the binaries. *Vegard's law* describes the relation mathematically:

$$a_{A_xB_{1-x}N} = x \cdot a_{AN} + (1-x) \cdot a_{BN} \tag{2.2a}$$

$$c_{A_xB_{1-x}N} = x \cdot c_{AN} + (1-x) \cdot c_{BN} \tag{2.2b}$$

where A and B are the group III elements and a and c the in-plane lattice constant and the out-of-plane one, respectively.

The lattice constant of InGaN is larger than that of GaN. Therefore, strain is induced within the InGaN/GaN QWs in the case of the pseudomorphic growth leading to piezoelectric polarization which will be discussed in section 2.6.2.

2.3.2. Band gap

The band gap of the alloys needs to be deduced from those of the binaries via a quadratic relation:

$$E_{g,A_xB_{1-x}N} = x \cdot E_{g,AN} + (1-x) \cdot E_{BN} - x \cdot (1-x) \cdot b \tag{2.3}$$

where E_g stands for the band gap and b the bowing parameter. Please refer to Table 2.2 for E_g and b values of group III-nitride binaries AlN, GaN and InN.

According to Equ. 2.2 and (2.3), the corresponding in-plane lattice constant a and band gap E_g of the ternaries are calculated (Fig. 2.4). The band gap of these ternaries covers the whole visible spectrum and parts of the infrared (IR) and ultraviolet (UV) spectra. Typically, AlGaN is applied as the active region of UV light emitters

whereas InGaN in the spectral range from violet until yellow light depending on the composition.

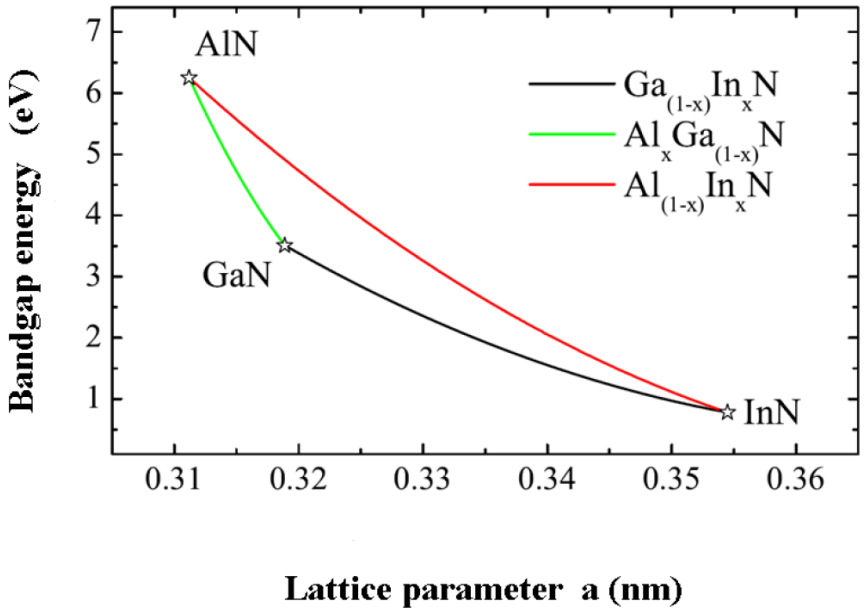

Figure 2.4.: The relation between band gap E_g and the lattice constant a for group III-nitride ternaries at RT [Fik14].

2.4. Emission wavelength of InGaN/GaN QWs

InGaN/GaN QWs are employed as luminescence core of the LEDs emitting green light. We will discuss in this section how the emission wavelength of the InGaN/GaN QWs can be determined.

The energy of the emitted photons E_{ph} generated via the radiative recombination determines the emission wavelength λ according to

$$E_{\mathrm{ph}} = \frac{hc_0}{\lambda} \tag{2.4}$$

with h and c_0 denoting the Planck constant and the speed of light in vacuum, respectively, and consequently the light color of the light emitting devices. A variety of factors affects the photon energy. Firstly, the photon energy is dependent on the band gap of the InGaN bulk material with the same material composition as the InGaN quantum film. Secondly, quantization occurs when the InGaN film is thin enough (typically <10 nm). Due to the energy quantization, the charge carriers can only stay at discrete energy levels rather than the band edge. The lowest energy levels

of electrons and holes are apart from the band edges, shifted into the conduction band and the valence band, respectively. The photon energy is equal to the energy difference between the lowest energy levels of the electrons and holes, affected by the quantization obviously. Thirdly, the photon energy gets reduced by the internal electrical field within the QWs (described as QCSE in section 2.6.2).

2.4.1. Band gap

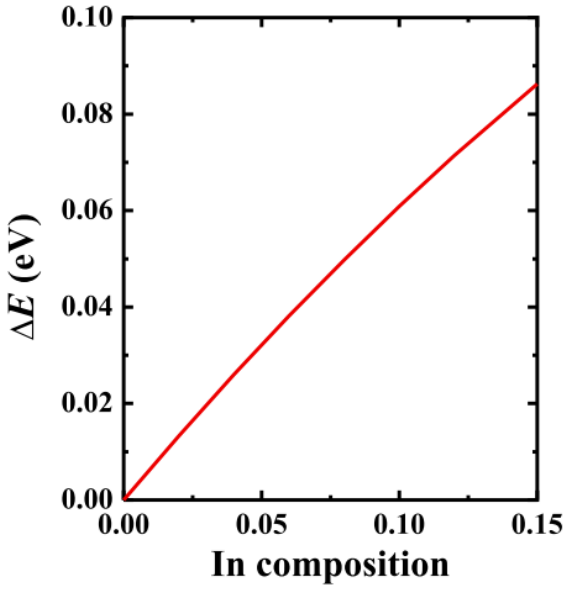

Figure 2.5.: Calculated band-gap change purely due to strain effects (section 2.5) in an $In_xGa_{1-x}N$ alloy grown pseudomorphically on *c*-plane GaN [Yan14].

The band gap of the $In_xGa_{1-x}N$ alloy is dependent on the indium composition x and the bowing parameter b according to a quadratic relation Equ. 2.3. Besides, it is modified by the strain as well. The biaxial compressive strain increases with increasing indium composition in the $In_xGa_{1-x}N$ alloy grown pseudomorphically on *c*-plane GaN leading to a rising transition energy in a nonlinear relation according to the calculation by Yan *et al.* (Fig. 2.5).

2.4.2. Quantization

The charge carriers are confined within the QW, a potential well formed by sandwiching the InGaN quantum film of a low band gap with another material, e.g. GaN of a high band gap. When the thickness of the active region becomes comparable to the de Broglie wavelength of the charge carriers, the energy is quantized within QWs. The

discrete energy levels can be calculated by the time-independent Schrödinger equation only with the variable along the x coordinate perpendicular to the QW:

$$\frac{p^2}{2m^*}\Psi + V(x)\Psi = (E - \epsilon_0)\Psi \tag{2.5}$$

with $\Psi(x)$ representing the wavefunction of the charge carriers, m^* the effective mass, E the allowed energy level over the band edge, p the momentum operator, ϵ_0 the band edge of the respective band and $V(x)$ the potential energy function varying only slowly with the dimension x as compared to the crystal potential (the strong fluctuation of the crystal potential is solved by m^*). $|\Psi(x)|^2$ describes the probability for the charge carrier to appear at a certain location x.

The solution of the Schrödinger equation leads to discrete specific energies (eigenvalues). When infinite barrier is assumed for a rectangular QW, the lowest eigenvalue is obtained as

$$E_0 = \frac{\pi^2\hbar^2}{2m^*d^2} \tag{2.6}$$

with d denoting the QW thickness and $\hbar = \frac{h}{2\pi}$ the reduced Planck constant. E_0 increases with decreasing QW thickness. Therefore, the emitted photo energy, as the energy difference of the lowest energy levels in the conduction band and the valence band, increases with decreasing QW thickness leading to a shorter emission wavelength.

The density of states (DOS) is the state number per unit energy and per unit volume. The DOS in bulk materials is proportional to $E^{\frac{1}{2}}$. The possible energy states are continuous. In the case of InGaN/GaN QWs, the movement of charge carriers is confined along the direction perpendicular to the QW. The DOS of the 2D electrons $\rho^{2D}(E)$ within the QWs stays constant when the energy E is larger than the ground state energy E_0:

$$\rho^{2D}(E) = \frac{m^*}{\pi\hbar^2} \quad E \geq E_0 \tag{2.7}$$

When more than one state exists for a certain QW, the total density of states can be written as

$$\rho^{2D}(E) = \frac{m^*}{\pi\hbar^2}\Sigma_n\sigma(E - E_n) \tag{2.8}$$

where E_n are the quantized energy levels and $\sigma(E - E_n)$ is the step function. Such discrete energy states enable energetically-defined optical transitions.

2.4.3. Electrical field

When an electrical field F is applied to the InGaN/GaN QWs, the band edge within the QWs is tilted confining the electrons and holes at the triangular corners of the conduction band and the valence band, respectively. The shifts of the ground-state energy level induced by the electrical field F can be calculated based on first-order perturbation theory as [Bul06]

$$E^0_{e,h} = \frac{512 m_{e,h} e^2 F^2 d^4}{243 \pi^6 \hbar^2 \chi^2} \tag{2.9}$$

where e is the elementary charge, d the QW thickness and the factor χ describes the electrical field screening by the charge carriers in the QW. Therefore, electrical field changes the emission wavelength of the InGaN/GaN QWs which flows to the core theory of this dissertation (section 2.6.2).

As an example, 20 % indium composition is required to achieve the emission wavelength of ∼540 nm on the c-plane taking the piezoelectric polarization and the energy quantization with the QW into account (Assumptions: QW thickness of 2.5 nm and piezoelectric field of 2 MV/cm [Jho01]). An even higher indium content is necessary for the InGaN/GaN QWs on the semipolar or nonpolar facets due to the reduced/vanished piezoelectric field. However, it is very challenging to achieve good material quality of InGaN with a high indium composition. It is one of the goals of this work to improve the material quality of the InGaN/GaN QWs for green emission (hapter 5).

2.5. Strain

Due to the lack of inversion symmetry, the wurtzite III-nitrides have piezoelectric properties: strain leads to piezoelectric polarization which is detrimental for the QW efficiency. The quantitative relation between strain and piezoelectric polarization will be discussed in the next section. Strain in heterostructures is mainly caused by two factors, lattice mismatch and thermal expansion coefficient mismatch.

2.5.1. Lattice mismatch

When a thin layer of single-crystal material is deposited on a single-crystal substrate with a different lattice constant in epitaxy, the epi-layer is forced to keep the in-plane lattice structure of the substrate: pseudomorphic growth. Lattice mismatch is accommodated by in-plane strain $\epsilon_{\parallel}$:

$$\epsilon_{\parallel} = \frac{a_{\mathrm{epi}} - a_{\mathrm{sub}}}{a_{\mathrm{sub}}} \tag{2.10}$$

where a_{epi} and a_{sub} are the lattice constants of the epi-layer and the substrate in equilibrium, respectively. Compressive strain occurs when $a_{\mathrm{epi}} > a_{\mathrm{sub}}$ whereas tensile strain is invoked when $a_{\mathrm{epi}} < a_{\mathrm{sub}}$. A vertical strain $\epsilon_{\perp}$ along the out-of-plane crystal direction arises correspondingly and can be calculated by Poisson's ratio ν of a certain material according to

$$\nu = -\frac{\epsilon_{\parallel}}{\epsilon_{\perp}}. \tag{2.11}$$

The lattice mismatch of GaN on different substrates varies with substrate materials and orientations ranging between $\sim 2\,\%$ and above $20\,\%$. It is as high as $16\,\%$ between c-GaN and c-sapphire which is the most common growth orientation for GaN.

2.5.2. Thermal expansion coefficient mismatch

The epitaxy growth temperature and the operation temperature for III-nitrides typically differ by more than $1000\,^{\circ}\mathrm{C}$. Strain induced by the thermal expansion mismatch is not really negligible and can be calculated as

$$\epsilon_{\mathrm{therm}} = (\alpha_{\mathrm{epi}} - \alpha_{\mathrm{sub}}) \times \Delta T \tag{2.12}$$

where α indicates the thermal coefficient of the two connected materials and ΔT the difference between the epitaxy growth temperature and the operation temperature. The typical value of $\epsilon_{\mathrm{therm}}$ between GaN and the sapphire substrate is about $0.1\,\%$ [Her09] which is negligible in comparison to the strain caused by the respective lattice mismatch.

2.5.3. Strain relaxation

Obviously, the strain energy rises with an increasing thickness of the epi-layer. Whenever it exceeds a certain value, the strain will be released. The respective thickness of the epi-layer is defined as *critical thickness*. The strain in a c-plane InGaN/GaN active region is typically released via formation of misfit dislocations lying in the plane of the heterostructure interface [Mei07b, Mei07a, Liu06b, Liu06a] or V-pits (Fig. 2.6, right). In contrary, the strain relaxation is realized via the formation of BSFs in the case of nonpolar InGaN/GaN active region, more precisely, the formation of SF type I_1 by terminating, e.g., a B plane (Fig. 2.7). Both of these two strain relaxation mechanisms exist for the semipolar InGaN/GaN active region [Wu11, Tya09]. Moreover, it was recently found that the semipolar InGaN/GaN active region releases strain via the formation of I_2-type BSFs [Li17].

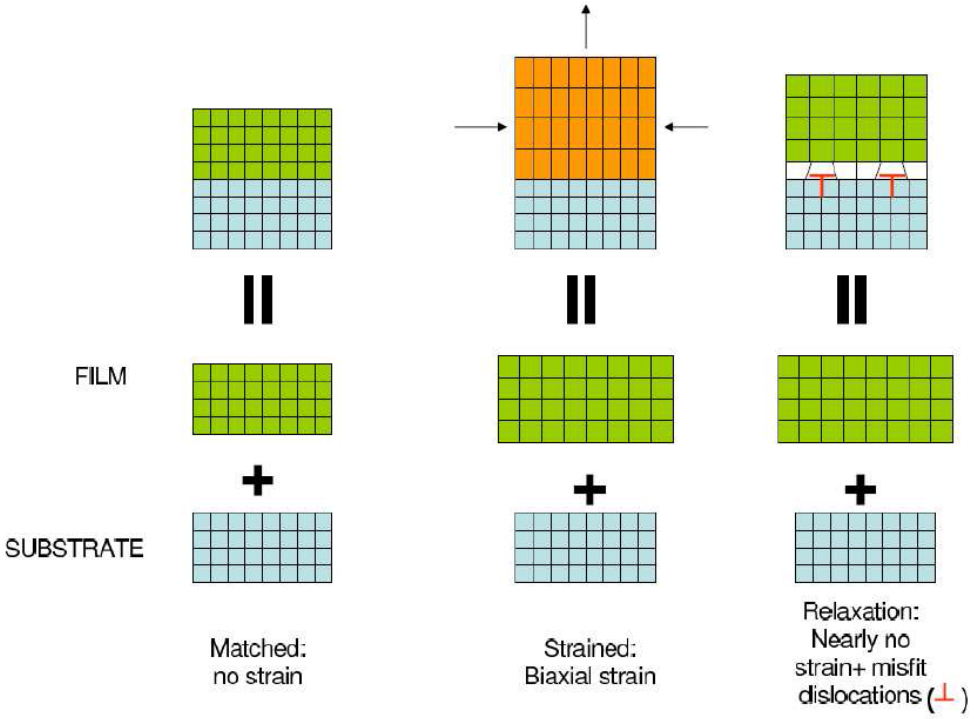

Figure 2.6.: Schematic illustration of lattice-matched (left), strained (middle) and relaxed (right) heteroepitaxial structures. The strain is released via the formation of misfit dislocations in the structure on the right side [For08].

BSFs running through the active region up to the device surface would allow leakage current to flow across the pn-junction of LEDs without entering the QWs. The critical thickness decreases with increasing indium content required for the green emission of the InGaN/GaN QWs, as another intrinsic problem leading to the green gap.

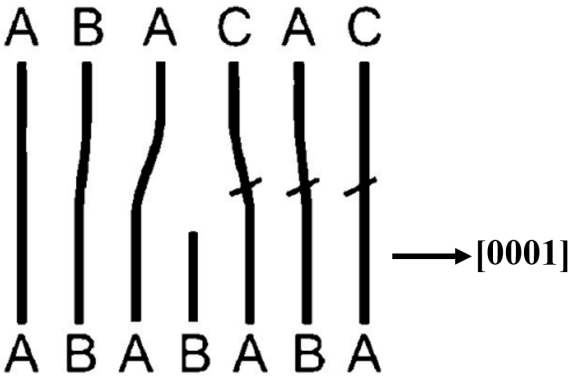

Figure 2.7.: Schematic illustration of strain relaxation in a non-polar hetero structure via formation of basal-plane stacking faults [Fis09].

2.6. Polarization

Polar character of wurtzite III-nitrides motivated the basic idea of this work, to employ 3D $\{10\bar{1}1\}$ InGaN/GaN-based structure.

2.6.1. Spontaneous and piezoelectric polarization

The partial ionicity of the chemical bonds in III-nitrides causes a dipole moment between each two nearest atoms pointing from the atom of the group III element to the nitrogen atom. The III-nitride wurtzite crystal structure is distinguishable by looking along the c-axis from opposite directions. Therefore, the dipole moments do not cancel out along the c-axis when integrating over the crystal volume leading to the existence of spontaneous polarization $\vec{P}_{\mathrm{sp}}$.

Table 2.3.: Calculated spontaneous polarizations of GaN, InN and AlN [Vur03].

	GaN	InN	AlN
P_{sp} (Cm^{-2})	-0.034	-0.042	-0.090

To calculate the electrostatic field $\vec{F}_{\mathrm{sp}}$ induced by the spontaneous polarization, the

following equation is required:

$$\vec{F}_{\mathrm{sp}} = \frac{\vec{P}_{\mathrm{sp}}}{\epsilon_0 \epsilon} \tag{2.13}$$

where $\vec{P}_{\mathrm{sp}}$ is the spontaneous polarization, ϵ the dielectric constant of the material for which the field is calculated and ϵ_0 the vacuum permittivity. Both of ϵ and ϵ_0 are positive. Therefore, the negative sign of the spontaneous polarization of GaN, InN and AlN listed in Table 2.3 indicates that the electrostatic field $\vec{F}_{\mathrm{sp}}$ induced by the spontaneous polarization is negative, i.e., oriented along the crystal direction $\langle 000\bar{1} \rangle$.

When the III-nitride layer is strained due to lattice mismatch or thermal expansion mismatch at the heterojunctions, the distortion of the crystal structure affects the partially-ionized chemical bonds leading to piezoelectric polarization $\vec{P}_{\mathrm{pz}}$.

Mathematical description of piezoelectric polarization

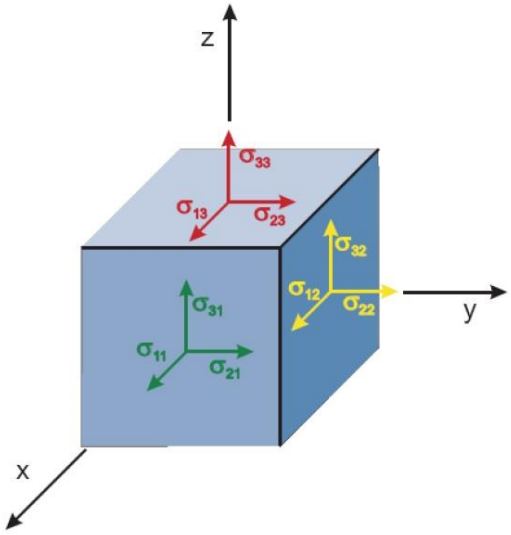

Figure 2.8.: Schematic drawing of the examplary crystal planes in wurtzite structure.

A short excursion to continuum mechanics is required to derive the polarization from stress status quantitatively. The equilibrium state is discussed for the interest of the stress status in crystalline heterojunction structures. This means the studied object has neither linear movement nor rotation. The stress status of an object can be completely described by all stress components shown in Fig. 2.8 with two in-plane stress components and one out-of-plane component for a single plane. So stress σ_{ij} and strain ϵ_{kl} are 2nd order tensors. σ can be written with 3×3 components:

$$\begin{pmatrix} \sigma_{11} & \sigma_{12} & \sigma_{13} \\ \sigma_{12} & \sigma_{22} & \sigma_{23} \\ \sigma_{13} & \sigma_{23} & \sigma_{33} \end{pmatrix}$$

Strain ϵ should also be interpreted in a similar way.

Stress is linked to strain by Hooke's law:

$$\sigma = \mathbf{C} \cdot \epsilon \tag{2.14}$$

where $\mathbf{C}$ is a 4th-order tensor composed of 81 (3^4) components called the elastic constant tensor.

Due to symmetry constraints and the equilibrium state, σ and ϵ have only 6 components each. The symmetric 1st order tensors of σ and ϵ can be simplified to be a 6-dimensional vector in Voigt's notation. Then, $\mathbf{C}$ is written as a 2nd order tensor with 6×6 components and Hooke's law reads:

$$\begin{pmatrix} \sigma_{11} \\ \sigma_{22} \\ \sigma_{33} \\ \sigma_{12} \\ \sigma_{23} \\ \sigma_{31} \end{pmatrix} = \begin{pmatrix} C_{11} & C_{12} & C_{13} & C_{14} & C_{15} & C_{16} \\ C_{12} & C_{22} & C_{23} & C_{24} & C_{25} & C_{26} \\ C_{13} & C_{23} & C_{33} & C_{34} & C_{35} & C_{36} \\ C_{14} & C_{24} & C_{34} & C_{44} & C_{45} & C_{46} \\ C_{15} & C_{25} & C_{35} & C_{45} & C_{55} & C_{56} \\ C_{16} & C_{26} & C_{36} & C_{46} & C_{56} & C_{66} \end{pmatrix} \cdot \begin{pmatrix} \epsilon_{11} \\ \epsilon_{22} \\ \epsilon_{33} \\ \epsilon_{12} \\ \epsilon_{23} \\ \epsilon_{31} \end{pmatrix} \tag{2.15}$$

The crystal symmetry in the wurtzite structure helps to reduce the components in the tensor $\mathbf{C}$ further [Sch11a]:

$$\begin{pmatrix} \sigma_{11} \\ \sigma_{22} \\ \sigma_{33} \\ \sigma_{12} \\ \sigma_{23} \\ \sigma_{31} \end{pmatrix} = \begin{pmatrix} C_{11} & C_{12} & C_{13} & 0 & 0 & 0 \\ C_{12} & C_{11} & C_{13} & 0 & 0 & 0 \\ C_{13} & C_{13} & C_{33} & 0 & 0 & 0 \\ 0 & 0 & 0 & C_{44} & 0 & 0 \\ 0 & 0 & 0 & 0 & C_{44} & 0 \\ 0 & 0 & 0 & 0 & 0 & \frac{1}{2}(C_{11} - C_{12}) \end{pmatrix} \cdot \begin{pmatrix} \epsilon_{11} \\ \epsilon_{22} \\ \epsilon_{33} \\ \epsilon_{12} \\ \epsilon_{23} \\ \epsilon_{31} \end{pmatrix} \tag{2.16}$$

In the case of biaxial strain in the (0001) plane of wurtzite III-nitrides, $\sigma_{33} = 0$, $\sigma_{11} = \sigma_{22}$ and no shear forces exist. We obtain

$$\epsilon_{\perp} = -\frac{2C_{12}}{C_{11}}\epsilon_{\parallel}. \tag{2.17}$$

The piezoelectric polarization $\vec{P}_{\mathrm{pz}}$ can be linked to the stress tensor σ or strain tensor ϵ via the piezoelectric modulus tensor $\mathbf{d}$ or $\mathbf{e}$, respectively, using the following

equations:

$$\vec{P}_{\mathrm{pz}} = \mathbf{d} \cdot \sigma = \mathbf{e} \cdot \epsilon \tag{2.18}$$

Similar to the simplification of the elastic constant tensor $\mathbf{C}$, the piezoelectric moduli of the wurtzite crystal structure can be expressed using Voigt's notation as follows:

$$\mathbf{e} = \begin{pmatrix} 0 & 0 & 0 & 0 & e_{15} & 0 \\ 0 & 0 & 0 & e_{15} & 0 & 0 \\ e_{31} & e_{31} & e_{33} & 0 & 0 & 0 \end{pmatrix} \tag{2.19}$$

$$\mathbf{d} = \begin{pmatrix} 0 & 0 & 0 & 0 & d_{15} & 0 \\ 0 & 0 & 0 & d_{15} & 0 & 0 \\ d_{31} & d_{31} & d_{33} & 0 & 0 & 0 \end{pmatrix} \tag{2.20}$$

According to Hooke's law, $\mathbf{e} = \mathbf{dC}$ is derived with which the tensor $\mathbf{e}$ can be transformed to the tensor $\mathbf{d}$ or vice versa. In the following, only $\mathbf{e}$ is discussed for the purpose of simplicity.

As already seen in Equ. 2.19, the piezoelectric polarization vector is linked to the strain status via three constants e_{31}, e_{33}, e_{15}:

$$\begin{pmatrix} P_{pz,x} \\ P_{pz,y} \\ P_{pz,z} \end{pmatrix} = \begin{pmatrix} 0 & 0 & 0 & 0 & e_{15} & 0 \\ 0 & 0 & 0 & e_{15} & 0 & 0 \\ e_{31} & e_{31} & e_{33} & 0 & 0 & 0 \end{pmatrix} \cdot \begin{pmatrix} \epsilon_{11} \\ \epsilon_{22} \\ \epsilon_{33} \\ \epsilon_{12} \\ \epsilon_{23} \\ \epsilon_{31} \end{pmatrix} = \begin{pmatrix} e_{15}\epsilon_{23} \\ e_{15}\epsilon_{12} \\ e_{31}\epsilon_{11} + e_{31}\epsilon_{22} + e_{33}\epsilon_{33} \end{pmatrix} \tag{2.21}$$

The piezoelectric polarization $P(\theta)$ along a crystal orientation which has a tilting angle of θ with respect to c-axis of wurtzite III-nitrides can be written as

$$P(\theta) = P_{pz,x} \cdot sin(\theta) + P_{pz,z} \cdot cos(\theta). \tag{2.22}$$

The electrostatic field $\vec{F}_{\mathrm{pz}}$ induced by the piezoelectric polarization can be obtained similar as described in Equ. 2.13:

$$\vec{F}_{\mathrm{pz}} = \frac{\vec{P}_{\mathrm{pz}}}{\epsilon\epsilon_0} \tag{2.23}$$

where $\vec{P}_{\mathrm{pz}}$ is the piezoelectric polarization, ϵ the dielectric constant of the material for which the field is calculated and ϵ_0 the vacuum permittivity.

Both, the spontaneous and piezoelectric electrical fields contribute to the total internal field $\vec{F}$ described by the following equation:

$$\vec{F} = \vec{F}_{\mathrm{sp}} + \vec{F}_{\mathrm{pz}} \tag{2.24}$$

2.6.2. Quantum confined Stark effect

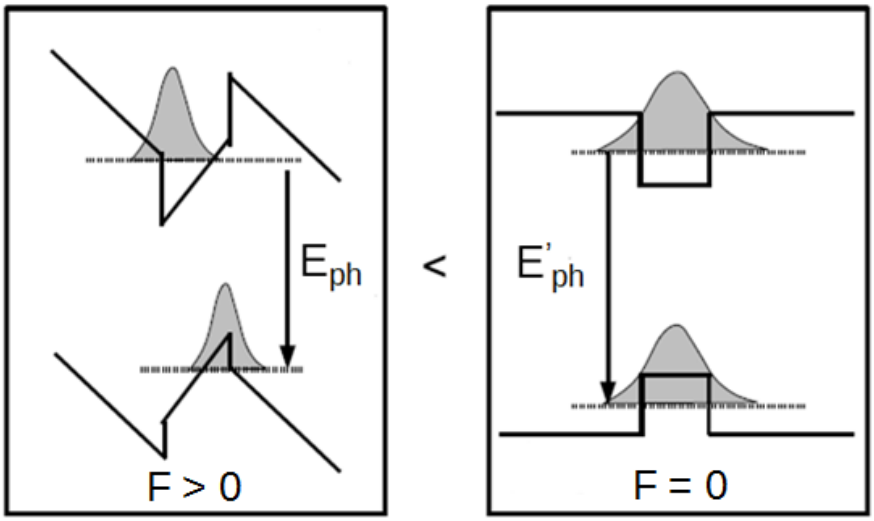

Figure 2.9.: Quantum confined Stark effect: the QW with (left) and without (right) an electrical field. With the electrical field, the band structure is tilted leading to the local separation of electrons and holes and energy reduction of emitted photons.

In InGaN/GaN QWs, the difference of the spontaneous polarization between GaN and InGaN (Table 2.3) invokes an internal electrical field F_{sp} within the QWs. Besides, the piezoelectric polarization contributes to an internal electrical field F_{pz} within the QWs since the InGaN layer is compressively strained. The overall electrical field is the summation of both. Consequently, the band edge within the QWs is tilted confining the electrons and holes at the triangular corners of the conduction band and the valence band, respectively (Fig. 2.9). The wavefunctions of electrons and holes are locally separated resulting in a reduced recombination possibility and hence a lower QW efficiency. Meanwhile, the effective band gap of the QWs gets smaller leading to a red-shift of the emission wavelength. This phenomenon is named as *quantum confined Stark effect*. The lattice mismatch between GaN and $\mathrm{In}_x\mathrm{Ga}_{1-x}\mathrm{N}$ increases with increasing indium content x leading to higher strain and consequently larger piezoelectric field within the QWs. Hence, the problem of the reduced QW efficiency is even more pronounced in the InGaN/GaN QWs for green emission as compared to the blue or violet ones, which is discussed as one main reason for the green gap.

How can we overcome the large internal electrical field within the green InGaN/GaN QWs? Actually the spontaneous polarization is negligibly small as compared to the piezoelectric one for the green InGaN/GaN QWs. Taking the biaxial strain into account, the dependence of the piezoelectric polarization on the crystal orientation can be determined according to Equ. 2.22: it reaches the max. value on the c-plane (polar

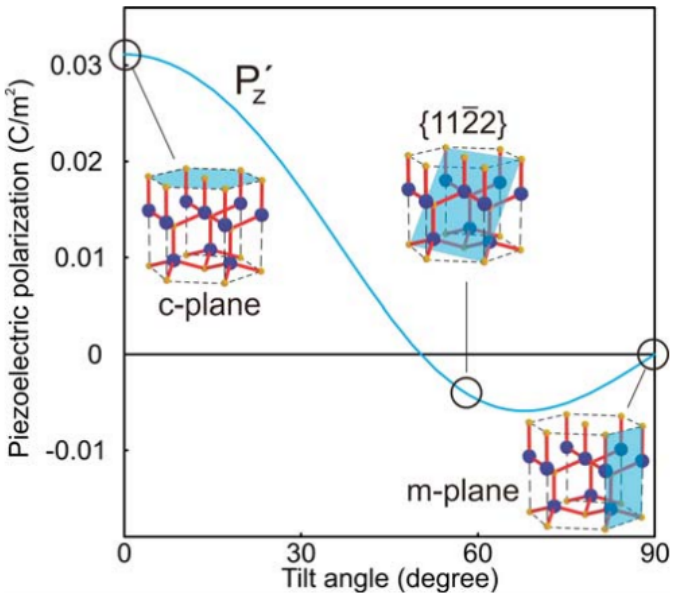

Figure 2.10.: Piezoelectric polarization of an $In_xGa_{1-x}N$ QW grown pseudomorphically between relaxed GaN barriers dependent on the tilt angle. The lattice planes of particular polar, semipolar and nonpolar orientations are shown as insets. P_z' is the polarization perpendicular to the growth plane [Sch07].

plane) and vanishes for the crystal planes with a tilt angle of 90 ° with respect to the *c*-plane (nonpolar planes, e.g., $\{10\bar{1}0\}$ and $\{11\bar{2}0\}$) (Fig. 2.10). All the crystal planes with a tilt angle between 0 ° and 90 ° have a reduced polarization field and are therefore named as semipolar planes, e.g., $\{10\bar{1}1\}$ and $\{11\bar{2}2\}$. Thus, the idea is to employ InGaN/GaN QWs on the nonpolar or semipolar crystal planes as the active region of the green light emitters to avoid the huge internal electrical field within the QWs. Many groups have been making efforts to follow this idea since about a decade. As mentioned shortly in Chapter 1, the investigations go mainly in three directions. One is to fabricate the complete semipolar/nonpolar LED structure on the native GaN substrate with the needed orientation, sliced from a HVPE grown bulk crystal [Fuj08, Zha10a, Zha10b, Kos10, Zha11]. However, the application of a native GaN substrate is limited by its small size and high cost. The second is to grow semipolar/nonpolar (Al)/(In)GaN directly on foreign substrates of respective orientation [Kim13, Jeo13]. Unfortunately, the crystal quality is inferior as compared to the *c*-plane growth. Non-radiative recombination is then compensating the advantage of the reduced internal fields and leads to the bad performance of such devices. The third is to make use of the well-developed technology of the *c*-plane growth in the case of semipolar/nonpolar (Al)/(In)GaN growth on the foreign substrate via two different methods. The first method is to etch parallel trenches into sapphire to achieve *c*-plane-like sidewalls where the n-GaN growth starts and coalesces into a planar surface followed by InGaN/GaN QWs and p-(Al)GaN layers to complete the LED

structure [Sch12, Uch13]. The schematic structure of a planar $\{11\bar{2}2\}$ GaN grown on a patterned $\{10\bar{1}2\}$ sapphire is shown in Fig. 2.11 (upper) as an example. Nevertheless, this method still requires expensive non-*c*-plane sapphire as the substrate. The second method, i.e., the one used in this work, is to realize 3D structures, e.g. stripes or inverse pyramids, via SAE on the *c*-plane GaN template offering a tilted semipolar surface for the deposition of the InGaN/GaN QWs and the subsequent p-(Al)GaN layers [Wun06] (Fig. 2.11, lower).

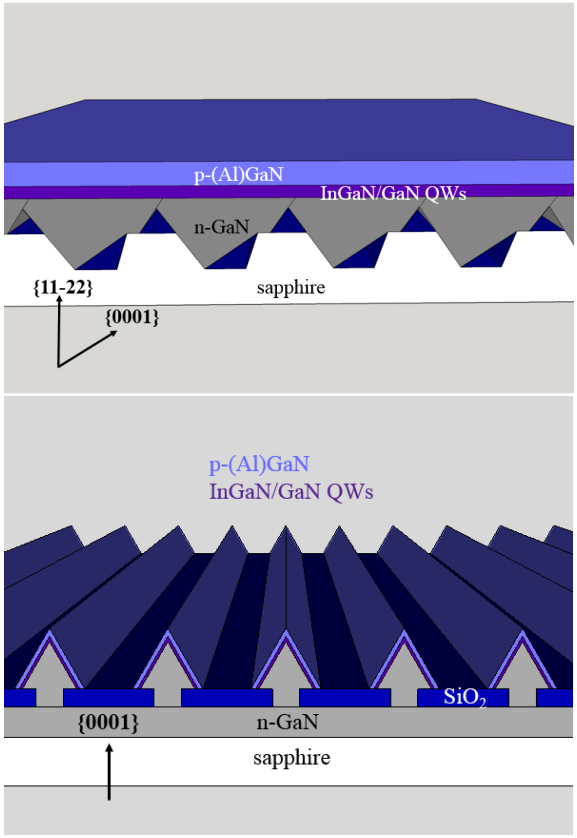

Figure 2.11.: Schematic drawing of semipolar LED structures based on coalesced $\{11\bar{2}2\}$ GaN on patterned $\{10\bar{1}2\}$ sapphire (upper) and on parallel GaN stripes realized via SAE on *c*-plane GaN template with tilted $\{10\bar{1}1\}$ facets as the surface (lower).

2.7. Defects

In most cases, III-nitrides are grown on foreign substrates. Defects are generated due to lattice mismatch between III-nitrides and the respective foreign substrate. The defect density is much higher in the nitrides than in other material systems employed for optoelectronic application, e.g., arsenides and phosphides. The defect deteriorates the

performance of our semipolar LED structure based on the AlInGaN material system via variable mechanisms, e.g., acting as a nonradiative recombination center or a channel for the leakage current when it penetrates the pn-junction.

2.7.1. Point defects

The point defect is zero-dimensional crystalline imperfection including vacancies (missing atoms), interstitials (an extra atom in between the original crystal lattice), substitutionals (a foreign atom sitting on a host atom site) and antisites (in a compound semiconductor, a cation sitting on a nominal anion site, or vice-versa). All the samples in this work are grown with the method of MOVPE (metalorganic vapor phase epitaxy) which will be discussed in details in Section 3.1. C, H and O are intrinsic impurities, namely point defects, incorporated in MOVPE-grown GaN: the sources of C and H are the precusors of NH_3 and the metalorganic Ga such as $Ga(CH_3)_3$ or $Ga(C2H_5)_3$ and O often comes from the impurity in the precusor NH_3.

2.7.2. Dislocations

A dislocation is a one-dimensional defect. Due to the lack of bulk substrates, GaN is grown on foreign substrates, e.g., sapphire in this work. The very first epilayer, i.e., the nucleation layer, is composed of densely packed, uniform islands. Crystal islands collide and coalesce with each other in the subsequent GaN growth. Threading dislocations (TDs) may be generated and this could be caused by the collision of the crystal islands which are tilted or twisted according to each other [Mor09]. The TD density may be as high as 10^8–$10^{10}\,\mathrm{cm}^{-2}$ for *c*-plane GaN on sapphire grown by MOCVD [Her08]. Several growth techniques help to reduce the dislocation density, e.g., the insertion of an in-situ SiN epi-mask and epitaxial lateral overgrowth. In the case of our 3D semipolar samples, the dislocation density is bent by the in-situ SiN interlayer in the *c*-plane GaN template and blocked by the ex-situ SiO_2 epi-mask as well. Another issue concerning TDs in InGaN/GaN-based LEDs stays in the active region of InGaN/GaN QWs. Misfit dislocations may be caused by the lattice mismatch between InGaN and GaN and lie in the interface plane at the heterojunction. As mentioned before, strain in the InGaN/GaN active region is typically released via formation of misfit dislocations in the case of *c*-plane structure and via the formation of basal-plane stacking faults (BSFs) which will be discussed in the next section in the case of nonpolar structure. For our semipolar samples, both of these two strain relaxation mechanisms exist.

2.7.3. Planar defects

As its name indicates, the planar defect is a two-dimensional crystal imperfection. The stacking fault is a disorder in the stacking sequence of the atomic layers. The wurtzite structure has a stacking sequence of the atomic layers as ABABAB along the c-direction. A change into the sequence of ABABCBC (I_1-type), ABABCACA (I_2-type), ABABCABAB (E-type) etc. leads to the formation of a stacking fault. The stacking faults lying in the c-plane of the wurtzite structure are named as BSFs while the ones lying in other crystal planes are indicated either as pyramidal or prismatic stacking faults depending on the defect orientations both abbreviated as PSFs in the literature. The BSFs in the wurtzite GaN structure have a low formation energy [Sta98]. Therefore, it is the type of stacking faults which occurs most often. The BSFs initiated in the GaN buffer layer run in parallel to the QWs as well as the pn-junction in the c-plane LED and therefore are not very harmful for LED performance. However, BSFs intercept the active region and the pn-junction in semipolar and nonpolar LEDs deteriorating the LED performance.

3. Sample Preparation

The 3D semipolar LEDs in this work are realized by depositing InGaN/GaN QWs and p-(Al)GaN layers on tilted semipolar facets of a 3D n-GaN structure which was achieved via SAE. In this chapter, the sample preparation procedure is explained with the emphasis on the epitaxial methods, the substrate materials and the SAE technique.

3.1. Epitaxy method - MOVPE (metalorganic vapor phase epitaxy)

Metalorganic vapor phase epitaxy (MOVPE) is today the commercially most important epitaxial growth method for III-V semiconductors. All samples throughout this work were grown in an Aixtron-200/4RF-S horizontal MOVPE reactor.

Precursors

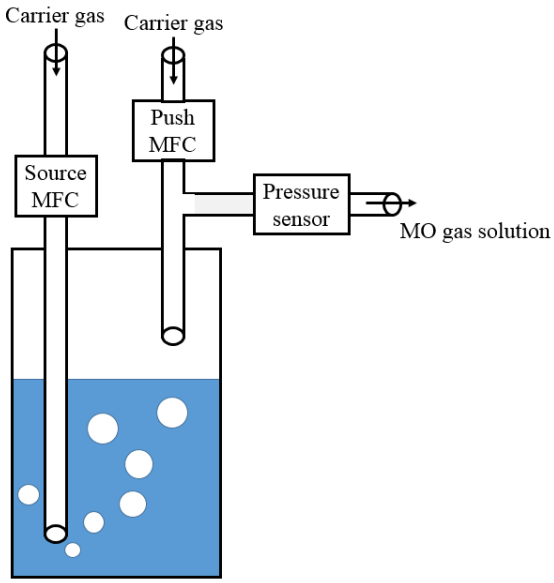

Figure 3.1.: The schematic drawing of the bubbler configuration.

As the name tells, MOVPE is an epitaxy method employing precursors in vapor phase. For the crystal growth of group III-nitrides, the hydrides ammonia (NH_3) and silane (SiH_4) are supplied in gas phase at RT and act as the precursor of the element nitrogen and the Si-dopant, respectively, while metalorganics (MO) are used as the precursors of the group III elements and the Mg-dopant. The molar flow rate of gases, e.g., NH_3 and SiH_4, is controlled by electronic mass flow controllers (MFC). The standard MO precursors are listed below:

- trimethylgallium (TMGa): $(CH_3)_3Ga$
- triethylgallium (TEGa): $(C_2H_5)_3Ga$
- trimethylindium (TMIn): $(CH_3)_3In$
- trimethylaluminium (TMAl): $(CH_3)_3Al$
- bis(cyclopentadienyl)magnesium (Cp_2Mg): $(C_5H_5)_2Mg$

The MO materials are either liquid or solid with a fairly high vapor pressure. They are stored in a container called *bubbler* lying in a water bath with a constant adjustable temperature. The carrier gas H_2 or N_2 flows through the bubbler, dissolves the MO precursor to form a saturated gas solution and flows out of the bubbler as shown in Fig. 3.1. An additional amount of the carrier gas dilutes the saturated gas solution directly after the bubbler to avoid any condensation of the MO precursors on the gas pipe. The molar flow rates of the carrier gas flowing into the bubbler and the carrier gas for dilution are controlled by MFCs as well, named as 'source' and 'push', respectively, in the Aixtron system. The carrier gas can be switched from the bubbler to a by-pass pipe by a 4/2-way valve in order to keep the carrier gas flowing in a stand-by mode. To calculate the molar flow of transported MO materials n, the following equation is required:

$$n[\frac{\text{mole}}{\text{min}}] = f[\text{sccm}] \cdot 10^{-6} \cdot \frac{p(T) \cdot p_0}{(p_\text{B} - p(T)) \cdot R \cdot T_0} \tag{3.1}$$

where f is the molar flow rate of the carrier gas with the unit sccm (standard cubic centimeter per minute), $p(T)$ the vapor pressure of the MO precursors dependent on the bubbler temperature T, p_B the bubbler pressure, R the gas constant, p_0 the standard pressure (10^5 Pa) and T_0 the standard temperature (15 °C). Obviously, it is the easiest way to vary the flow rate of the carrier gas and also possible to change the bubbler pressure to obtain different molar flow rates of transported MO precursors.

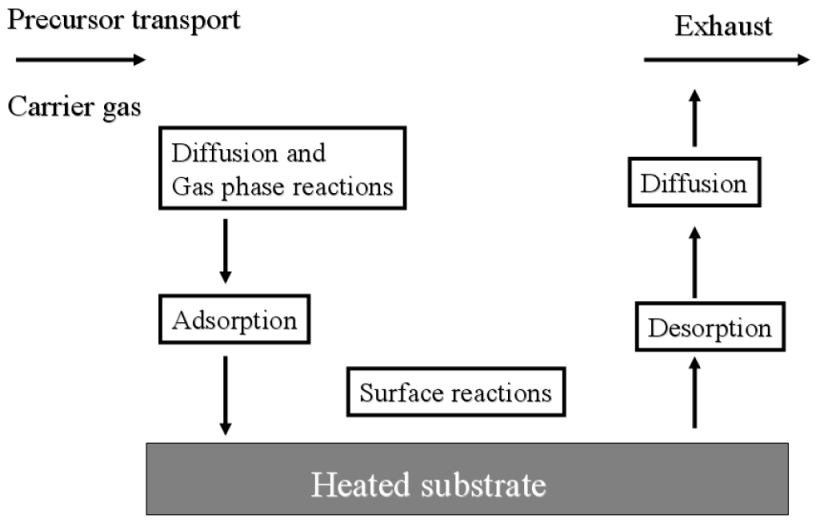

Figure 3.2.: Schematic description of the basic process steps involved in MOVPE growth [Tha10].

Growth kinetics

Taking the MOVPE growth of GaN with the precursors NH_3 and TMGa as an example, the overall chemical reaction can be expressed as

$$Ga(CH_3)_3 + NH_3 \rightarrow GaN + 3CH_4.$$

GaN growth requires a temperature as high as about 1000 °C to crack the precursors. Still NH_3 cracks only partly due to its high thermal stability. Hence, NH_3 is supplied in excess. The basic process steps involved in MOVPE growth can be schematically described by Fig. 3.2. Our MOVPE reactor consists of a quartz liner in a steel tube. The substrate sits on a rotating susceptor heated by an inductive radio frequency coil, i.e., only the susceptor is directly heated. Therefore, the chemical reaction occurs only close to the susceptor with a sufficiently high temperature. In a horizontal MOVPE reactor, the processing gases flow horizontally over the substrate, react chemically there and flow into the exhaust. The process pump is connected to the exhaust controlling the reactor pressure.

The MOVPE growth is affected by the temperature differently in three different temperature ranges (Fig. 3.3).

- At low temperatures, the thermal cracking of the MO precursors limits the growth rate k which depends on the temperature T according to the Arrhenius law: $k = e^{-\frac{E_A}{k_B T}}$ with E_A representing the activation energy and k_B Boltzmann's constant. Meanwhile, the adatoms on the substrate surface do not have a sufficiently high mobility to move to the suitable site for layer by layer growth leading to high defect density.

- At medium temperatures, the MO precursors are 100 % thermally cracked. The growth rate is then linearly related to the supply of the MO precursors independent on the temperature. Moreover, the mobility of the adatoms on the substrate surface is high enough to achieve reasonable crystal quality in this temperature regime. MOVPE is normally operated in this temperature regime (*mass transport limited regime*), i.e., 800–1200 °C for GaN.

- At high temperatures, more adatoms desorb from the substrate surface and the crystal dissolves leading to high defect density. In this case, the growth rate decreases with increasing temperature.

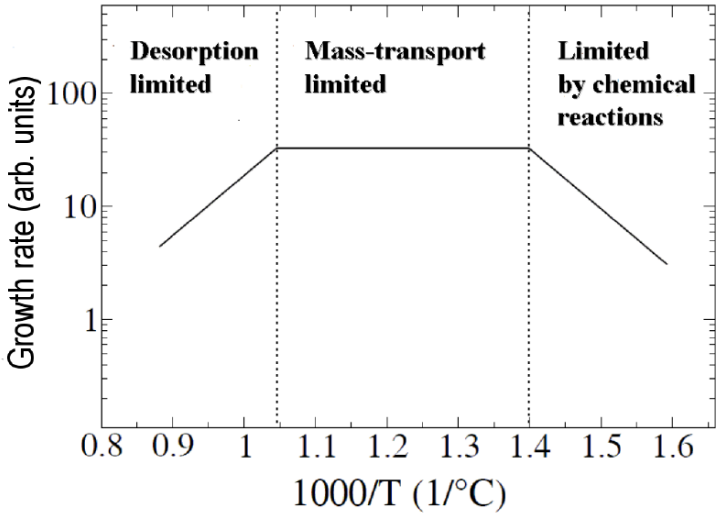

Figure 3.3.: Schematic illustration of temperature dependence on growth rate in MOVPE [Str99].

3.2. Sapphire

The substrate material should have small lattice mismatch, small thermal expansion mismatch, the same atomic arrangement as the epi-layer and stability for the epitaxial and processing steps. In this point of view, GaN would be the best substrate for itself. However, GaN cannot be grown from its stoichiometric melt by the Czochralski or Bridgman methods commonly used for typical semiconductors due to extremely high melting temperature and corresponding equilibrium pressure at melting [Grz01]. Therefore, its usage is very limited due to the small size and the high cost of GaN single bulk crystals [Sch07]. Sapphire (Al_2O_3) is the most commonly used substrate for the AlGaInN system and employed for all structures discussed in this thesis. It has the hexagonal crystal structure as wurtzite III-nitrides do. It is chemically stable under GaN epitaxial conditions, available with high crystal quality and relatively cheap compared to other substrates. The lattice mismatch and the thermal expansion mismatch

Table 3.1.: Lattice mismatch [Vur03, Mis03] and thermal mismatch [Nak00] between c-plane GaN epi-layer and c-sapphire substrate. Two values for lattice mismatch are obtained when the crystal direction $[01\bar{1}0]$ of GaN is oriented along the crystal direction $[1\bar{1}00]$ and $[1\bar{2}10]$ of sapphire, respectively. α_a and α_c are thermal expansion coefficients along a-axis and c-axis, respectively.

	Periodic distance (nm)		α_a ($10^{-6}\,\mathrm{K}^{-1}$)	α_c ($10^{-6}\,\mathrm{K}^{-1}$)
GaN	0.3189 ∥ $[01\bar{1}0]$	0.3189 ∥ $[01\bar{1}0]$	5.59	3.17
sapphire	0.4785 ∥ $[1\bar{1}00]$	0.2763 ∥ $[1\bar{2}10]$	7.5	8.5
lattice mismatch	30 %	16 %		

(Table 3.1) between sapphire and GaN are fairly high. The lattice mismatch is as high as 30 % when their crystal directions are oriented in the same way with the basal plane (0001) as the interface Table 3.1. The $[1\bar{1}00]$ crystal direction of GaN would overlap the $[1\bar{2}\bar{1}0]$ direction of sapphire when rotating the GaN layer by 30 ° around the axis [0001]. This leads to a much reduced lattice mismatch of 16 % and is actually the GaN/sapphire orientation relation in epitaxial growth. Reasonable crystal quality of GaN with a dislocation density $< 2 \times 10^8$ cm^{-2} can be obtained on sapphire with deposition of low-temperature wetting layer, i.e., AlN or GaN and SiN interlayer for defect reduction [Her08] despite of their high lattice mismatch and thermal expansion mismatch.

3.3. Selective area epitaxy

SAE is the local growth of semiconductors through partial masking of the semiconductor template by dielectric materials, typically employed in MOVPE. Firstly, a layer of the epi-mask material is deposited on the semiconductor template and removed within a certain area via lithography and etching where the underlying semiconductor is exposed (the opening). Then, the semiconductor overgrowth occurs selectively in the opening rather than on top of the dielectric epi-mask due to the high surface energy between the GaN crystal and the amorphous masking material. The precursors in the epi-mask area are transported to the opening via gas phase diffusion and surface migration [Wun11].

On one hand, the mask material should be stable under the GaN growth condition with the temperature above 1000 °C and in the atmosphere of the corrosive gas H_2. On the other hand, the surface energy between the mask material and the grown crystal should be sufficiently high to provide good selectivity, i.e., the precursors in the epi-mask area can be transported to the opening before they get deposited on the

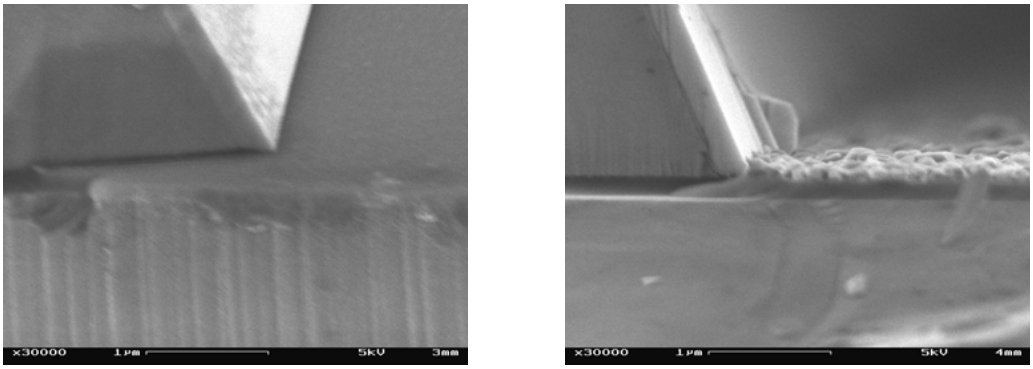

Figure 3.4.: SEM images at the bottom of the stripe LEDs emitting at 430 nm (left) and 500 nm (right). Polycrystalline material is observed on the epi-mask in the latter LED emitting at 500 nm with a higher indium content in the active QWs but not in the former LED.

epi-mask surface in the form of polycrystalline material. SiO_2 and Si_3N_4 are suitable epi-masks for GaN. However, the selectivity gets worse for InGaN than GaN. This is due to the low growth temperature of InGaN as compared to that of GaN which reduces mobility of the precusors. InGaN with increasing indium content requires an even lower growth temperature leading to decreasing selectivity. This can be confirmed experimentally by observing a clean epi-mask surface in the stripe LEDs emitting at 430 nm while polycrystalline material can be found on the dielectric mask in the stripe LEDs emitting at 500 nm with a higher indium content (Fig. 3.4). A SiO_2 epi-mask has been employed for all samples in this work. An important parameter of the epi-mask, filling factor, is defined as the area ratio of the opening over the whole surface:

$$\mathrm{FF} = \frac{A_{\mathrm{open}}}{A_{\mathrm{open}} + A_{\mathrm{mask}}} = \frac{A_{\mathrm{open}}}{A_{\mathrm{period}}}. \tag{3.2}$$

This parameter affects the evolution of the 3D GaN structure and varies surface facet of GaN inverse pyramids to be $\{10\bar{1}1\}$, $\{11\bar{2}2\}$ or a mixture of both. The respective experimental results will be discussed in section 5.1

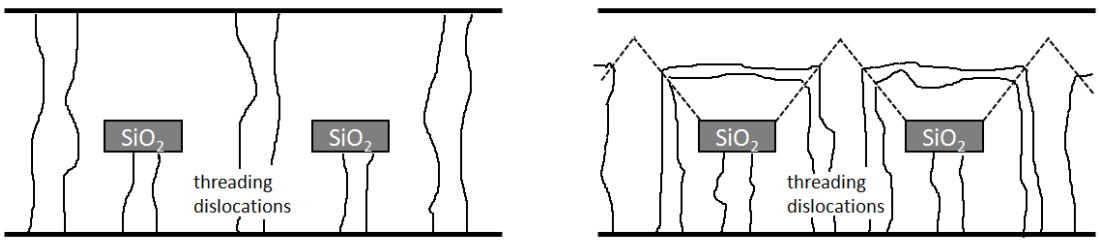

Figure 3.5.: Schematic illustration of the techniques ELO (left) and FACELO (right).

SAE is employed for defect reduction in the technique of epitaxial lateral overgrowth

(ELO) [Sch12]. The epitaxial overgrowth initiates in the opening and develops laterally to form a planar layer embedding the epi-mask. The TDs in the semiconductor template are blocked in the epi-mask region leading to a reduced dislocation density in the overgrown material (Fig. 3.5, left). The dislocation density is even reduced further in the advanced version facet-assisted epitaxial lateral overgrowth (FACELO) [Sch12]. The corresponding epitaxial overgrowth involves two phases: the 3D GaN structure with tilted facets is realized by applying proper growth conditions to push the vertical growth in the 1st phase. The growth condition in the 2nd phase is chosen in favor of the lateral growth so that the threading dislocations are bent horizontally leaving the top part of the GaN crystal essentially free of TDs (Fig. 3.5, right).

The technique SAE is employed for the production of native GaN substrates in hydride vapor phase epitaxy (HVPE) as well. Despite of an increasing application of GaN as a material for devices, usage of the native GaN substrate is limited due to its small size and high cost. Thick layers grown on sapphire are a good candidate to provide GaN wafers for industrial processes [Nak13, Mey13]. However, a big difference of thermal expansion coefficients and lattice mismatch between GaN and sapphire result in wafer bowing or even cracks after cooldown. The technique SAE forms an easy-breaking interlayer and the thick GaN layer is removed from sapphire at this defined position to produce freestanding GaN substrates [Lip10].

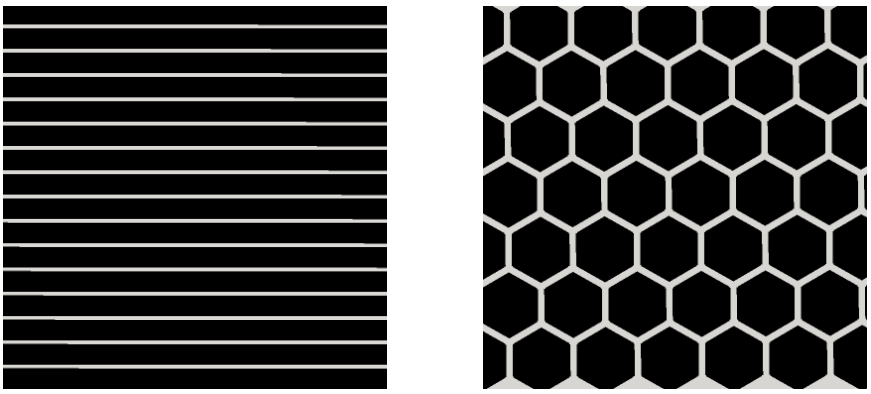

Figure 3.6.: Schematic drawing of the epi-mask patterns for SAE – parallel stripes (left) and periodically arranged hexagons (right). The black region is the epi-mask and the grey area is the opening.

3.4. Preparation procedure

InGaN/GaN QWs are employed as luminescence core of green LEDs. However, the efficiency of the InGaN/GaN QWs decreases drastically with increasing emission wavelength. The polar character of the nitride semiconductors is discussed as one main reason (refer to section 2.6.2). In this thesis, we prepare semipolar LEDs grown on the side-facets of 3D structures fabricated by SAE on *c*-plane sapphire [Wun08b, Wan13].

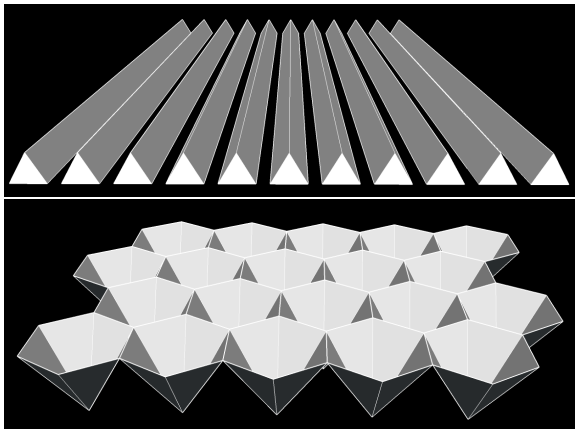

Figure 3.7.: Schematic drawing of the 3D GaN structures – parallel stripes (upper) and inverse pyramids (lower).

Due to lack of native substrates, sapphire is employed for GaN growth. About 3 µm thick *c*-plane GaN on *c*-plane sapphire is taken as a template. Firstly, a 200 nm thick SiO_2 layer is deposited on the GaN template by plasma enhanced chemical vapor deposition (PECVD) and patterned via photolithography and dry etching with a CF_4 plasma to act as the epi-mask in the next step. Then, 3D structures are achived via SAE under a growth condition which favors vertical growth. Low temperature, low V/III ratio and high pressure were found to be in favor of the vertical growth [Wun09]. The epi-mask is patterned in either periodic parallel stripes or hexagons with periods of some µm (Fig. 3.6). The pattern of parallel stripes leads to the formation of 3D GaN stripes (Fig. 3.7, upper). The parallel stripes patterned in the SiO_2 epi-mask are aligned along either the crystal direction $\langle 10\bar{1}0\rangle$ or $\langle 11\bar{2}0\rangle$. Accordingly, the facet $\{11\bar{2}2\}$ or $\{10\bar{1}1\}$ is naturally stabilized as the tilted surface of the 3D GaN structure [Neu05]. The other epi-mask pattern type consists of periodically arranged hexagonal masked areas separated by openings in between. The GaN growth starts in the openings and approaches the hexagon centers forming 3D inverse pyramids with either $\{11\bar{2}2\}$ or $\{10\bar{1}1\}$ facets or even both as tilted semipolar surface (Fig. 3.7, lower). Actually, the $\{11\bar{2}2\}$ and $\{10\bar{1}1\}$ facets compete with each other and the one with the higher growth rate turns out to be the surface. The parameters temperature, V/III ratio, pressure and FF affect the growth rate of different facets in a different way. By varying these four parameters, one can stabilize the desired facet as the surface of the inverse pyramids. The experimental result to stabilize the $\{10\bar{1}1\}$ facet as the surface of the GaN inverse pyramids will be discussed in section 5.1. Finally, semipolar InGaN/GaN QWs are deposited on the tilted side facets of the 3D GaN structure. With subsequent p-(Al)GaN layers, the semipolar LEDs are completed.

Following growth, the wafers were annealed in an air atmosphere at 750 °C for 1 min in order to depassivate the Mg acceptors. Then, indium contacts were evaporated onto the wafer by electron evaporation. After this step, the LED sample is ready for the EL test.

4. Semipolar LEDs on $\{10\bar{1}1\}$ Side Facets of GaN Stripes

Both, optical and electrical performance are necessary to obtain high-efficient LEDs. In this chapter, we will discuss how the electrical properties of semipolar LEDs on $\{10\bar{1}1\}$ side facets of GaN stripes are affected by our various individual functional layers: SiO_2 epi-mask, spacer (the intentionally undoped layer lying directly on top of the active region), main p-GaN layer and p-contact layer. The schematic structure of the stripe $\{10\bar{1}1\}$ LED is shown in Fig. 2.11 (lower).

4.1. Insulation of SiO_2 epi-mask

In the beginning phase of this work, the leakage current of the semipolar LEDs on $\{10\bar{1}1\}$ facets is as high as ∼5 mA at -10 V. As mentioned, a parallel GaN stripe structure was achieved via SAE employing PECVD-deposited SiO_2 as epi-mask. The SiO_2 epi-mask has to be insulating to block any leakage current flowing through it directly into n-GaN. Therefore, we checked the electrical insulation of the SiO_2 epi-mask experimentally. A sample was taken with the schematic structure shown in Fig. 4.1: A *c*-plane wafer of ∼3 µm n-GaN on the sapphire substrate partly covered with the SiO_2 epi-mask, partly not, with evaporated indium contacts distributed over the sample surface.

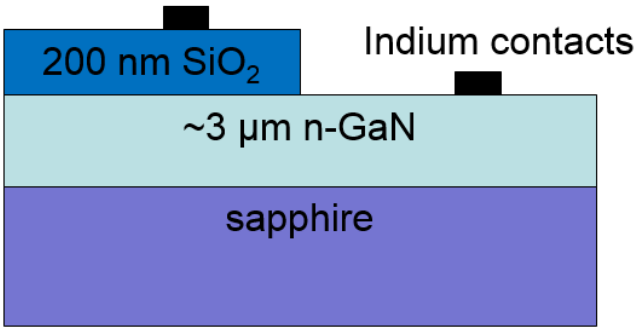

Figure 4.1.: Schematic structure of the sample taken to test the electrical property of the SiO_2 epi-mask.

A I-V curve was measured by applying an external voltage between two contacts on the exposed n-GaN surface, not covered with SiO_2. A linear relation was obtained indicating a resistor-like behavior as expected confirming device functionality. During the PECVD process, the material SiO_2 gets deposited on the sample surface as well as on the free area inside the chamber. The parasitic deposition of the SiO_2 material in the PECVD chamber from the previous runs could get redeposited on the sample surface varying the material property of the SiO_2 epi-mask. The PECVD chamber is refreshed regularly by etching the parasitic deposition away. We prepared two samples, one with SiO_2 deposited in a "clean" PECVD chamber and the other in a "dirty" PECVD chamber. Then, an external voltage was applied between two contacts, one on the n-GaN surface covered with SiO_2 and the other on the exposed n-GaN surface. For both samples, the SiO_2 epi-mask is almost insulating with the current just measured to be below 5×10^{-10} mA and 2×10^{-10} mA, respectively, under the bias ranging from -5 V to 20 V which is larger than the bias range for the test of the stripe $\{10\bar{1}1\}$ LEDs in this work. The I-V curves measured at most of the contacts have a similar shape.

In conclusion, the insulation of the SiO_2 epi-mask is sufficient to block any significant leakage current flowing through it directly into n-GaN.

4.2. Spacer

It was reported that the Mg profile in the intentionally undoped GaN layer separating the p-(Al)GaN layers from the InGaN/GaN active region has a significant effect on the EL output power of LEDs [Köh05]. This intentionally undoped layer directly above the active region is named as spacer. The Mg atoms in the p-(Al)GaN layers diffuse backward approaching the active region at the high temperature during the crystal growth leading to a diffusive interface of the Mg profile. Therefore, the spacer layer is partly or even completely p-doped. Its function is to prevent the Mg atoms from diffusing into the InGaN/GaN QWs since the Mg dopants cause nonradiative recombination centers leading to a reduced QW efficiency. However, a too thick spacer layer results in an insufficient hole injection into the active region, detrimental to the LED performance again. Secondary ion mass spectrometry (SIMS) can not be easily applied on the 3D structure to detect Mg profile in the spacer which is possible for planar structure. We investigated the dependency of the EL output power on the spacer thickness to find an optimum.

The spacer thickness was varied between 22 nm and 67 nm for five stripe $\{10\bar{1}1\}$ LEDs, respectively. The EL output power for a structure with an emission wavelength of 460 nm at a current of 20 mA firstly increases with increasing spacer thickness by avoiding the Mg diffusion into the InGaN/GaN QWs, reaches a maximum value of 19 µW at a spacer thickness of 35 nm and finally decreases with the further increasing spacer thickness presumably due to the reduced hole injection efficiency into the active

region (Fig. 4.2).

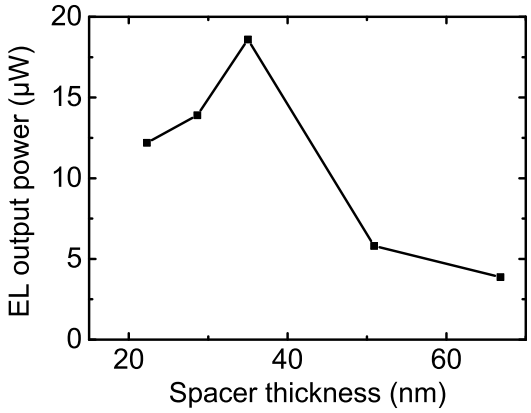

Figure 4.2.: The EL output power at the current of 20 mA of five stripe $\{10\bar{1}1\}$ LEDs with the spacer thickness of 22 nm, 29 nm, 35 nm, 51 nm and 67 nm, respectively.

The local Mg profile at the apex of the stripes is different from that over the facet due to the special morphology of the apex. A plateau will appear at the apex with a growth condition in favor of the lateral growth whereas a sharp tip forms when the vertical growth is enhanced. We modified the morphology of the spacer at the apex to vary the local effective Mg profile. With a plateau, the Mg dopants diffuse closer to the QWs at the apex than over the facet, or even into the QWs while it is not the case with a sharp tip. Firstly, the growth temperature was reduced from 1080 °C to 950 °C to enhance the vertical growth [Wun10]. The growth temperature of 950 °C is close to the lower limitation for a reasonable material quality of the MOVPE-grown GaN. Then, the V/III ratio is reduced from 1100 to 400 to push the vertical growth further [Wun10] while the growth rate keeps constant with the same TMGa molar flow. The EL output power increases dramatically when the spacer growth is pushed vertically (Fig. 4.3). The low EL output power of the LED with the plateau at the apex formed within the spacer (presented by the black curve in Fig. 4.3) is presumably due to a local current crowding at the apex since hole injection is easier when the Mg dopants diffuse closer to the QWs.

As a summary, a spacer thickness of 35 nm is found to be best to achieve the optimal EL output power for the stripe $\{10\bar{1}1\}$ LEDs. Enhancement of vertical growth in the spacer increases the EL output power, presumably due to a better Mg profile at the apex.

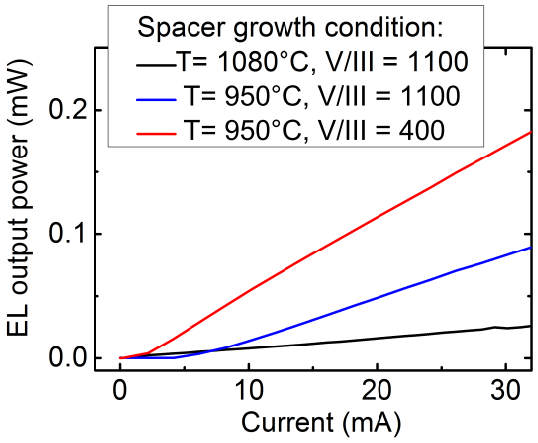

Figure 4.3.: The EL output power for the stripe $\{10\bar{1}1\}$ LEDs with the spacer grown under different conditions. Lower temperature and less V/III ratio are in favor of the vertical growth.

4.3. p-doping in the main p-GaN layer

Good conductivity of both, n-type and p-type GaN is essential to obtain effcient GaN-based LEDs. The doping problem proves to be more challenging in case of p-type for GaN. The GaN-based LED was made possible in 1989 by solving the p-doping problem using Mg doping followed by post-growth low energy electron irradiation [Ama89] or thermal annealing [Nak92]. This is due to the fact that the dopant is passivated by hydrogen (the carrier gas in MOVPE) by forming a bond between the acceptor and the single electron in the outer shell of the hydrogen atom. However, the p-conductivity in GaN is still inferior as compared to the n-conductivity. The electrical conductivity σ is dependent on the density n and the mobility μ of the free charge carriers:

$$\sigma = qn\mu \tag{4.1}$$

with q representing the elementary charge. The low hole concentration in p-GaN is on one hand due to the fact that the activation energy is as high as 180–200 meV for the acceptor Mg whereas it is 12–17 meV for the donor Si [Göt96] and on the other hand, limited by the self-compensation effect [Kau00]. (The hole concentration saturates and drops when the acceptor concentration reaches a certain value by forming a Mg-related complex as shown in Fig. 4.4.) The highest hole concentration has been reported to be $2 \times 10^{19}\,\mathrm{cm}^{-3}$ in p-GaN grown by metal modulated epitaxy (metal modulated epitaxy is a technique wherein only the metal fluxes (Al, Ga, In, and Mg) are modulated in a short periodic fashion in radio-frequency molecular beam epitaxy system, while maintaining a continuous nitrogen plasma flux. [Try09]). This exceptionally high hole concentration is questionable since it is obtained only by one group whereas more or less all other groups achieve hole concentrations not higher than $1 \times 10^{18}\,\mathrm{cm}^{-3}$. The lower mobility of the holes as compared to that of the electrons counts as another

factor leading to the lower p-conductivity. Moreover, the GaN layer deposited in the MOVPE is intrinsically n-doped by the background oxygen or vacancies compensating the p-conductivity. Oxygen originates from external leakages if they exist and the impurities (in the form of O_2, CO, CO_2, H_2O and so on) in the source materials, e.g., the metalorganics, NH_3 and the carrier gases. our *c*-plane GaN layer has an intrinsic electron density below $10^{16}\,\mathrm{cm}^{-3}$ [Mei16].

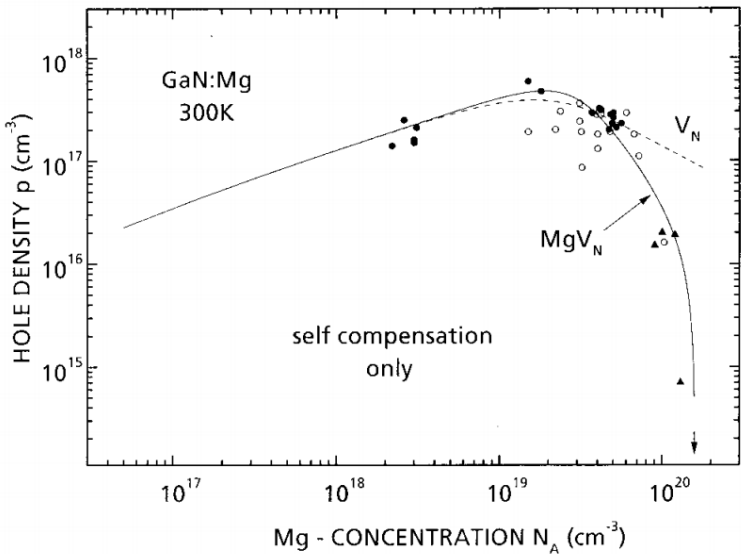

Figure 4.4.: Hole density dependent on Mg concentration in GaN:Mg [Kau00]. Solid circles, open circles and triangles correspond to data from different time and different groups. The dashed and the full curve are fits based on two self-compensation models, assuming the isolated nitrogen vacancy V_N or the nearest neighbor complex MgV_N as the compensating donor, respectively.

Lots of investigations were done for the optimal hole conductivity of planar p-GaN. However, little is known about the 3D semipolar p-GaN since Hall measurement is not applicable and SIMS is difficult on 3D structures. We have tried to investigate the determination of the Mg concentration of 3D semipolar p-GaN – $\{10\bar{1}1\}$ and $\{11\bar{2}2\}$ – via SIMS analysis.

In order to compare the Mg incorporation efficiency, a *c*-plane LED, a stripe $\{10\bar{1}1\}$ LED and a stripe $\{11\bar{2}2\}$ LED were grown on three quarters of a wafer simultaneously in the same epitaxial run. As mentioned, the 3D LED is realized via SAE on a c-plane GaN template covered by a SiO_2 epi-mask. The SiO_2 layer is removed completely within one quarter of the wafer, whereas it is patterned into periodic stripes with 10 µm wide masked area and 3 µm wide opening along the crystal directions $\langle 11\bar{2}0\rangle$ and $\langle 10\bar{1}0\rangle$, respectively, within the other two quarters of the wafer and patterned into periodic hexagons within the fourth quarter of the wafer. The structure formed with the epi-mask of the hexagonal pattern is not discussed here. Epitaxial overgrowth

was applied on the processed template to form 3D stripe LEDs on the two quarters of the wafer with the stripe pattern and planar c-plane LED structure on the quarter of the wafer without any SiO_2 epi-mask. As a tool of material composition analysis, conventional SIMS measurements normally collect the signal over a surface of about $100\,\mu m^2$ or even larger area, not able to spatially resolve the GaN-based stripes and the SiO_2 epi-mask in between. In contrary, imaging SIMS employs a finely focused primary ion beam to achieve an analytical spot diameter of about 150 nm (Y. Gao, private communication). The SIMS images can be recorded as a function of depth and lateral position as another ion gun sputters the sample layer by layer. The SIMS measurements were performed with a time-of-flight SIMS instrument manufactured by the company ION-TOF in which Bi^+ and O^{2+} were used as the primary ion and sputtering ion, respectively. Hence, the method of image SIMS is applied to the stripe LEDs with $\{10\bar{1}1\}$ and $\{11\bar{2}2\}$ facets, respectively, to characterize their Mg and In concentrations. The sputtering ion beam was oriented in parallel with the GaN-based stripes and with an angle of 45 ° to the sample surface for the two types of stripe LEDs.

The chemical Si, Mg and In concentrations of the sample with a molar flow ratio between Cp_2Mg and TMGa (Cp_2Mg/TMGa) of 0.06 % during the main p-GaN layer growth were determined by SIMS. The Si, Mg and In signals integrated over a sputtering depth of 1–2 µm are shown in Fig. 4.5 for the stripe LED with the $\{11\bar{2}2\}$ facet indicating the expected stripe period of 13 µm. Obviously the area with a high Si concentration is the SiO_2 epi-mask between the GaN-based stripes. Detected Mg and In concentrations from the same surface area are higher than the value because the presence of SiO_2 enhances the ion yield. At the stripe tip, a low In concentration is detected opposite to the reported increasing In concentration from the bottom to the tip of the stripes [Wun11]. This is presumably due to the different sputtering behaviour there.

The Mg concentration was determined for the stripe LEDs from a rectangular integration area with the size of $1.5 \times 40\,\mu m^2$. The integration window was positioned with the long side parallel to the stripes and in the middle of the stripe facet to avoid measurement artifacts caused by the SiO_2 epi-mask and the stripe tip. The Mg concentrations in the main p-GaN layer of the stripe LEDs with the $\{10\bar{1}1\}$ and $\{11\bar{2}2\}$ facets and the c-plane LED are $4 \times 10^{19}\,cm^{-3}$, $1.5 \times 10^{19}\,cm^{-3}$ and $1.5 \times 10^{19}\,cm^{-3}$, respectively, for the wafer with Cp_2Mg/TMGa = 0.06 % (Fig. 4.6). Hence, the Mg incorporation efficiency on the GaN crystal plane $\{10\bar{1}1\}$ is higher than that on $\{11\bar{2}2\}$, confirming similar findings on planar semipolar layers [Cru09, Sch14]. The Mg incorporation efficiency is not directly comparable between the planar c-plane and the 3D semipolar structures due to the different surface morphologies.

The five-fold InGaN/GaN QWs on the semipolar facets are resolved by imaging SIMS as indicated by the indium signal from the cross sections of the stripes (Fig. 4.7). The InGaN/GaN superlattice stucture is continuous in the cross section along

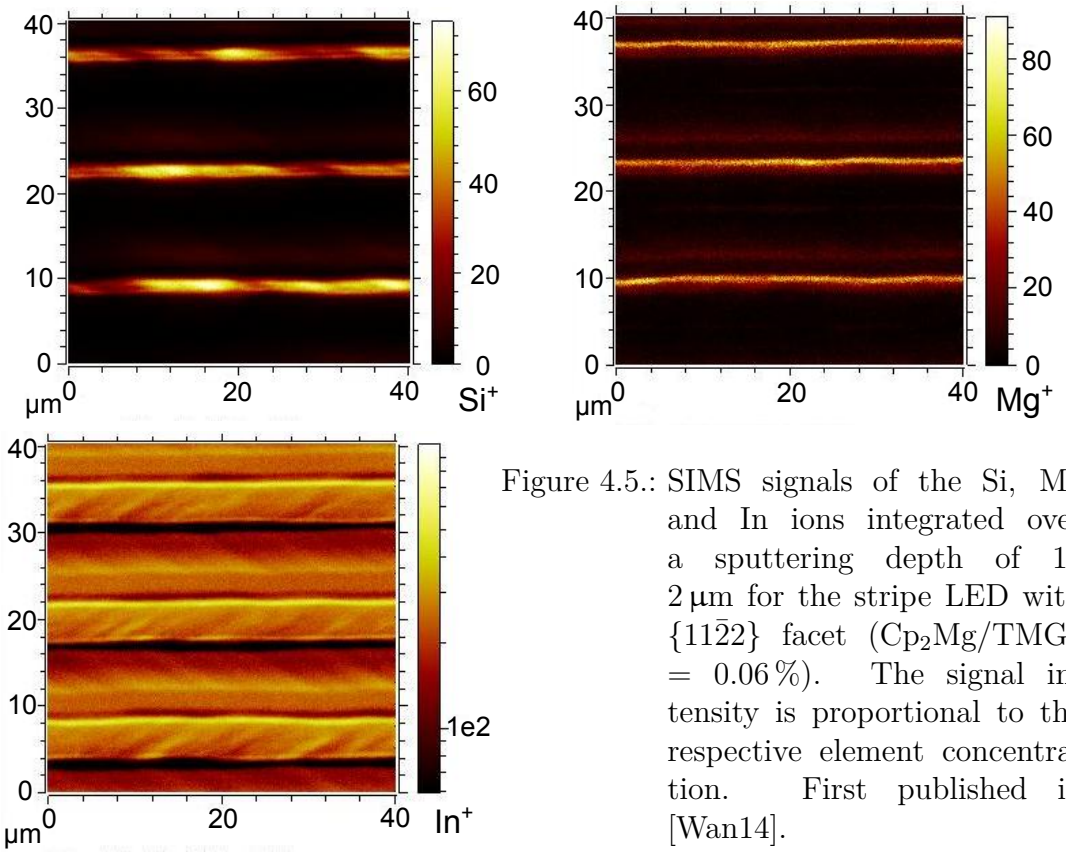

Figure 4.5.: SIMS signals of the Si, Mg and In ions integrated over a sputtering depth of 1–2 µm for the stripe LED with $\{11\bar{2}2\}$ facet (Cp_2Mg/TMGa = 0.06 %). The signal intensity is proportional to the respective element concentration. First published in [Wan14].

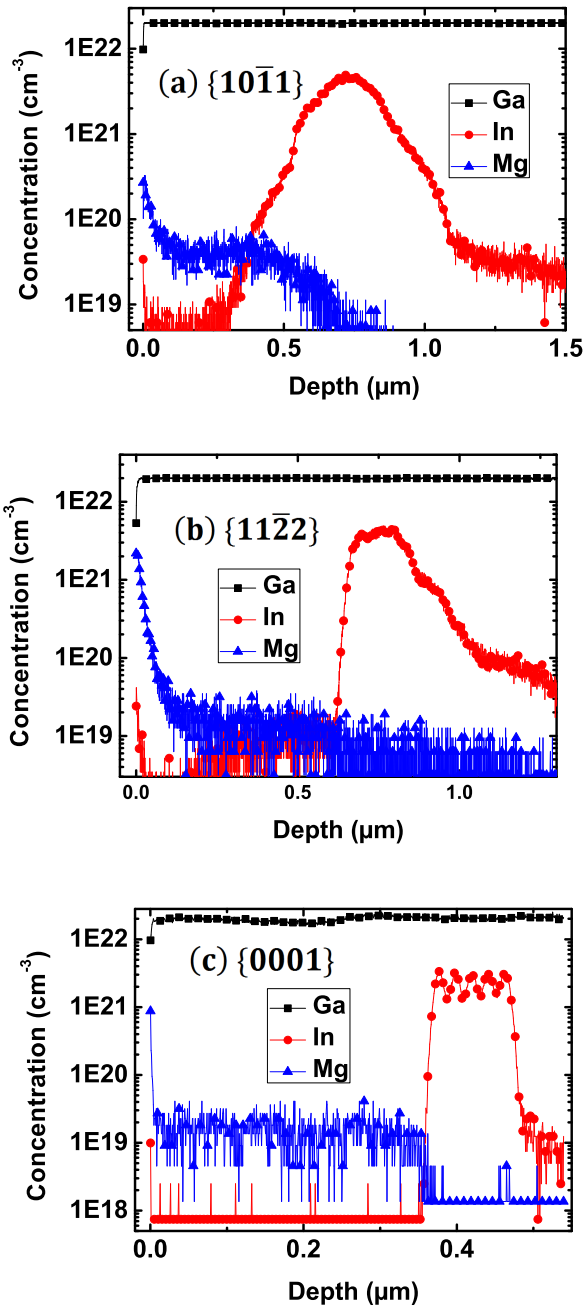

Figure 4.6.: SIMS depth profiles of the Ga, Mg and In concentrations for the stripe LEDs with $\{10\bar{1}1\}$ (a) and $\{11\bar{2}2\}$ (b) facets and the c-plane LED (c) at the same growth conditions ($Cp_2Mg/TMGa = 0.06\,\%$). First published in [Wan14].

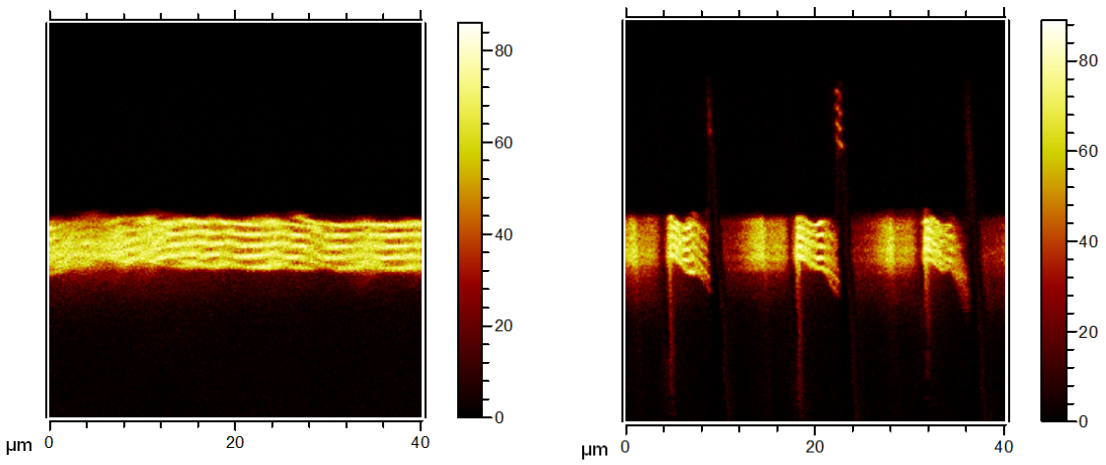

Figure 4.7.: The SIMS signal for the element indium of the semipolar stripe LEDs in the cross sections along (left) and perpendicular (right) to the stripes. First published in [Wan14].

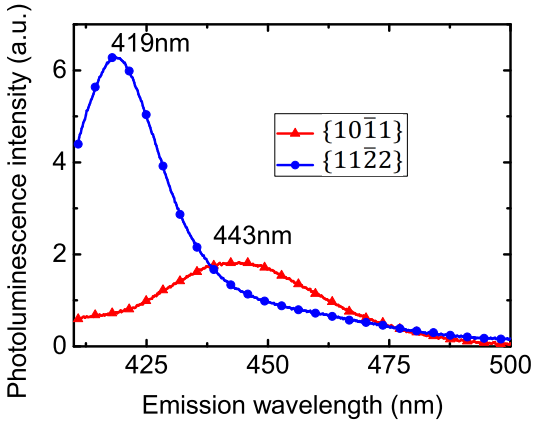

Figure 4.8.: PL spectra of the QW emission of the stripe LEDs measured at RT and with a 405 nm excitation source. First published in [Wan14].

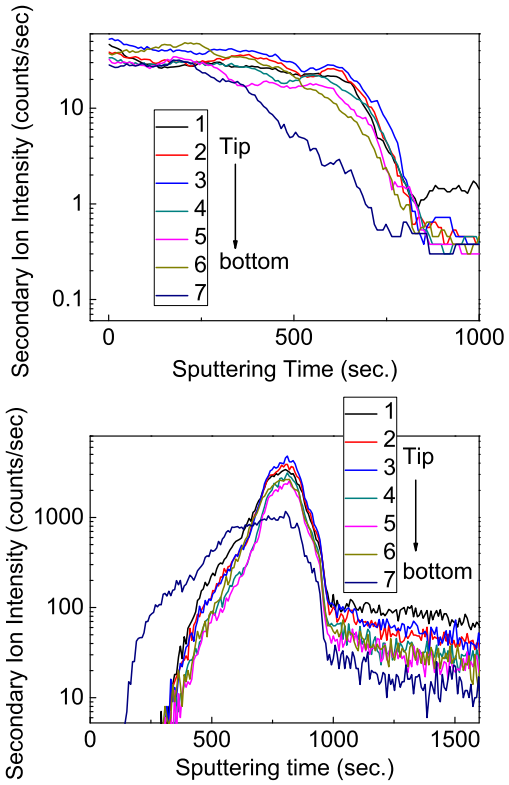

Figure 4.9.: SIMS signal for the element indium of the semipolar stripe LEDs in the cross sections along (upper) and perpendicular (lower) to the stripes.

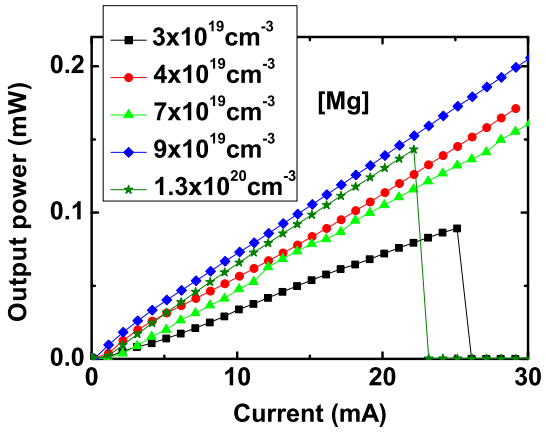

Figure 4.10.: EL output power of the stripe LEDs with the $\{10\bar{1}1\}$ facet with varying Cp_2Mg/TMGa ratio during the main p-GaN layer growth. First published in [Wan14].

the stripes and periodically separated by the SiO_2 epi-mask in the cross section perpendicular to the stripes. The indium concentration is measured by SIMS to be higher by about 30 % on the $\{10\bar{1}1\}$ facet than on the $\{11\bar{2}2\}$ facet. Resonant PL was applied to the stripe LEDs at RT with a 405 nm excitation source to penetrate the p-GaN to excite the QWs. The QW emission wavelength on the $\{10\bar{1}1\}$ facet is determined to be 443 nm, longer than 419 nm on the $\{11\bar{2}2\}$ facet (Fig. 4.8). Since the strength of the piezoelectric field and the QW thickness almost don't differ between the two types of semipolar facets, one can conclude higher indium incorporation efficiency on the $\{10\bar{1}1\}$ facet than on the $\{11\bar{2}2\}$ facet, consistent with the SIMS measurement and previous findings [Wun11].

In order to study the influence of the Mg concentration on the EL performance of the stripe LED with the $\{10\bar{1}1\}$ facet, Cp_2Mg/TMGa was chosen to be 0.04 %, 0.06 %, 0.10 %, 0.15 % and 0.21 % during the main p-GaN layer growth for five samples (samples #1–5). The Mg concentration is expected to depend on the Cp_2Mg/TMGa linearly [Ama90]. The Mg concentrations of samples #1 and #3–5 are estimated based on the Mg concentration of $4\times10^{19}\,cm^{-3}$ for sample #2 characterized by imaging SIMS. EL is measured for all five stripe LEDs with the $\{10\bar{1}1\}$ facet (Fig. 4.10). The EL output power is low with a too low Mg concentration of $3\times10^{19}\,cm^{-3}$, probably due to the inferior hole injection efficiency, and stays almost constant with Mg concentration ranging from $4.0\times10^{19}\,cm^{-3}$ to $1.3\times10^{20}\,cm^{-3}$ for the 3D LEDs with the $\{10\bar{1}1\}$ facet. Obviously, it is not critical to control the Mg doping concentration very accurately to achieve high EL output power. A Mg doping concentration window between $4.0\times10^{19}\,cm^{-3}$ and $1.3\times10^{20}\,cm^{-3}$ could offer good enough hole conductivity aiming at high EL output power.

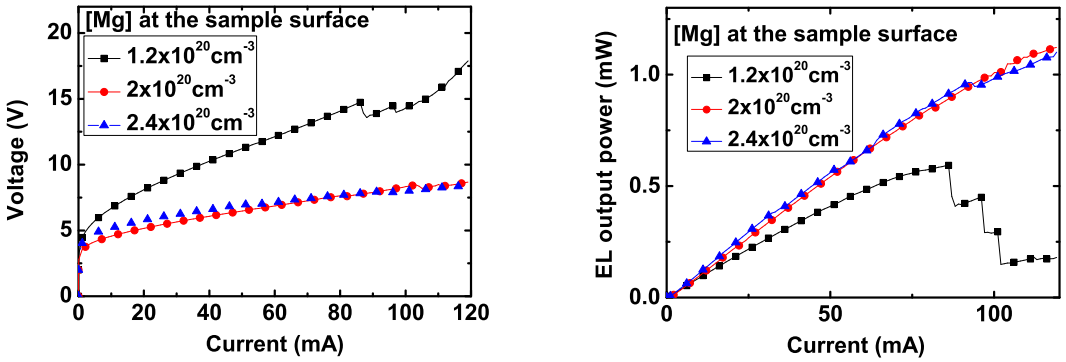

Figure 4.11.: I-V curve (left) and light output power (right) of the stripe LED with $\{10\bar{1}1\}$ facet varying the Mg concentration at the interface between the p-type semiconductor and the metal contact. First published in [Wan14].

In short, SIMS analysis revealed the Mg concentration of the 3D semipolar p-GaN, indicating a higher Mg doping concentration on the $\{10\bar{1}1\}$ facet by a factor of 2.7 as compared to the $\{11\bar{2}2\}$ facet under the same growth conditions. The In incorporation

efficiency is found to be about 30 % higher on the $\{10\bar{1}1\}$ facet than on the $\{11\bar{2}2\}$ facet by both methods of SIMS and PL. The EL output power is low for a too low Mg concentration of $3 \times 10^{19}\,\mathrm{cm}^{-3}$, probably due to the inferior hole injection efficiency and stays almost constant for the Mg concentration ranging from $4 \times 10^{19}\,\mathrm{cm}^{-3}$ until $1.3 \times 10^{20}\,\mathrm{cm}^{-3}$ for the 3D LEDs with the $\{10\bar{1}1\}$ facet.

4.4. p-doping in p-contact layer

Low contact resistance is crucial for the high performance of GaN-based LEDs to avoid heating at the pn-junction. With a high contact resistance, lots of heat are generated at the contact due to ohmic losses and increase the temperature of the pn-junction leading to a reduced efficiency of LEDs. This problem gets more pronounced for high-power LEDs operated at high current density. It is much easier to achieve an ohmic behavior for the n-GaN/metal contact than the metal contact to the p-GaN. Hence, we focus on the p-GaN/metal contact in this section.

Contacting a metal to the GaN layer results in a bending of the valence and conduction bands within the semiconductor and a Schottky barrier for the carriers forms at the interface. The Schottky barrier Φ_B can be calculated as

$$\Phi_\mathrm{B} = (\chi + E_\mathrm{g}) - \Phi_M \tag{4.2}$$

for the p-doped GaN, where χ is the electron affinity of the semiconductor, E_g the band gap of the semiconductor and Φ_M the work function of the metal. This expression is valid for an ideal Schottky diode. Another phenomenon – Fermi level pinning – occurs when there is a high density of interface states within the forbidden band of the semiconductor. The metal denotes a high quantity of electrons to the interface states in the semiconductor pinning the Fermi level to a certain distance to the valence band. In this case, an energy barrier is determined by the semiconductor band gap, independent of the metal property [Wei01].

The electron affinity χ of GaN is reported to be 4.1 eV with a band gap of 3.4 eV. No metal has a work function higher than 6 eV [Fik14]. Therefore, an energy barrier exists at the metal/p-GaN contact assuming the case of an ideal Schottky diode and obviously exists as well in the other case of Fermi level pinning.

Carrier tunnelling, thermionic-field emission and field emission are three main mechanisms for the carrier transport from the metal to the semiconductor over the energy barrier (Fig. 4.12). The difficulties to achieve an ohmic p-GaN/metal contact include the low mobility and low concentration of the holes in p-GaN suppressing the carrier tunnelling and the large barrier height reducing the possibility for the thermionic-field emission and the field emission. To enhance carrier transport via carrier tunnelling, a possible strategy could be to improve the p-conductivity of GaN whereas to optimize the metal scheme for a higher work function for better carrier transport via

thermionic-field emission and field emission. In this work, an additional p-GaN capping layer of about 10 nm is deposited on the main p-GaN layer. Excessive Mg doping, about an order of magnitude higher doping concentration than the optimum for good p-conductivity, is applied there leading to a deep-level-defect (DLD) band and the carriers are transported from the metal contact to the p-GaN capping layer through the DLD band instead of overcoming a Schottky barrier [Wu13].

Cp_2Mg/TMGa was ramped up from 0.06 % for the main p-GaN layer growth to 0.80 %, 1.34 % and 1.60 % during the growth of the p-GaN capping layer for three stripe LEDs with $\{10\bar{1}1\}$ facet. The Mg concentration at the sample surface, in other words, at the p-GaN/metal interface, was measured to be about $2 \times 10^{20}\,\mathrm{cm}^{-3}$ for the second sample by SIMS. With a linear extrapolation, the Mg concentration at the sample surface is estimated to be $1.2 \times 10^{20}\,\mathrm{cm}^{-3}$ and $2.4 \times 10^{20}\,\mathrm{cm}^{-3}$ for the first and third samples, respectively.

The complete LED device can be modeled as a Schottky diode and a pn-diode connected in series if there is a Schottky barrier between the p-GaN and the metal contact. The relation between the voltage V and the current I is expressed by the equation:

$$V = \sum \frac{n_i k T}{q} \ln\left(\frac{I + I_{si}}{I}\right), i = 1, 2. \tag{4.3}$$

n, k, T, q and I_s represent the ideality factor, Boltzmann's constant, the absolute temperature, the elementary charge and the saturation current of the diode, respectively. Two items with $i = 1$, 2 stand for the voltage over the pn junction and the Schottky barrier at the p-type contact. Hence, the knee voltage of the complete device is the summation of the knee voltages of the pn junction and the Schottky barrier between the p-GaN and the metal contact.

The knee voltage of the stripe LEDs with the $\{10\bar{1}1\}$ facets is determined from their I-V curves (Fig. 4.11, left). It drops from 6.3 V to 4.3 V by increasing the Mg concentration from $1.2 \times 10^{20}\,\mathrm{cm}^{-3}$ to $2.0 \times 10^{20}\,\mathrm{cm}^{-3}$ (Table 4.1). In the latter case, excessive Mg doping leads to a DLD band in the p-GaN capping layer and the carriers are transported from the metal contact to the p-GaN capping layer through the DLD band instead of overcoming the Schottky barrier. The Schottky barrier at the p-GaN/metal hinders the carrier transport in the sample with the low Mg doping level of $1.2 \times 10^{20}\,\mathrm{cm}^{-3}$ leading to a high knee voltage. The contact resistance is also higher in this case indicated by the slope of the I-V curve after the diode switch-on compared to the other two samples with larger Mg concentrations. Thus, heat is generated due to the poor contact performance during the EL leading to a high junction temperature. The generated heat is reduced when the LED is operated at a pulsed current as compared to cw current. As a result, the diode breaks down at a small operating current of 85 mA (Fig. 4.11, right) and the emission efficiency is lower when operated with a cw current compared to a pulsed current (Fig. 4.13). The employed pulsing current has a frequency of 10 kHz and a duty cycle of 1 %. With an even higher Mg

concentration of $2.4 \times 10^{20}\,\mathrm{cm}^{-3}$, the knee voltage rises again to 5.0 V . The contact performance deteriorates slightly, presumably due to the crystal quality degradation with a too high Mg doping level.

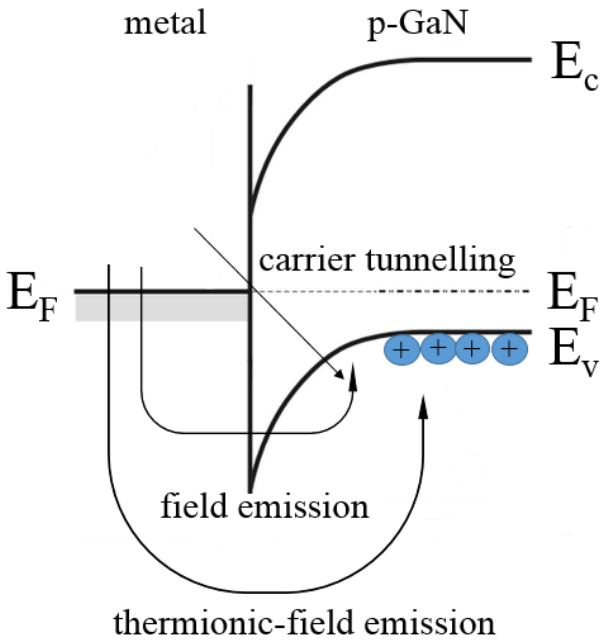

Figure 4.12.: Band diagram of the metal/p-GaN interface with different mechamisms of the carrier transport.

The electrical efficiency (EE) is the ratio between the wall plug efficiency and the external quantum efficiency which is described in details in section 6.1. It increases when the fraction of the energy consumed on the series resistor connecting to the diode decreases. The EE improves with better contact performance as expected (Fig. 4.14).

Obviously, the p-type contact performance was improved by excessive Mg doping.

Table 4.1.: Knee voltage of the stripe LED with the $\{10\bar{1}1\}$ facet while varying the Mg concentration at the p-GaN/metal interface.

Cp_2Mg/TMGa (%)	Mg concentration (cm^{-3})	knee voltage (V)
0.80	1.2×10^{20}	6.3
1.34	2×10^{20}	4.3
1.60	2.4×10^{20}	5.0

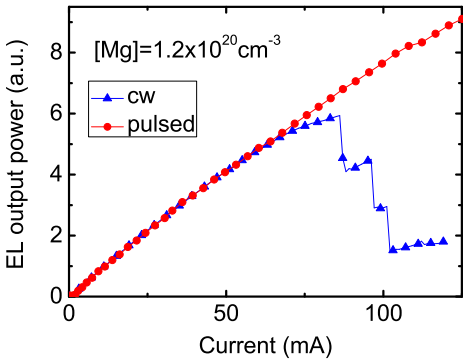

Figure 4.13.: EL output power of the stripe $\{10\bar{1}1\}$ LED with a Mg concentration of $1.2 \times 10^{20}\,\mathrm{cm}^{-3}$ at the p-GaN/metal interface under cw and pulsed currents. First published in [Wan14].

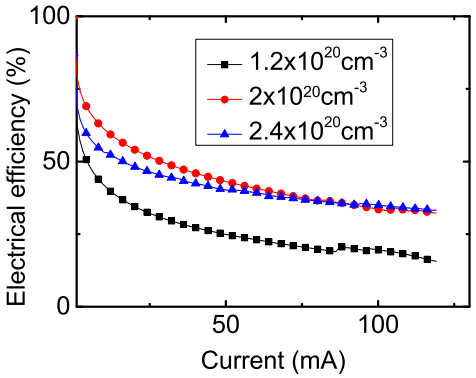

Figure 4.14.: Electrical efficiency of the stripe $\{10\bar{1}1\}$ LED while varying the Mg concentration at the p-GaN/metal interface.

5. Green converter structure

As mentioned, high power InGaN/GaN-based green LEDs attract worldwide interest nowadays. Two aspects are most important: to improve the efficiency of the InGaN/GaN QWs and to avoid the 'droop' effect at high current densities.

The efficiency of the InGaN/GaN QWs decreases drastically with increasing emission wavelength. The reasons have been discussed partly to be the polar character of the nitride semiconductors (cf. section 2.6.2) and partly to be the degraded material quality of InGaN with an increasing indium content.

The droop problem is typically identified as an EL efficiency maximum obtained at comparably small current densities of about $10\,\mathrm{A/cm^2}$ in GaN-based LEDs and a continuously decreasing efficiency at higher current densities [She07]. Auger recombination as a nonradiative recombination overwhelms at high carrier density and is discussed as the most important reason for the droop effect by the scientific community (cf. section 6.1.1). In order to mitigate the droop effect, one solution is to decrease the carrier concentration in the QWs, which requires either wider or more QWs. While semipolar structures allow wider QWs compared to polar structures, an increase of the number of QWs in LED structures is difficult due to the strongly different injection efficiencies of electrons and holes from the *n*- and the *p*-side of the diode, respectively. This issue is aggravated for high In content QWs. However, this can be circumvented by optical excitation of carriers leading to the idea of luminescence conversion structures with green light emitting InGaN QWs optically pumped with a highly efficient blue LED [Gal11]. Thus, a more homogeneous excitation of a larger amount of QWs can be achieved. Moreover, electron spill-over can be avoided in such electrically un-biased converter structures.

In this work, we investigate luminescence conversion structures with semipolar InGaN/GaN QWs based on our 3D inverse pyramidal structure (see section 3.4). The facet formation of the GaN inverse pyramids, $\{10\bar{1}1\}$, $\{11\bar{2}2\}$ or coexistence of both facets, and its effect on the QW quality is discussed. These structures have been mainly characterized by an optical transmission experiment, which enables the determination of the conversion ratio. Moreover, we enhanced the green emission of the conversion structure under optical excitation focusing mainly on the optimization of the InGaN growth condition. CL experiments in this chapter were done by I. Tischer in the Institute of Quantum Matter/Semiconductor Physics Group of Ulm University, Germany.

5.1. Stabilization of the $\{10\bar{1}1\}$ facet

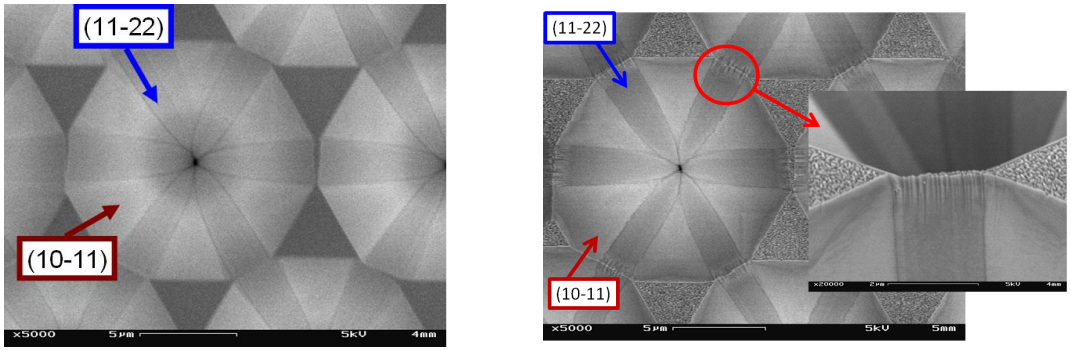

Figure 5.1.: Top view of the structure with both types of facets $\{10\bar{1}1\}$ and $\{11\bar{2}2\}$ before (left) and after (right) the growth of 5 InGaN/GaN QWs. The area close to the apex on the $\{11\bar{2}2\}$ facet is enlarged in the insert in the right-hand figure. First published in [Wan13].

The crystal planes $\{10\bar{1}1\}$ and $\{11\bar{2}2\}$ are naturally stable semipolar facets for GaN inverse pyramids. Under reasonable growth conditions, both types of crystal planes coexist and 12 facets form on the surfaces (Fig. 5.1). However, for such long wavelength QWs with fairly large In content of about 24 %, we typically observe some roughening of the surface near the apex of the $\{11\bar{2}2\}$ facets having the shape of ministripes oriented along the crystal direction $\langle 10\bar{1}x\rangle$ (see insert in Fig. 5.1, right), whereas the ridges between adjoining $\{10\bar{1}1\}$ facets remain sharp. The ministripes are caused by basal-plane stacking faults (BSFs) and dislocation arrays within the QWs underneath, as cross-sectional TEM images (shown later in section 5.4.1) suggest. Consequently, these regions show low luminescence intensity in spatially resolved cathodoluminescence (CL). Locally resolved spectra on such a $\{11\bar{2}2\}$ facet was measured within 8 excitation windows from top to bottom (Fig. 5.2). The emission from the topmost excitation window – where we observe the mini-stripes – is relatively week and broad. From the second to the lowest excitation window, the emission is fairly strong and narrow with slightly decreasing intensity and a blue-shifting wavelength from top to bottom. Obviously, the mini-stripes developing during the InGaN/GaN MQW growth degraded the QW quality causing a weak and broad emission. In order to achieve QWs with high luminescence intensity we decided to prevent the emergence of such ministripes by suppressing the $\{11\bar{2}2\}$ facets on the GaN inverse pyramids.

Three parameters were varied during the growth of the GaN inverse pyramids and their influence of the facet formation was investigated: temperature, V/III ratio, and the filling factor of the SiO_2 mask (the ratio of the masked area over the total surface area).

When decreasing the growth temperature from 1120 °C to 950 °C, we observe a steady transition from purely $\{11\bar{2}2\}$ facets to the increased appearance of $\{10\bar{1}1\}$

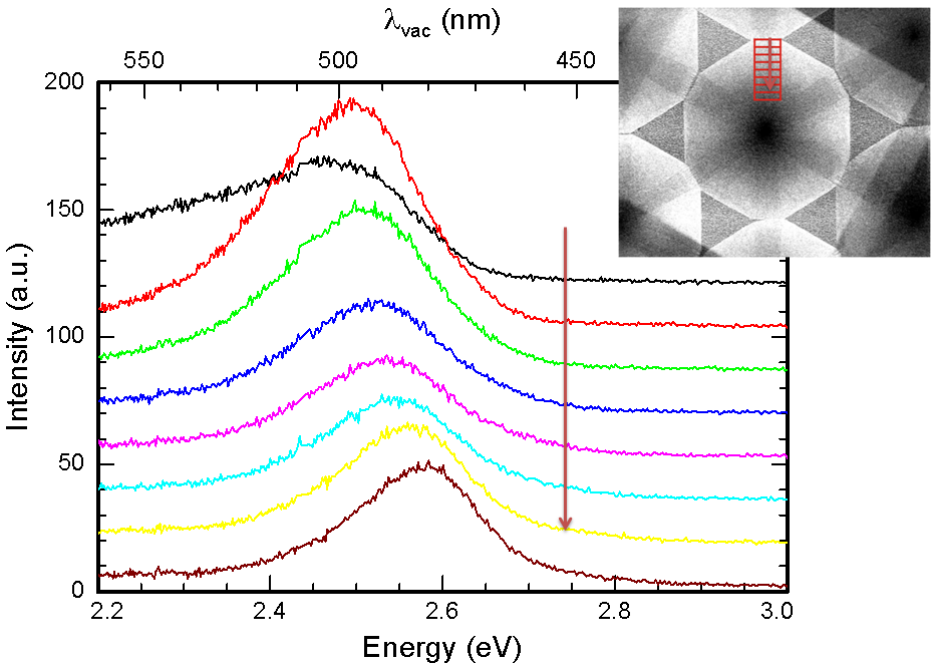

Figure 5.2.: CL linescans on a $\{11\bar{2}2\}$ facet from top to bottom. The insert shows a SEM top view on the investigated facets with the respective fields marked, in which the spectra have been measured.

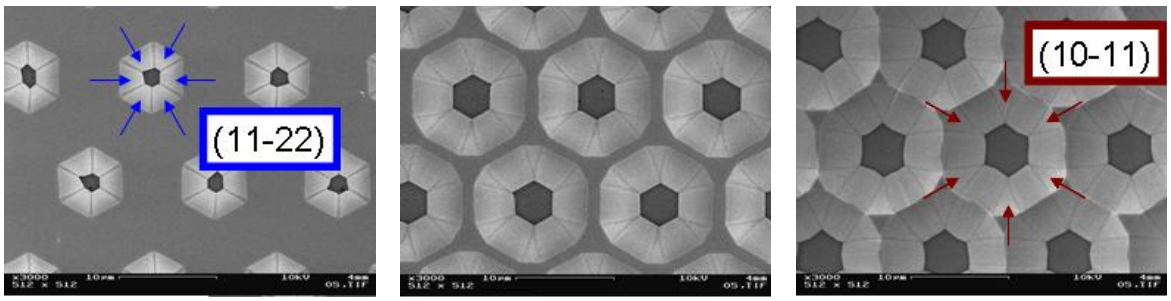

Figure 5.3.: Top view of GaN inverse pyramids grown at a temperature of 1120 °C (left), 1060 °C (middle) and 950 °C (right). First published in [Wan13].

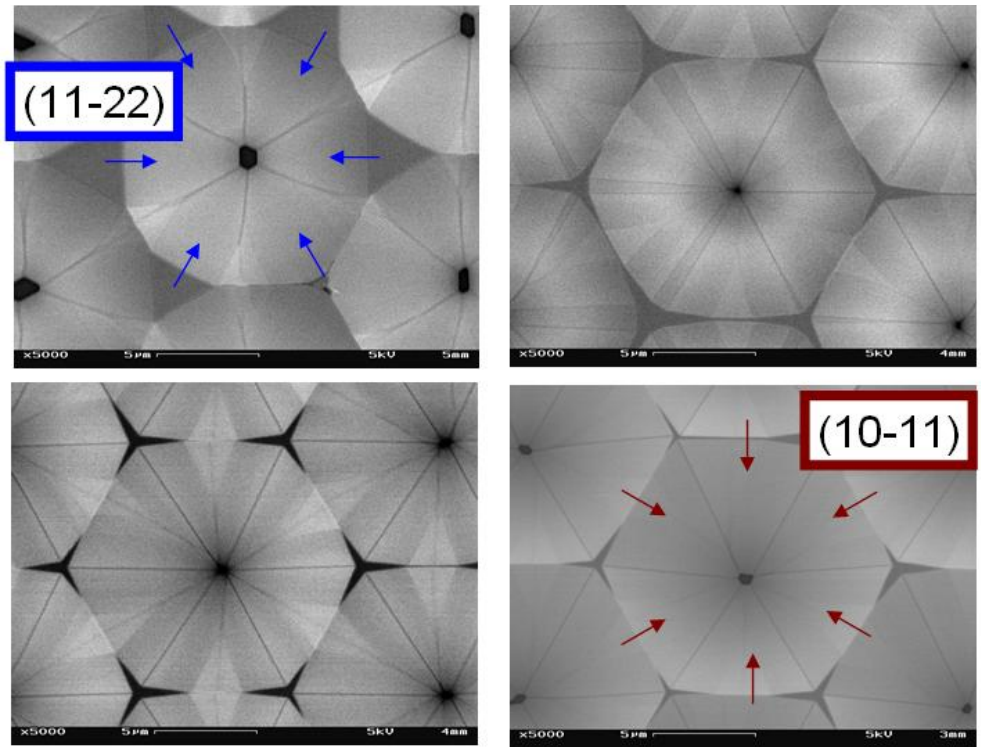

Figure 5.4.: Top view of GaN inverse pyramids grown with a V/III ratio of 200 (upper left), 400 (upper right), 500 (lower left) and 700 (lower right). First published in [Wan13].

facets (Fig. 5.3). Similarly, the GaN inverse pyramidal surface is dominated by the $\{11\bar{2}2\}$ facet for a small V/III ratio of 200, getting gradually suppressed with increasing V/III ratio (Fig. 5.4). Finally, the $\{11\bar{2}2\}$ facet disappeared when the mask filling factor (see Equ. 3.2) was reduced from 59 % to 25 % (Fig. 5.5), speculatively due to a different local V/III ratio at growth point.

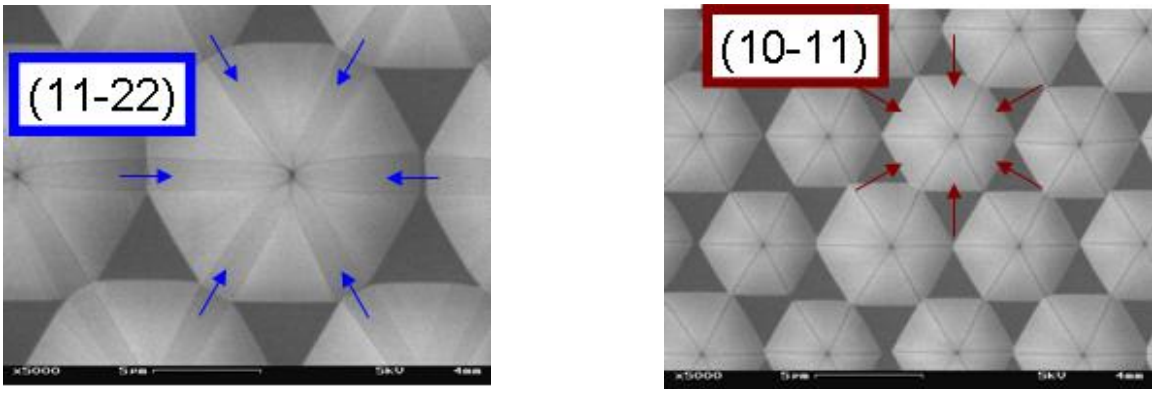

Figure 5.5.: Top view of GaN inverse pyramids with a mask filling factor of 59 % (left) and 25 % (right). First published in [Wan13].

By applying a proper combination of the 3 parameters discussed above (temperature of 950 °C, V/III ratio of 400 and mask filling ratio of 59 %), the $\{11\bar{2}2\}$ facet was totally suppressed for a pure GaN structure without QWs (Fig. 5.6, left). Moreover, the PL intensity of this structure with 5 InGaN/GaN QWs is higher than that of the structure grown with all the optimized parameters (temperature of 950 °C, V/III ratio of 700 and mask filling ratio of 25 %). Therefore, the former parameter set is chosen for the all the inverse pyramidal converter structures in this work. Again, spectra were obtained from 8 excitation windows from top to bottom in CL (Fig. 5.7) for the converter structure with 5 InGaN/GaN QWs (Fig. 5.6, right). The emission shows the trend of continuously decreasing intensity and blue-shifted wavelength from top to bottom without exceptions. The area within the first excitation window contributes the strongest emission without suffering from the mini-stripes. The integrated PL of these structures peaking at 505 nm is about 50 % more intense as compared to the structure with the mini-stripes peaking at 494 nm.

In the top view of a structure without the $\{11\bar{2}2\}$ facet, but still grown with fairly low V/III ratio and high mask filling ratio, three parts (one triangle and two symmetric neighboring parts as marked in Fig. 5.6) are observed within any of the 6 equivalent surface areas after the growth of the GaN layer below the quantum wells. The central triangle part is attributed to the facet $\{10\bar{1}1\}$ since its upper edge is parallel to the crystal direction $\langle 11\bar{2}0\rangle$ indicated by the growth mask alignment. The neighboring part could be either one single facet rotated by a slight angle with respect to the $\{10\bar{1}1\}$ facet or several small facets with tiny misorientations among them. However, seemingly only one pure $\{10\bar{1}1\}$ facet remains after the deposition of the 5 InGaN/GaN

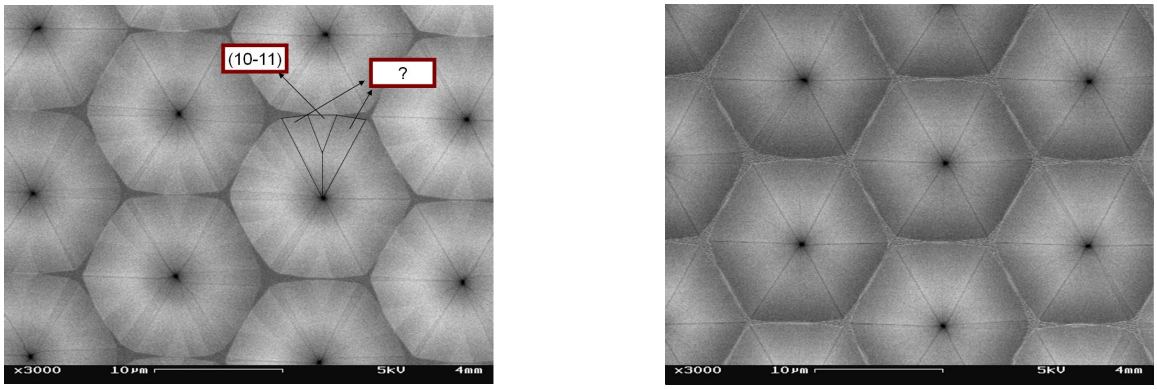

Figure 5.6.: Top view of the structure without $\{11\bar{2}2\}$ facets before (left) and after (right) the InGaN/GaN QW growth. The three parts in any of the 6 equivalent surface areas are marked. The central triangular part is attributed to the $\{10\bar{1}1\}$ facet. The other parts are attributed to high-index facets very close to $\{10\bar{1}1\}$. First published in [Wan13].

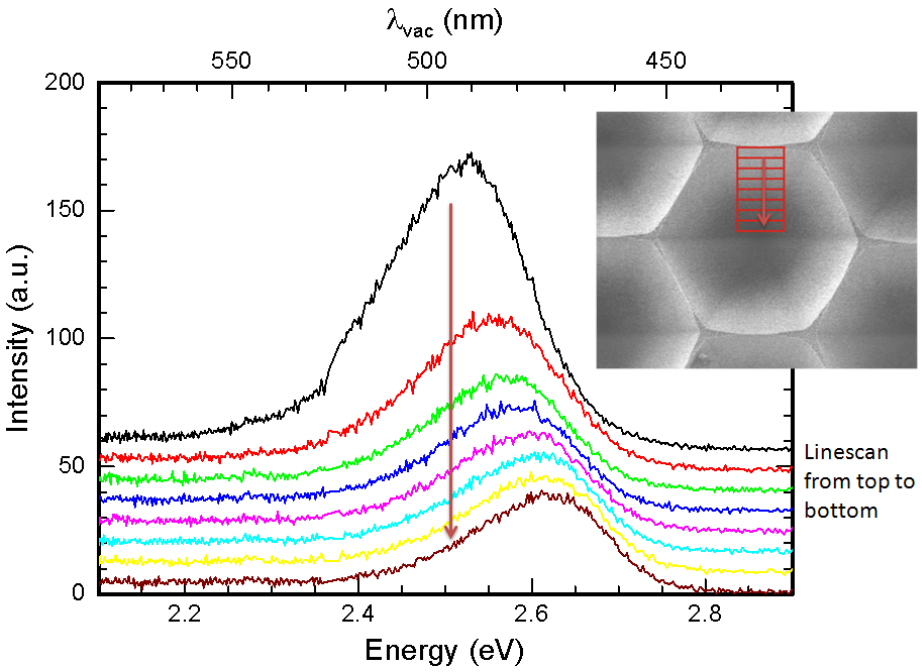

Figure 5.7.: CL linescan on the $\{10\bar{1}1\}$ facet from top to bottom. Insert shows again the areas in which the spectra have been acquired.

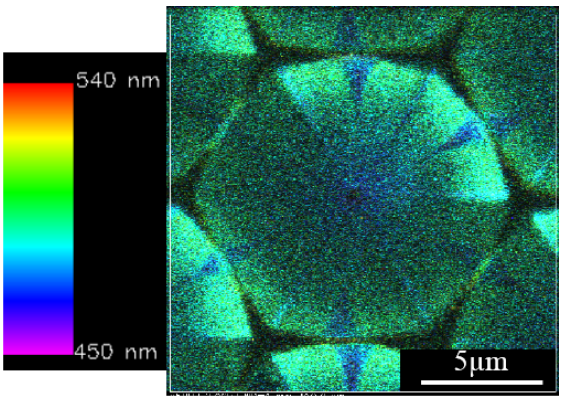

Figure 5.8.: CL mapping of the structure with 3 sub-facets after InGaN/GaN QW growth.

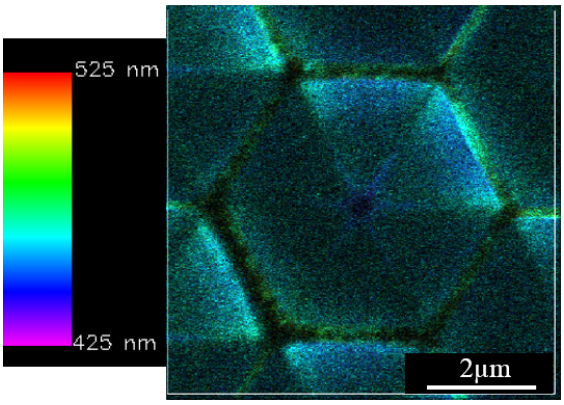

Figure 5.9.: CL mapping of the structure with exclusively $\{10\bar{1}1\}$ facets after InGaN/GaN QW growth.

QWs (Fig. 5.6, right). In spatially resolved CL mapping (Fig. 5.8) of the same structure with the 5 InGaN/GaN QWs, the 3 sub-facets are clearly resolved with longer emission wavelength from the two sub-facets as compared to the central triangle part. This may be explained by different In incorporation as a result of different surface orientations [Per09] needing more detailed studies. By increasing the V/III ratio to 700 and decreasing the mask filling ratio to 25 %, the two neighboring parts are suppressed and GaN inverse pyramids with exclusively $\{10\bar{1}1\}$ facets have been achieved (Fig. 5.9).

5.2. Transmission experiments

Along these findings, we have grown green converter structures, typically containing multi InGaN/GaN QW without doping. These green converters were characterized by transmission experiments. The light beam of a 405 nm blue laser diode is coupled into the converter samples in some cases from the sapphire-side of the wafer (forward excitation). The transmitted blue and converted green light are detected from the epi-side. The absorption fraction η_a (the intensity ratio between the absorbed and incoupled blue light) and the conversion rate η_c (the intensity ratio between the converted green and the absorbed blue light) can be determined. They are figures of merit for the QW absorption capability and the QW emission quality, respectively. The relation between the converted green and incoupled blue light can be expressed by the following equation:

$$I_{\text{converted,g}} = I_{\text{incoupled,b}} \cdot \eta_a \cdot \eta_c \tag{5.1}$$

A similar sample without any InGaN/GaN QWs was taken as a reference to compensate the light back-scattering at each interface along the light path since the light incoupling and outcoupling efficiencies are assumed to be equal for the green converter and the reference sample. The absorption fraction η_{a} is calculated from the intensities of the outcoupled blue light for the green converter and the reference sample, indicated by $I_{\mathrm{outcoupled,b}}$ and $I_{\mathrm{outcoupled,b,r}}$, respectively:

$$\eta_{\mathrm{a}} = \frac{I_{\mathrm{outcoupled,b,r}} - I_{\mathrm{outcoupled,b}}}{I_{\mathrm{outcoupled,b,r}}} \tag{5.2}$$

Assuming that the outcoupling efficiency η_{e} is equal for the blue and green light, the calculation of the conversion rate η_{c} can be expressed as:

$$\eta_{\mathrm{c}} = \frac{I_{\mathrm{converted,g}} \cdot \eta_{\mathrm{e}}}{I_{\mathrm{absorbed,b}} \cdot \eta_{\mathrm{e}}} = \frac{I_{\mathrm{outcoupled,g}}}{I_{\mathrm{outcoupled,b,r}} - I_{\mathrm{outcoupled,b}}} \tag{5.3}$$

The overall intensity of the outcoupled light in front of the sample is calculated by integrating the light intensity per unit area over the semispheric surface. As shown in Fig. 5.10, the outcoupled blue light is distributed center-symmetrically with a six-fold pattern as a consequence of our hexagonal pyramidal surface structure. Hence, the mapping of the area-normalized light intensity is performed via angle-resolved measurements in two directions indicated as A (the radial direction) and B (the circular direction) in Fig. 5.10. The case of the outcoupled green light is even simpler since its distribution is center-symmetrical and constant along the circular direction. The measurement has been applied with an increment of 10 ° in the radial direction at two positions with the maximum and minimum blue light intensities along the circular direction (Fig. 5.11).

The absorption coefficient α can be calculated from the absorption fraction η_{a} by the equation:

$$1 - \eta_{\mathrm{a}} = e^{-2\alpha n L_Z} \tag{5.4}$$

where n and L_Z represent the number and the thickness of the QWs, respectively. Since our semipolar QWs are tilted by 60 ° with respect to the substrate surface, the path of the blue light through the QWs is actually twice of the QW thickness which gives the factor of 2 in equation 5.4. With the same QW number, the doubled light path in our tilted QWs compared to the planar ones results in a strong absorption of the blue light in our structures.

Back-scattering of sapphire

As discussed, a reference sample without any InGaN/GaN QWs was employed for the determination of the 405 nm laser absorption. By doing so, we assumed that the back-scattering of the 405 nm laser at the backside of the sapphire wafers is constant at different locations. 4 pieces of the sapphire wafers from the same manufacturer were

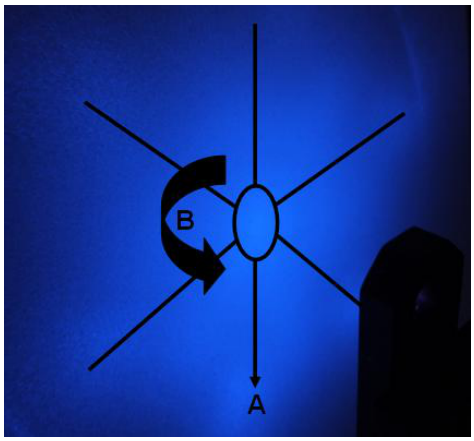

Figure 5.10.: The outcoupled blue light intensity distribution of the reference sample on a screen. The sample holder (black part at the right lower corner) indicates how the photo is taken: not straight facing the screen, but with a tilting angle to the screen. The six straight lines show the six-fold pattern with the center indicated by the ellipse. Two dimensional angle-resolved measurements are performed along the radial (A) and circular (B) directions. First published in [Wan13].

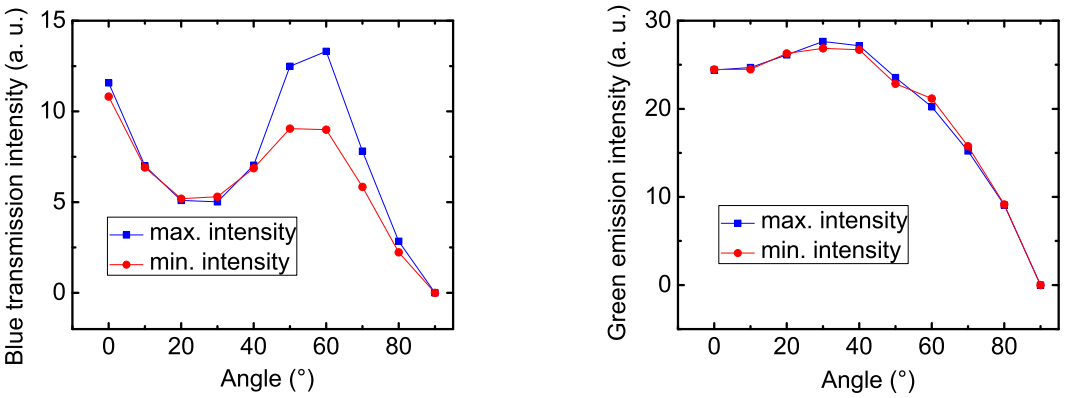

Figure 5.11.: The transmitted blue (left) and green (right) light intensities of the angle-resolved measurement for the green converter structure. The x-axis indicates the angle along the radial direction. The blue and red curves in each diagram belong to the positions with the maximum and minimum blue light intensities along the circular direction, respectively.

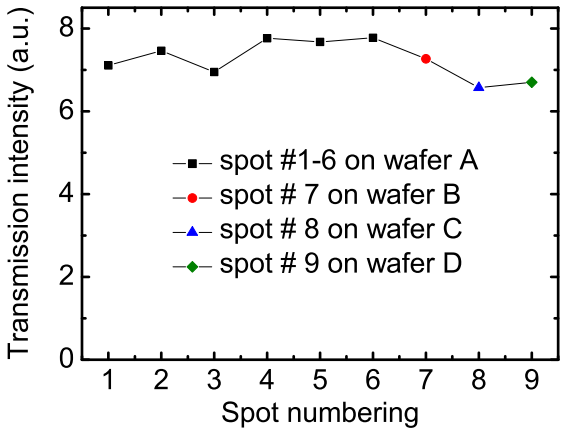

Figure 5.12.: Transmission intensity of c-plane sapphire wafers at spot # 1–6 on wafer A and spot #7–9 on wafer B, C and D each, under forward excitation. 4 pieces of the sapphire wafers are from the same manufacturer.

taken to check this assumption. The transmission intensity was measured to vary only in a small range of 18 % among spot # 1–6 on wafer A and spot # 7–9 on wafer B, C, D each, under forward excitation (Fig. 5.12). Therefore, our assumption is valid, however, still causes an error bar of 18 %.

Does SiO_2 absorb 405 nm laser?

Of course the suitable structure for a green converter should absorb the excitation light, in our case, the 405 nm laser, exclusively in the QWs. The sapphire and GaN are transparent at the light wavelength of 405 nm. How about the SiO_2 epi-mask which is employed to realize the 3D GaN structure via SAG? Does this SiO_2 layer deposited by PECVD absorb the 405 nm laser? To answer this question, we compared the transmission intensity of the green converter before and after the removal of the SiO_2 epi-mask. The $\{10\bar{1}1\}$ green converter based on the GaN stripes was etched for 20 mins in the solution of 8 % HF to remove the SiO_2 layer. The parallel GaN stripes are separated from each other by $\sim 3\,\mu m$ with the SiO_2 layer in between partly as the sample surface and the rest buried under the GaN stripes. The green converter based on the GaN inverse pyramid is not suitable for this experiment since its SiO_2 is embedded in the (In)GaN material completely. The SiO_2 layer is completely removed after etching (Fig. 5.13). Moreover, the five-fold InGaN/GaN QWs are not attacked, as resolved clearly in SEM at the top (Fig. 5.14). The transmission intensity even decreases slightly after the HF etching which is attributed to a different light scattering without the SiO_2 layer. This indicates that the SiO_2 epi-mask does not have a strong absorption of the 405 nm laser (Fig. 5.15).

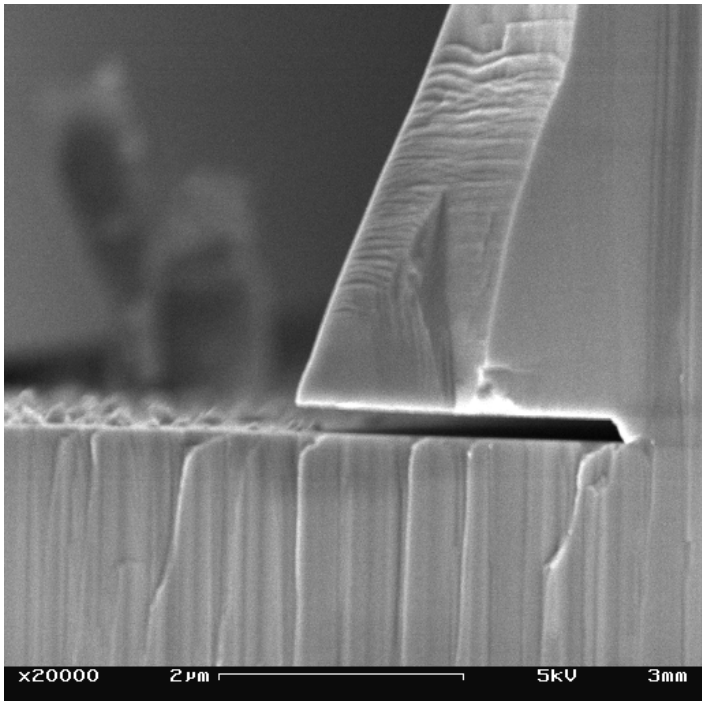

Figure 5.13.: Cross section of the green converter based on the GaN stripes after etching in a solution of 8 % HF for 20 mins at the bottom.

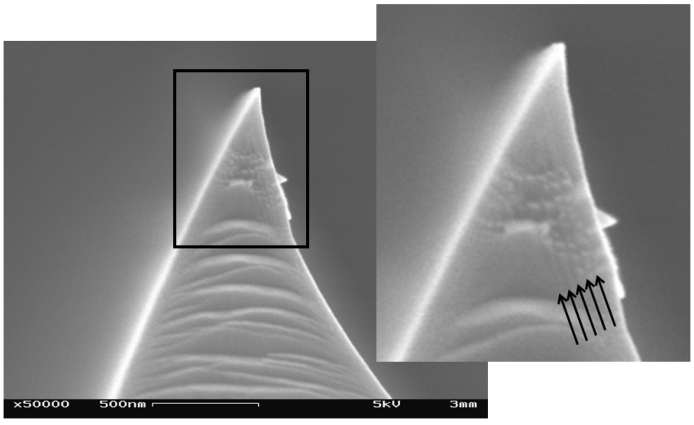

Figure 5.14.: Cross section of the green converter based on the GaN stripes after etching in a solution of 8 % HF for 20 mins at the top, insert showing resolved 5QWs.

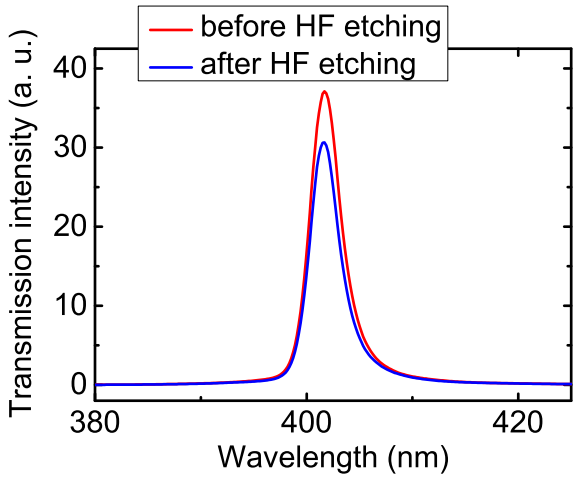

Figure 5.15.: The transmission intensity of the 405 nm laser for the green converter based on the GaN stripes before and after the HF etching.

5.3. InGaN/GaN QWs grown in MOVPE

The MOVPE growth of InGaN has its own challenges. TMIn, TEGa and NH_3 are used as the precursors with N_2 as the carrier gas. The binding energy of the chemical bonds in InN is weak resulting in a low decomposition temperature of InN leading to a N_2 equilibrium vapor pressure over the InN surface several orders higher than that over the GaN and AlN surface [Bhu03]. Therefore, a low InGaN growth temperature below 800 °C is normally required to suppress the thermal decomposition of InN to achieve sufficient indium incorporation for a long emission wavelength above 500 nm. The indium incorporation efficiency increases with decreasing growth temperature and vice versa. However, a low InGaN growth temperature reduces the cracking efficiency of NH_3. Hence, it is necessary to raise the V/III ratio during the InGaN growth as compared to GaN. Moreover, the migration mobility of the adatoms on the substrate surface is low at low growth temperature leading to a high defect density. The InGaN growth rate is then typically reduced to about 1 nm/min to compensate the low migration mobility. Nevertheless, the crystal quality is normally inferior for InGaN with the low growth temperature as one main reason.

As seen in the phase diagram of $In_xGa_{1-x}N$ (Fig. 5.16), the alloy is thermodynamically stable when the corresponding data point for certain indium concentration x and temperature T is above the line. Otherwise, the alloy is thermodynamically more stable when it separates into co-existing phases, some richer in InN and the others in GaN causing local indium composition fluctuation. The region under the line in the phase diagram is thermodynamically unfavorable for one-phase material and named as *miscibility gap*. Taking $\{10\bar{1}1\}$ InGaN/GaN QWs with the InGaN thickness of 2.5 nm as an example, 22 % indium is required to achieve the emission wavelength of

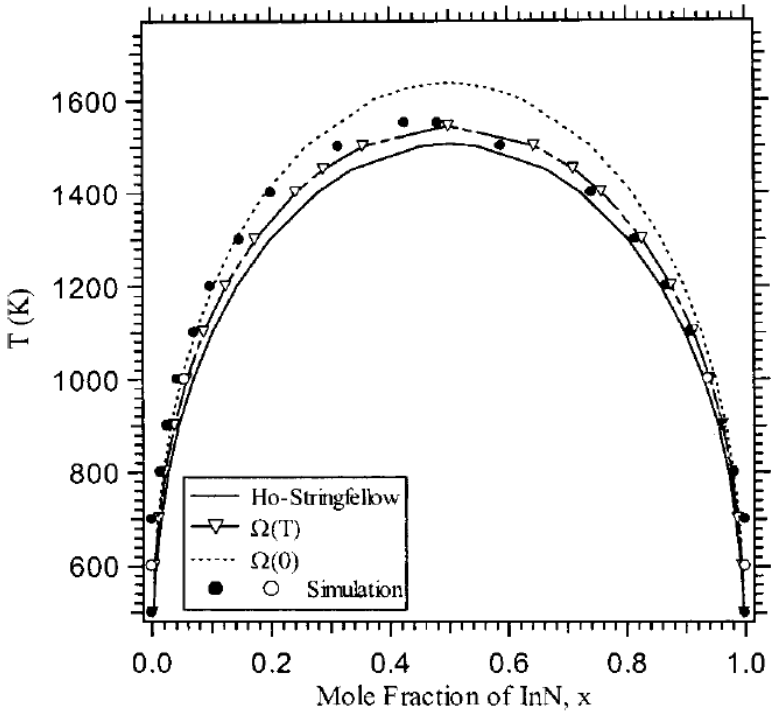

Figure 5.16.: Calculated miscibility diagram for the InGaN system according to different theories [Adh04].

504 nm according to calculations based on Equ. 2.3 and the polarization-induced band structure tilting. $In_{0.22}Ga_{0.78}N$ is actually within the miscibility gap even at growth temperature. Therefore, local indium composition fluctuations may be another reason for the degraded material quality of InGaN with high indium content aiming on the long-wavelength emission.

A pseudomorphically grown InGaN layer on GaN is compressively strained due to the lattice mismatch. When the thickness of the InGaN layer exceeds the critical thickness, strain is released via either defect generation or 3D growth mode. As known, defects act as nonradiative recombination centers in GaN and its alloys. The respective mechanism is discussed in section 6.1.1 with the topic called Shockley-Read-Hall recombination. The defects in the proximity of the active region are detrimental for the QW efficiency. Obviously, the critical thickness decreases with increasing indium content (Fig. 5.17). The growth of highly strained c-plane heterostructures often results in the formation of misfit dislocations at heterointerfaces while basal-plane stacking faults (BSFs) are typically generated in the nonpolar and semipolar structures. For the latter, the BSFs lie in the (0001) basal plane penetrating through the nonpolar and semipolar active region and even the pn-junction until the device surface in the case of LEDs and LDs acting as a current-leakage channel (shown in section 5.4.1). The strain relaxation pathway for nonpolar and semipolar structures is heavily under investigation [Hsu12, SH11, You10]. Very few investigations have been reported, how

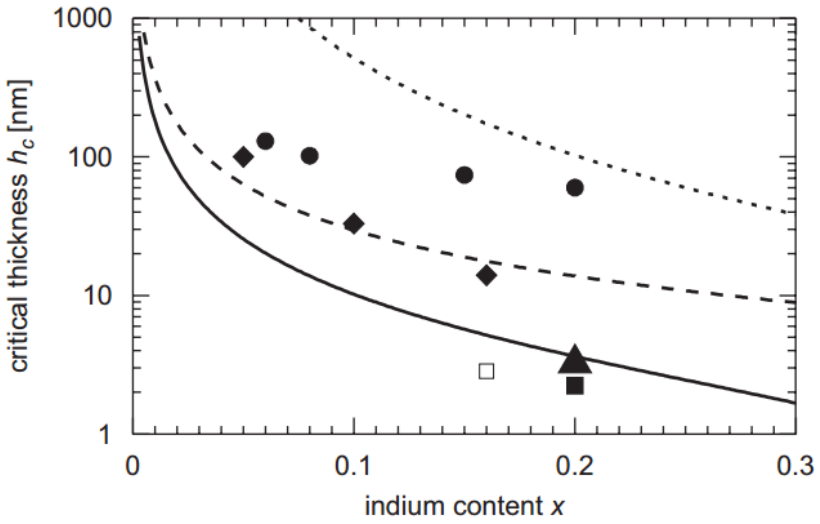

Figure 5.17.: Critical thickness values calculated for c-plane $In_xGa_{1-x}N$/GaN single-layer system using different models and experimentally obtained by PL and by TEM. [Hol07].

the critical thickness of InGaN on GaN changes depending on different nonpolar and semipolar facets, especially none on the $\{10\bar{1}1\}$ facet [SH12a, SH12b].

5.4. Brightness enhancement of green converters

In order to pump more green light out of the conversion structure, one may increase either the absorption fraction η_a of the excitation light or the conversion rate η_c or both as indicated by Equ. 5.1. For the former, a larger QW number, i.e. a larger total QW thickness, leads to a larger η_a. For the latter, better crystal quality of the InGaN QW contributes to a larger η_c. As discussed, a low temperature typically below 800 °C is required to grow the InGaN material with enough In content for green emission. Such high In content may be one main reason for the inferior crystal quality of the InGaN layer. In order to improve the InGaN quality, we tried to increase the QW growth temperature while keeping emission wavelength constant. This could be achieved by larger InGaN thickness, higher reactor pressure, higher flow and lower TEGa molar flow. The InGaN growth conditions optimized according to the conversion structure were integrated into the 3D semipolar LEDs leading to an enhanced EL output power by a factor of more than 3 which also proves the improved QW crystal quality.

5.4.1. QW number

As mentioned above, the possibility to increase the number of QWs is a significant advantage of such optically pumped structures, which increases the overall absorption of the excitation light and hence potentially the green light intensity. Therefore, 40-fold InGaN/GaN QWs were deposited on the tilted $\{10\bar{1}1\}$ facets of GaN inverse pyramids to form a green converter as suggested by the c-plane case [Gal11]. Interestingly, the ridge of the inverse pyramids emits at $\sim 555\,\text{nm}$ whereas the rest of the surface area emits at a shorter wavelength below 500 nm resulting in two separated peaks in the integrated CL spectrum (Fig. 5.18). Again, locally-resolved spectra were measured within 8 excitation windows from top to bottom along the $\{10\bar{1}1\}$ facet (Fig. 5.19). The topmost excitation window is located at the ring on the ridge which has a different tilting angle as compared to the rest surface area with respect to the c-plane substrate. Green emission at $\sim 555\,\text{nm}$ was detected from this ring on the ridge. The second excitation window covers the area with some mini-stripes on the $\{10\bar{1}1\}$ facet. On the same height, the mini-stripes are found also on the parasitic $\{11\bar{2}2\}$ facet. Similarly as observed in section 5.1, the area with the mini-stripes shows inferior luminescence intensity, in this case almost none. Greenish-blue emission was measured within the other 6 excitation windows with a slightly decreasing intensity and a blue-shifting wavelength from top to bottom.

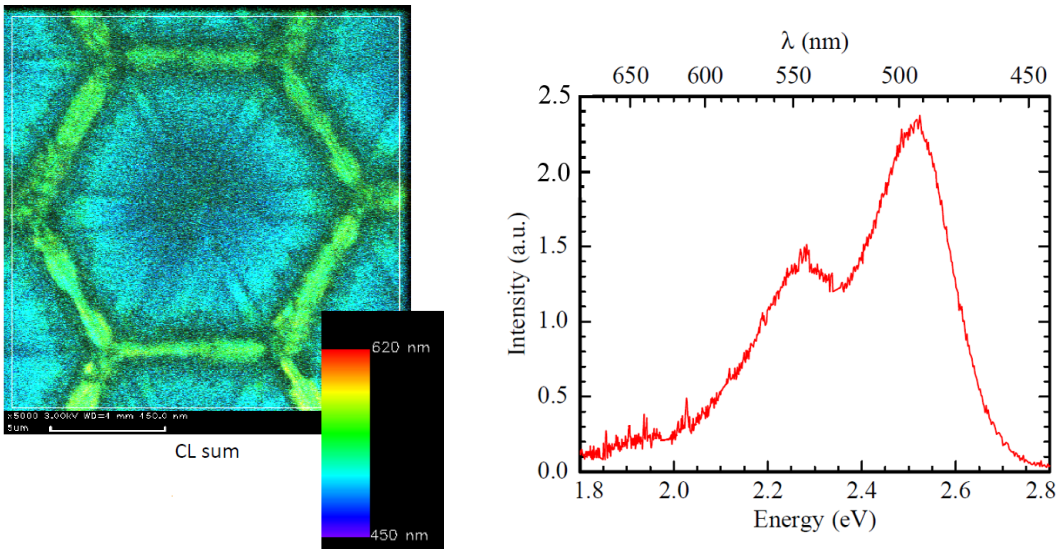

Figure 5.18.: CL mapping (left) and the corresponding integrated CL spectrum (right) of the conversion structure with 40-fold InGaN/GaN QWs.

TEM investigations have been done in the region close to the ridge to understand the luminescence behaviour of the conversion structure with 40-fold InGaN/GaN QWs (Fig. 5.20). Defects running almost in the horizontal direction start within the QWs. The facts that the planar features show a change in contrast and that they are terminated by partial dislocations indicate that they are BSFs (Fig. 5.21). The partial

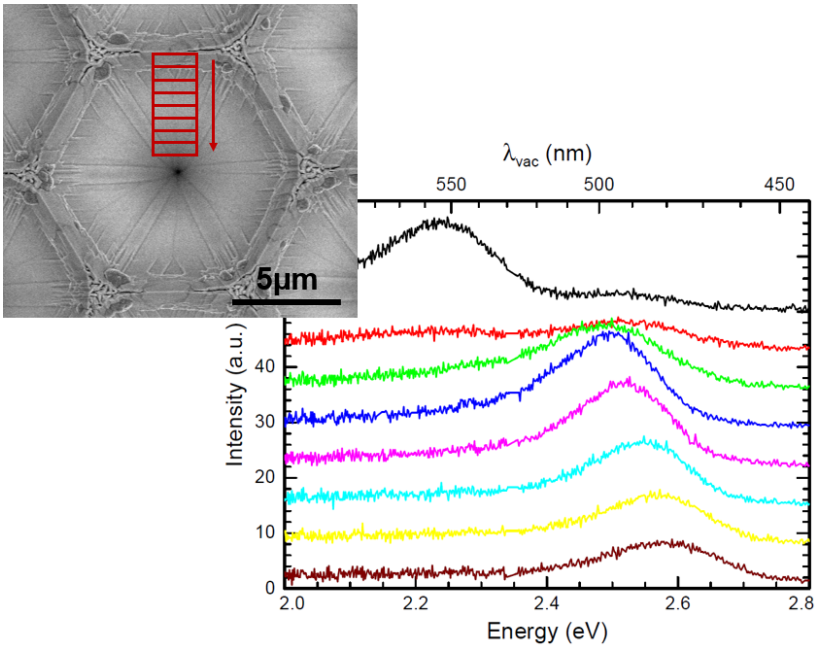

Figure 5.19.: CL linescans on a $\{10\bar{1}1\}$ facet from top to bottom. The insert shows the SEM top view on the investigated facets with the respective fields marked, in which the spectra have been measured.

dislocations at the end of the planar features form an array that runs diagonally over the QW structure. These defects within the QWs are generated to release the strain when the InGaN thickness exceeds the critical thickness. They start from the early grown QWs at the position close to the apex of the GaN inverse pyramids and shift to the late grown QWs gradually when the position moves to the bottom over the facet. This is due to the inhomogeneous strain distribution caused by the geometry of the apex. This part of the material with the BSFs and the partial dislocations corresponds to the surface area with the mini-stripes. The defects act as nonradiative recombination centers, being responsible for the inferior luminescence performance there. Electron diffraction patterns (Fig. 5.22) were taken at locations # 1–4 with constant sample orientation. The change in the diffraction patterns at locations # 2–4 as compared to that at location # 1 of the GaN inverse pyramids indicates the change in lattice orientation caused by the defects (Fig. 5.22). The lattice orientation change makes the QWs above the highly-defective material tilt more to the vertical direction up to $\sim 7\,^\circ$ corresponding to the differently tilted surface facet of the ring on the ridge. This part of the QWs has a higher indium incorporation efficiency leading to the luminescence at $\sim 555\,\mathrm{nm}$ observed in the CL measurement above. Moreover, the crystal lattices from two sides of the apex do not match each other when they join together above the apex of the GaN inverse pyramid resulting in double tips and a hole in between.

What is the optimal QW number of the conversion structure? A low QW number

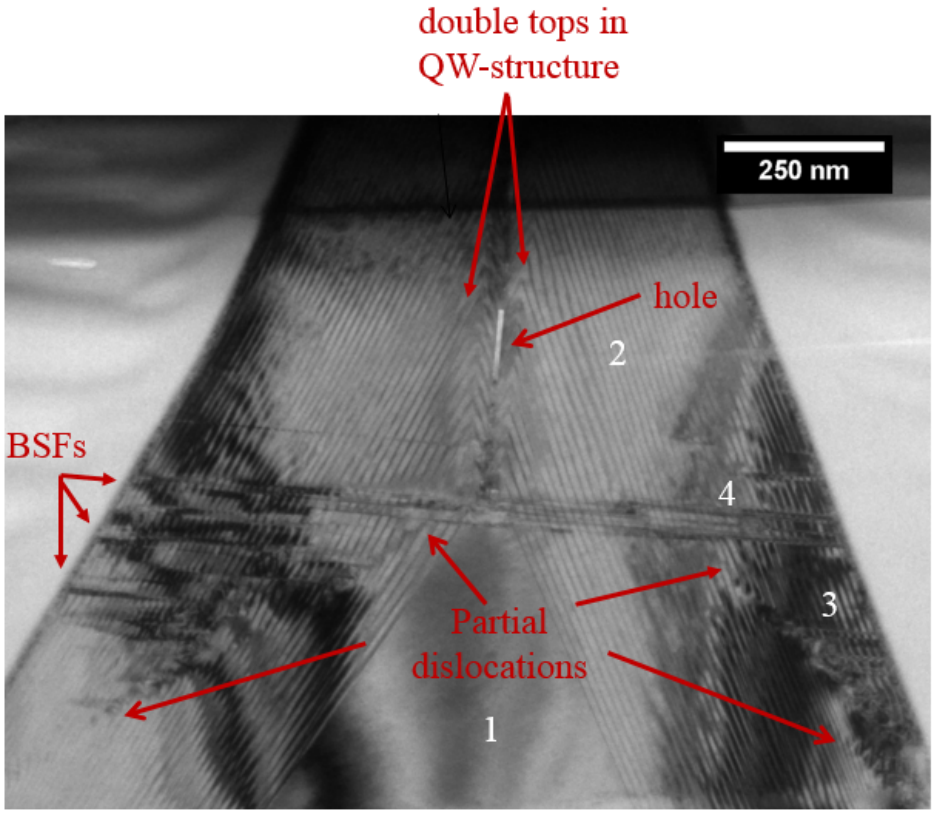

Figure 5.20.: The TEM image of the region close to the ridge for the conversion structure with 40-fold InGaN/GaN QWs.

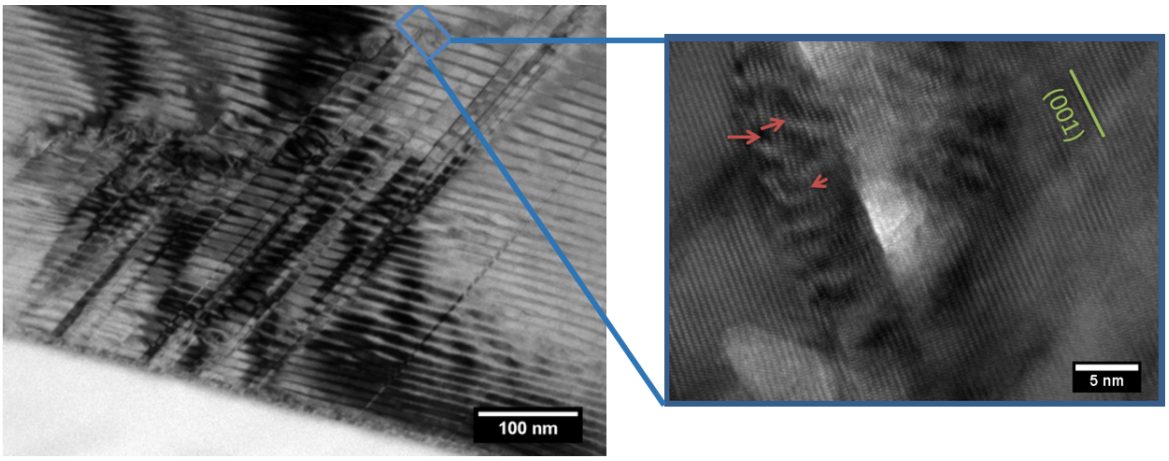

Figure 5.21.: TEM images showing the BSFs lying on the c-plane generated within the QWs. The partial dislocations terminate the the conversion structure with 40-fold InGaN/GaN QWs.

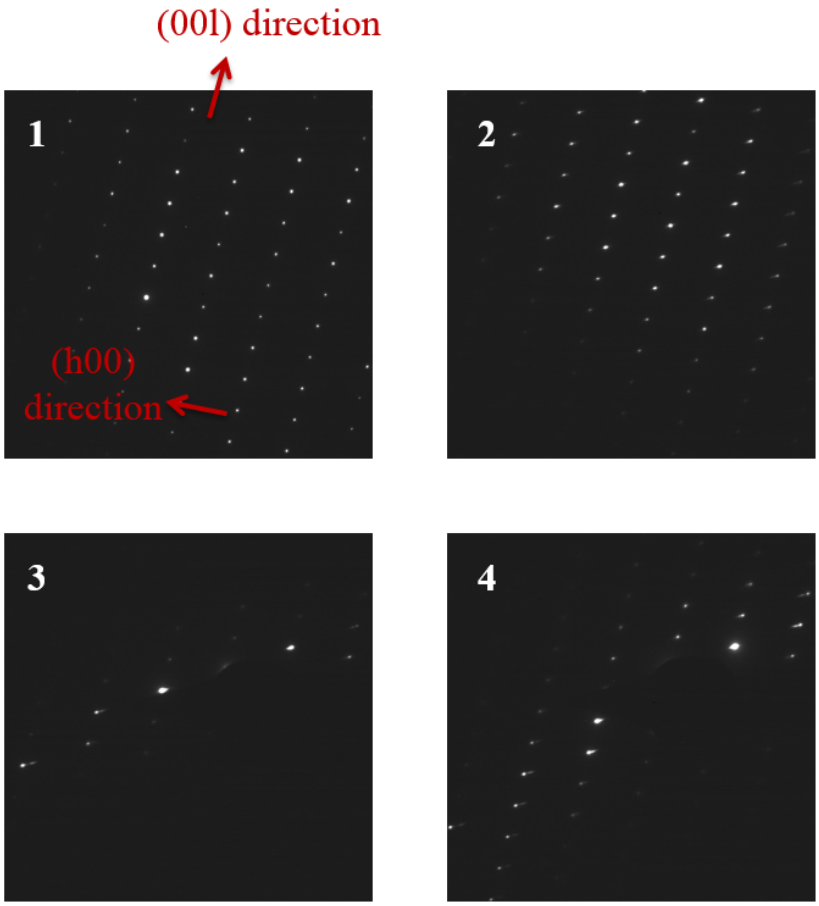

Figure 5.22.: Diffraction patterns at 4 locations with a constant sample orientation for the conversion structure with 40-fold InGaN/GaN QWs. Locations # 1–4 are marked in Fig. 5.20.

results in low absorption and high conversion due to better crystal quality and vice versa for a high QW number. Hence, an optimum has to be found concerning the number of QWs aiming at higher green light intensity. To this end, we have grown three samples (sample # 1, # 2 and # 3) with 10, 15 and 20 QWs, respectively, all emitting at the same wavelength of 505 nm (Fig. 5.23). Indeed, the absorption fraction η_a rises with increasing QW number as expected, exceeding 90 % for the samples with 15 and 20 QWs. For optically pumped structures, electron and hole densities are the same within each QW, but decrease exponentially with respect to the penetration depth of the blue pump light. Thus, the overall performance will depend more strongly on the quality of the QWs closer to the excitation source. Sample # 1 and # 2, with 10 and 15 QWs respectively, have similar values for η_c, 4.9 % and 5.1 %, indicating comparable QW quality and the higher number of QWs results in a higher total green emission. However, for sample # 3 the further addition of 5 QWs leads to a reduction of η_c by 0.9 % compared to sample # 2 indicating an inferior crystalline quality for the higher number of QWs which counters and outweighs the higher absorption of blue light. One reason is the larger thermal load experienced by early grown QWs during the longer overgrowth. On the other hand, late grown QWs encounter an increasing number of defects caused by the strain in the underlying GaN/InGaN superlattice of QWs. With our current epitaxy conditions, sample # 2 has the strongest green emission achieving a balance between those two parameters η_a and η_c.

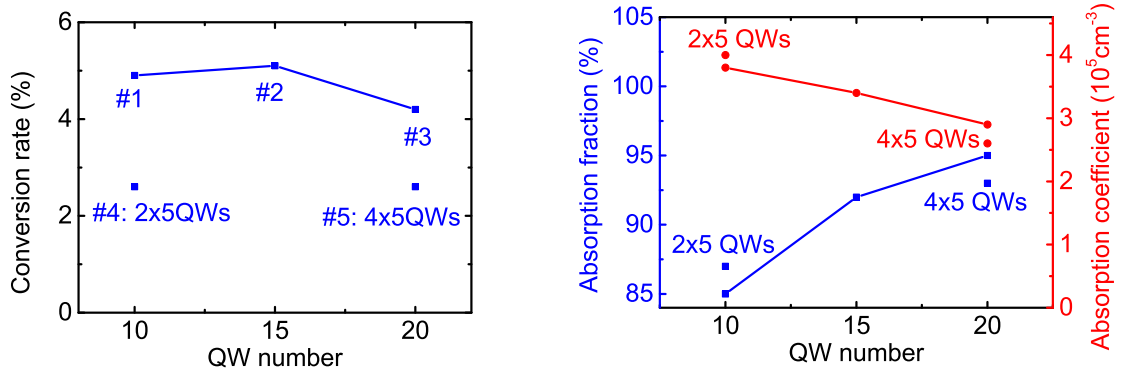

Figure 5.23.: Result of the transmission experiment for green converters of different QW numbers under forward excitation. ($\lambda = 505$ nm)

In order to reduce strain related defects and consequently improve the quality of the late grown QWs, groups of 5 QWs each were separated by inserting about 50 nm GaN, thus reducing the average In content of the active layer. Two samples with 2×5 QWs and 4×5 QWs (sample # 4 and # 5) were produced. While the samples with the same number of QWs (sample # 1 and # 4; sample #3 and #5) have similar values of η_a, the samples with separated groups of QWs have substantially decreased values for η_c. This is attributed to the extra thermal load caused by the growth of the GaN layer between each two groups of 5 QWs which seems to be more important than the reduced strain.

All 5 samples (sample # 1-5) have similar values for the absorption coefficient α which confirms comparable absorption capability for the InGaN material with the same indium content.

As discussed above, the absorption in the QWs farther from the excitation source is much weaker than that in the ones close to it. Hence, the QWs with better quality should be placed closer to the excitation source to enhance the green emission intensity. When the green converter is placed with its epi-side facing the 405 nm laser, most of the pump light is absorbed in the topmost QWs and the measured light leaves the sample from the sapphire-side. We refer to such an experimental setup as backward excitation while the previously mentioned transmission experiment is named forward excitation. Comparing Fig. 5.23 and Fig. 5.24, η_a is pretty similar for the forward and backward excitation, respectively, for all 5 samples. Interestingly, η_c is enhanced by nearly 90 % in backward excitation for sample # 3. This result shows that the late grown QWs which are not subjected to a large thermal load have a better quality than the early grown ones and further optimizations for samples with high numbers of QWs should specifically address the issue of thermal budget.

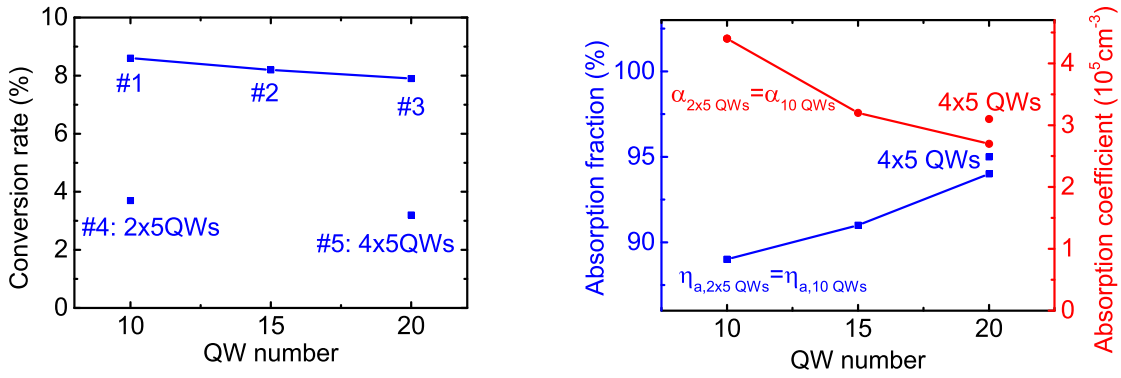

Figure 5.24.: Result of the transmission experiment for green converters of different QW numbers under backward excitation. ($\lambda = 505$ nm)

5.4.2. InGaN thickness

As mentioned, better crystal quality of the InGaN QW can be obtained by increasing the InGaN growth temperature leading to a lower indium concentration. The reduced indium concentration is compensated by other parameters, e.g., a larger InGaN well thickness. In a further experiment, we tried to find an optimum for the QW thickness.

The InGaN well thickness was set to be 2.5 nm, 3.5 nm, 5.0 nm and 7.5 nm by varying the InGaN growth time (Fig. 5.25). Wider QWs result in longer emission wavelength with a constant indium concentration because of a reduced quantum size effect. Thus, the growth temperature to achieve a constant QW emission wavelength of 510 nm can

be increased from 750 °C to 760°C with increasing InGaN well thickness. The η_a rises with increasing overall InGaN thickness as expected. The η_c, as figure of merit for the InGaN crystal quality, keeps the value of 10.8 % at the growth temperatures of 750 °C and 752 °C but is improved to 12.0 % at 758 °C. At 760 °C, η_c drops with the InGaN well of 7.5 nm. One reason for the reduced η_c may be the increasing QCSE with an increasing QW thickness. Moreover the total InGaN/GaN MQW thickness may exceed the critical thickness resulting in a reduced η_c. In this case, the total InGaN/GaN MQW thickness is 75 nm when half of the thickness is taken by the InGaN well. The indium concentration is $\sim$ 20 %. To the author's best knowledge, no investigations of the critical thickness of the InGaN/GaN MQW on $\{10\bar{1}1\}$ GaN have been reported yet [Hol06, SH12b].

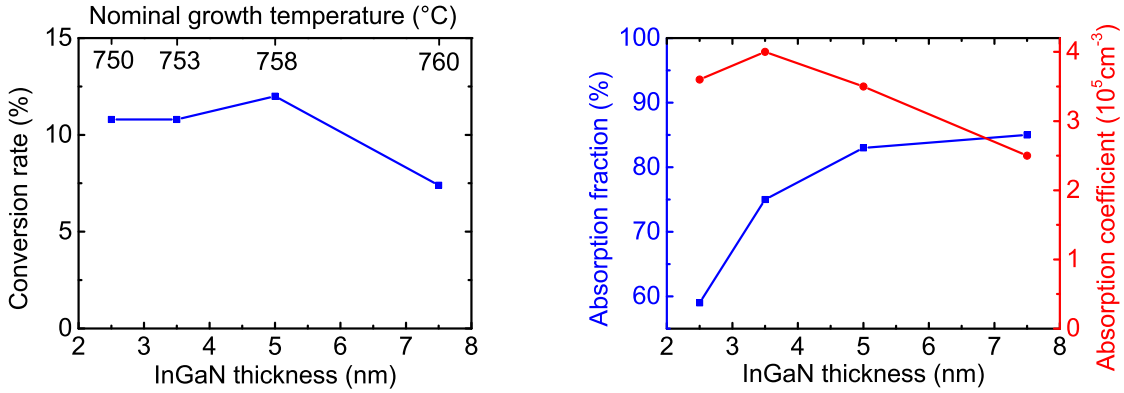

Figure 5.25.: Result of the transmission experiment for green converters varying the InGaN well thickness with backward excitation. (λ = 510 nm)

5.4.3. Reactor pressure

The reactor pressure was increased during the InGaN well growth in order to achieve a constant indium concentration at a higher growth temperature (Fig. 5.26). The reactor pressure should not exceed the pressure of any bubblers, in this case, the TMIn bubbler pressure of 40 kPa, to avoid the gas flow in the reverse direction from the reactor to the bubbler. As mentioned, the N_2 equilibrium pressure over the InN surface is several orders higher than that over the GaN and AlN surface and the binding energy of the chemical bonds in InN is weak. Therefore, high N_2 partial pressure is beneficial to incorporate more indium [Bhu03]. The N_2 partial pressure increases with the higher reactor pressure. Consequently, the required growth temperature to achieve a constant QW emission wavelength of 510 nm rises from 758 °C to 780°C with increasing reactor pressure. The η_a is measured to be fairly the same with equal overall InGaN thickness. The η_c however drops to almost half at the elevated InGaN growth temperature. It needs further investigation to clarify the effect of the high reactor pressure on the micro-structure of the InGaN material.

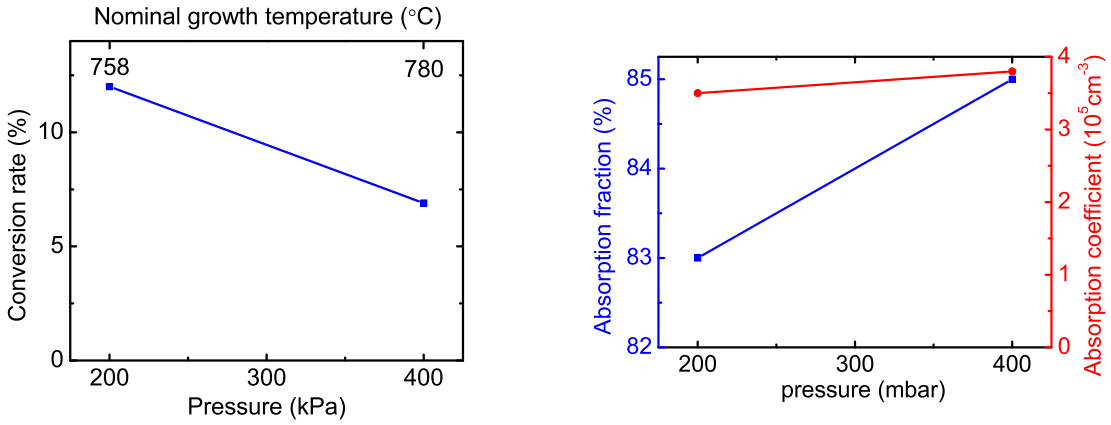

Figure 5.26.: Result of the transmission experiment for green converters varying the reactor pressure with backward excitation. ($\lambda = 510\,\mathrm{nm}$)

5.4.4. TMIn molar flow

The TMIn molar flow was increased during the InGaN well growth in order to achieve a constant indium concentration at a higher growth temperature. The source material TMIn is in the solid phase at the bubbler operation temperature of 17 °C leading to a relatively low sublimation rate. Therefore, the carrier gas N_2 will not be saturated by the TMIn vapor when its flow rate is above a certain limitation. Then, the molar flow of TMIn can not be calculated easily. In order to avoid this situation, we set the N_2 flow rate through the TMIn bubbler to be 200 sccm and increase the TMIn molar flow by tuning the bubbler pressure according to Equ. 3.1. The bubbler pressure of course should not be lower than the reactor pressure of 200 hPa to avoid any gas flow in the reverse direction, from the reactor to the bubbler. The TMIn bubbler pressure and the corresponding TMIn molar flow are listed in Table 5.1. Obviously, larger molar flow ratio between TMIn and TEGa should enhance the indium incorporation. Thus, the required growth temperature to achieve a constant QW emission wavelength of 518 nm increases from 752 °C to 787 °C with increasing TMIn molar flow (Fig. 5.27). The sample grown with the TMIn molar flow of 40 µmole/min is characterized via the transmission experiment twice resulting in two sets of data (the second set presented by the star symbol in Fig. 5.27) indicating a resonable error bar. The η_a remains fairly the same with an equal InGaN thickness as expected. The η_c rises up with increasing InGaN growth temperature and reaches a maximum of 10.3 % at a growth temperature of 779 °C. An excessive increase in the TMIn molar flow up to 53 µmole/min presumably enhances indium surface segregation and as a result, the MQW quality and interface abruptness are degraded [Kim07].

Table 5.1.: The applied TMIn bubbler pressure and the corresponding TMIn molar flow. The star symbols present the result according to a repeated transmission experiment from the same sample.

TMIn bubbler pressure(mbar)	f_{TMIn} (µmole/min)
400	26
320	33
266	40
200	53

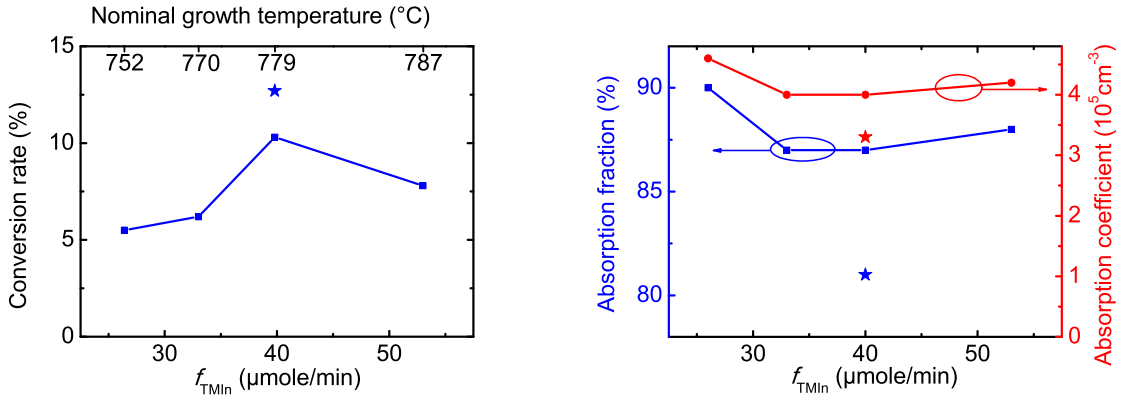

Figure 5.27.: Result of the transmission experiment for green converters varying the TMIn molar flow with backward excitation. ($\lambda = 518\,\mathrm{nm}$)

5.4.5. TEGa molar flow

Another way to optimize the In incorporation may be a variation of the TEGa flow. However, two opposite effects must be considered: For a reduced TEGa flow, we obtain a larger molar flow ratio between TMIn/TEGa and smaller growth rate (Fig. 5.28). The former may lead obviously to more indium incorporation whereas the latter the opposite since the indium adatoms have more chance to evaporate back into the gas phase [Cho01]. When the TEGa molar flow was decreased from 14 µmole/min to 8 µmole/min, the second effect seems to dominate leading to a reduced indium incorporation efficiency. Therefore, the growth temperature must be decreased from 791 °C to 785 °C to achieve a constant emission wavelength. We observed that η_c was improved at lower growth temperature, presumably a consequence of a lower growth rate. When the TEGa molar flow was decreased further down to 1 µmole/min, the first effect dominated leading to the possibility to enhance the growth temperature for a constant QW emission wavelength of 500 nm. However, opposite to our first expectation, η_c drops presumably because the defects are generated via the evaporation of indium adatoms back into the gas phase. η_a and η_c have the opposite trend among these four samples: the larger the η_a, the smaller the η_c. The sample grown with

the TEGa molar flow of 8 µmole/min has the optimal η_c of 46.2 % which is actually surprisingly high. Its much reduced η_a of 35 % is presumably due to the absence of the absorption at defects.

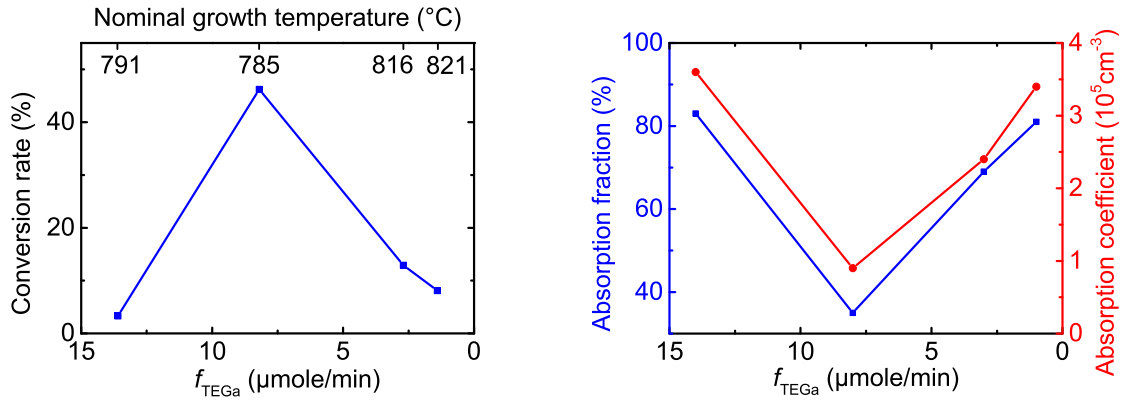

Figure 5.28.: Result of the transmission experiment for green converters varying the TEGa molar flow with backward excitation. ($\lambda = 500$ nm)

5.5. Stripe LEDs with optimized InGaN growth condition

We integrated some of the optimized growth parameters into the stripe $\{10\bar{1}1\}$ LED with a single QW. For the reference LED, flows of $f_{\mathrm{TMIn}} = 26$ µmole/min and $f_{\mathrm{TEGa}} = 14$ µmole/min were used. For the improved one, $f_{\mathrm{TMIn}} = 40$ µmole/min and $f_{\mathrm{TEGa}} = 3$ µmole/min. The optimal f_{TEGa} of 8 µmole/min was not applied due to time issue. The InGaN well thickness was kept to be 2.5 nm to avoid any p-GaN quality degradation caused by the thicker InGaN layers underneath. The growth temperature of the InGaN well was chosen to be 807 ° C leading to an emission wavelength of 430 nm in EL. The EL output power was enhanced by a factor of more than 3 under the optimized InGaN growth condition while the I-V curve keeps a similar shape (Fig. 5.29).

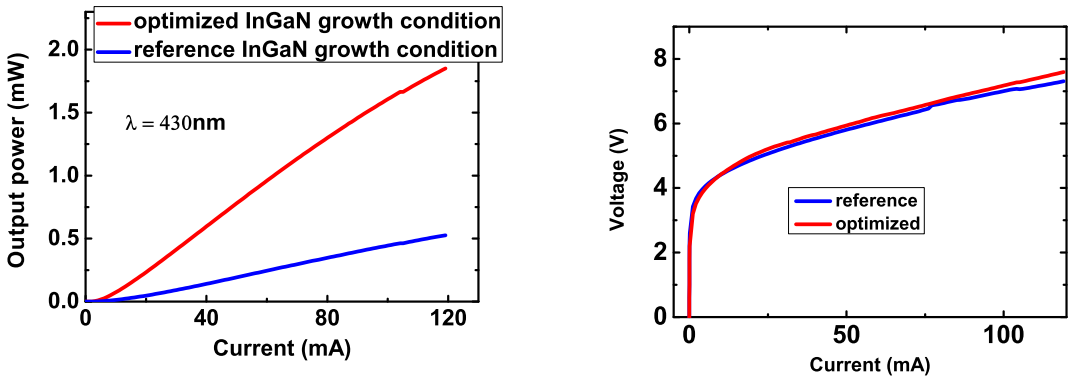

Figure 5.29.: EL output power against current (left) and I–V curve (right) of stripe LEDs with the reference and optimized InGaN growth conditions.

6. LED Evaluation

Two LED evaluation methods, the ABC model fitting and the electron beam-induced current method, will be discussed in this chapter. By the fit of the EL data according to the well-known ABC model, one acquires more information beyond the EL output power, such as the internal quantum efficiency (IQE) and the carrier injection efficiency (CIE). The IQE can be determined by the fit of the curve of the PL intensity as a function of the excitation power at RT as well. Electron beam-induced current (EBIC) is a powerful LED analysis tool applied in the setup of SEM, capable to reveal the position and material quality of the buried *pn*-junction.

6.1. LED analysis with the ABC model

The investigation of semipolar/nonpolar LEDs has been strongly motivated by the potentially higher QW efficiency as compared to *c*-plane counterparts, especially in the emission wavelength range of the green light, due to the reduced piezoelectric field within the InGaN/GaN QWs (Fig. 2.10). However, the EL output power of the semipolar/nonpolar LEDs is still much less than that of the c-plane ones, at least for the structures on foreign substrates. Is the lower luminescence efficiency caused by lower QW efficiency or worse charge carrier transport into the QWs? In this section, we will try to answer this question by separating the IQE and the CIE through the ABC model fitting of the EL data for c-plane, $\{10\bar{1}1\}$ and $\{11\bar{2}2\}$ LEDs.

In order to judge the performance of such stripe LEDs described in the last section, we have compared them with a "standard" polar LED and also with another kind of semipolar LED. The schematic structures of the c-plane, $\{10\bar{1}1\}$ and $\{11\bar{2}2\}$ LEDs can be seen in Fig. 6.1. The c-plane LED was grown on a c-plane sapphire consisting of 3 µm thick *n*-GaN employing an in-situ deposited SiN nanomask layer for defect density reduction, 5-fold InGaN/GaN QWs as the active region with an InGaN thickness of 2.2 nm, 100 nm thick p-(Al)GaN capped with an excessively p-doped contact layer. The dislocation density of this GaN buffer layer is in the range of $3 - 5\times10^{8}\,\mathrm{cm}^{-2}$ [Her08]. The other semipolar LED, $\{11\bar{2}2\}$ LED, was grown and processed in our group by T. Meisch by employing a $\{10\bar{1}2\}$ sapphire wafer as substrate [Sch14, Oka09, Oka12]. Firstly, the photoresist on the sapphire substrate is patterned into parallel stripes running along the sapphire *a*-direction with a period

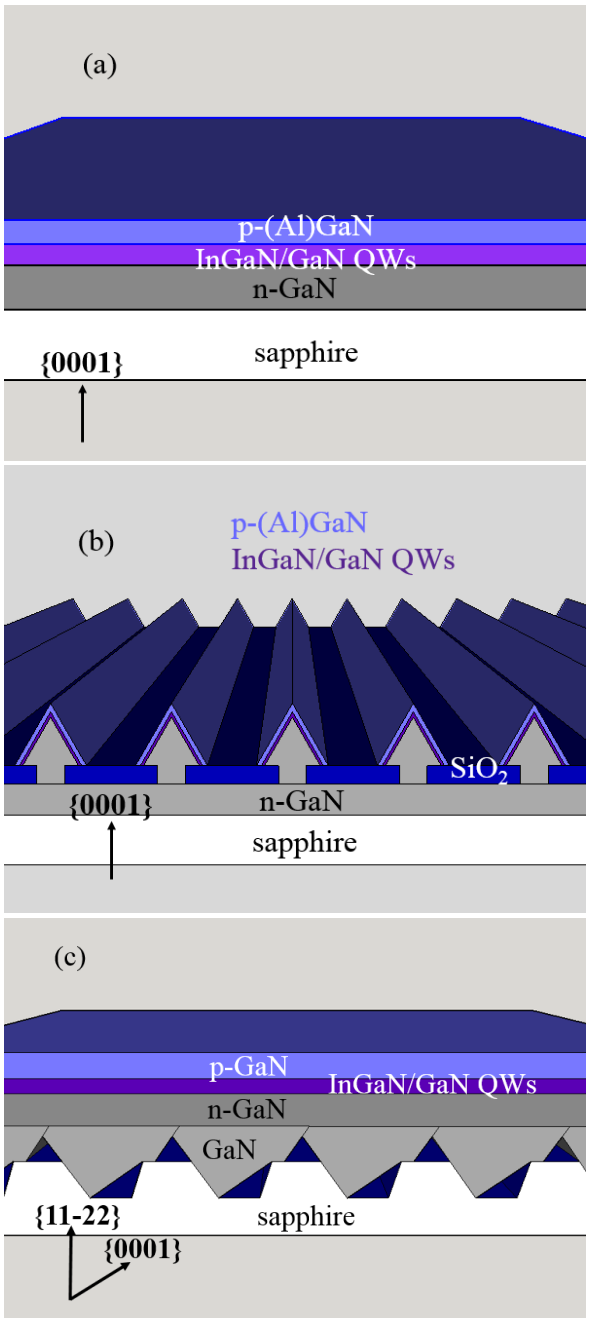

Figure 6.1.: Schematic structure of the c-plane (a), stripe $\{10\bar{1}1\}$ (b) and planar $\{11\bar{2}2\}$ (c) LEDs. First published in [Wan16].

of 6 µm via lithography. The stripe pattern is transferred into the sapphire substrate via reactive ion etching to achieve trenches with *c*-plane-like sidewalls. Then, SiO_2 is sputtered on top of all non *c*-plane-like facets to avoid parasitic GaN growth. Finally, the GaN growth starts from the *c*-plane-like sidewall and coalesces into a planar $\{11\bar{2}2\}$ surface, followed by *n*-GaN, 5-fold InGaN/GaN QWs with the InGaN thickness of 4.1 nm and *p*-GaN layers to complete the LED structure. The *c*-plane LED, the stripe $\{10\bar{1}1\}$ LED and the planar $\{11\bar{2}2\}$ LED emit at 435 nm, 430 nm and 428 nm, respectively, in order to compare the IQE and the CIE of the polar and semipolar LEDs at similar wavelength. The corresponding indium content differs due to the different piezoelectric polarities on variable crystal facets and the different InGaN well thicknesses among these three samples.

6.1.1. Efficiency

Wall plug efficiency

The overall efficiency of the LED is the ratio of the radiant flux (radiant energy per unit time, also called radiant power) and the consumed electrical power, named *wall plug efficiency* (WPE). Thus, WPE can be calculated as

$$\mathrm{WPE} = \frac{\Phi}{IV} \tag{6.1}$$

where Φ represents the radiant flux out of the LED, I the current through the LED and V the voltage over the LED.

External quantum efficiency

In any efficient LEDs, most of the electrons and holes are transported from the opposite directions into the active region by the flowing current and recombine there. However not all free electron-hole pairs entering the LED device contribute to photons exiting the LED. The ratio of the photons exiting the LED and the electron-hole pairs entering the LED is named *external quantum efficiency* (EQE). The EQE as an input data for the EL fit besides the current density j can be calculated from the experimental result according to the following equation:

$$\mathrm{EQE} = \frac{\Phi/E_{\mathrm{ph}}}{I/q} \quad \text{where} \quad E_{\mathrm{ph}} = \frac{hc}{\lambda} \tag{6.2}$$

with E_{ph} representing the photon energy, q the elementary charge, h Planck's constant, c the speed of light in vacuum and λ the emission wavelength. The radiant flux Φ is measured in an integration sphere whereas the emission wavelength λ is obtained by a spectrometer.

The EQE can be expressed as the product of three items, *carrier injection efficiency* (CIE), *internal quantum efficiency* (IQE) and *light extraction efficiency* (LEE):

$$\mathrm{EQE} = \mathrm{CIE} \cdot \mathrm{LEE} \cdot \mathrm{IQE}. \tag{6.3}$$

The CIE is the fraction of the free charge carriers injected into the active region outside the ones entering the LED. Some electrons and holes recombine via defect-related traps in the bulk material out of the active region nonradiatively thus reducing the CIE.

The LEE is the fraction of the photons extracted out of the LED to all the generated photons. When a photon emitted in the active region hits the LED surface with an angle larger than the total reflection angle, it will be reflected back into the LED. This photon may be absorbed during the travel or be extracted by the next chance hitting the device surface. To enhance the LEE, the LED surface is normally roughened [Fuj04] to vary the incident angle at different positions on the device surface and immersed into transparent domes made of high-refractive-index materials, e.g., silicone with the refractive index of 1.54, so that the total reflection angle is increased.

The energy difference between the initial and the final state of the electron-hole recombination is given off via different mechanisms which are classified into either radiative or nonradiative recombination mechanisms depending on whether the extra energy is transferred to emitted photons or not. The fraction of the radiative recombination events is defined as the IQE.

Obviously, the three components of the EQE are related to different aspects of the LEDs: The CIE describes the carrier transport into the QWs heavily affected by the diode quality; the LEE is related to the refractive index of the materials, the surface morphology of the device, the device shape and so on; the IQE is mainly determined by the crystal quality of the active region. It is very helpful to acquire all of the three components individually to reveal the promising aspect to improve the EQE further. The CIE and the LEE are assumed to be independent on the carrier density n while the IQE depends on n according to the ABC model fitting which is discussed in the next section.

Internal quantum efficiency

The internal quantum efficiency is defined as

$$\mathrm{IQE} = \frac{R_{\mathrm{rad}}}{R} \tag{6.4}$$

where R_{rad} represents the radiative recombination rate and R the total recombination rate.

According to the ABC model [Sho52, Dai09], there are three recombination mechanisms:

- Schockley-Read-Hall (SRH) recombination is a single-particle process assisted by defects. Impurities or crystal defects give rise to defect levels in the forbidden band. Electrons or holes interact with defect levels releasing energy by a few steps emitting phonons and finally recombine with other holes or electrons. The SRH recombination rate R_{SRH} can be calculated as

$$R_{\mathrm{SRH}} = A_n \left(n - n_{\mathrm{i}}\right) \quad \text{or} \quad R_{\mathrm{SRH}} = A_p \left(p - p_{\mathrm{i}}\right) \tag{6.5}$$

  in case that an electron or hole interacts with the defect level, respectively. A_n and A_p are the RRCs of the SRH recombination for electrons and holes, respectively, n the electron concentration, p the hole concentration and n_{i} or p_{i} the equilibrium electron or hole concentration. When $n = p \gg n_{\mathrm{i}}$ under strong excitation, Equ. 6.5 can be then rewritten as $R_{\mathrm{SHR}} = An$.

- During the radiative recombination, an electron interacts with a hole releasing the extra energy as a photon. Two particles, an electron and a hole, are involved in the process and the total recombination rate should be proportional to the product of the exceeding electron concentration $n - n_{\mathrm{i}}$ and hole concentration $p - p_{\mathrm{i}}$:

$$R_{\mathrm{rad}} = B \left(p - p_{\mathrm{i}}\right) \left(n - n_{\mathrm{i}}\right) \tag{6.6}$$

  with B representing the radiative recombination coefficient (RRC). Under strong excitation, $n = p \gg n_{\mathrm{i}}$ and Equ. 6.6 can be rewritten as $R_{\mathrm{rad}} = Bn^2$. We notice that R_{SRH} is proportional to n whereas R_{rad} varies with n^2. Therefore, the SRH recombination dominates at low current density ($n \ll \frac{A}{B}$) and the radiative recombination dominates at high current density ($n \gg \frac{A}{B}$).

- An Auger recombination process involves three particles. An electron in the conduction band falls directly into the valence band and recombines with a hole there. The extra energy is transferred to a third particle which is excited to a higher energy level, rather than emitting a photon. Hence, the Auger recombination rate R_{Auger} can be expressed as

$$R_{\mathrm{Auger}} = \left(C_n \cdot n + C_p \cdot p\right) \left(np - n_{\mathrm{i}}^2\right) \tag{6.7}$$

  with C_n or C_p being the Auger coefficients for electrons or holes, respectively. With the simplification done above, $R_{\mathrm{Auger}} = Cn^3$ under strong excitation with $C = C_n + C_p$ as the RRC for the Auger recombination. R_{SRH}, R_{rad} and R_{Auger} are proportional to n, n^2 and n^3, respectively. Hence, the Auger recombination overwhelms the other two mechanisms at pretty high current density ($n \gg \frac{B}{C}$). It is discussed as the most important reason for the droop effect by the scientific community. The use of a luminescence conversion structure is motived by the fact that it may have a reduced droop effect as compared to LEDs, as discussed

in Chapter 5. Commercial high-power LEDs actually operate at a high current density in order to decrease the device costs. However, then the Auger effect becomes significant when the Auger effect dominates to achieve high output power.

In conclusion, IQE can be calculated as the ratio between the radiative recombination rate and the total recombination rate:

$$\mathrm{IQE} = \frac{Bn^2}{An + Bn^2 + Cn^3} \tag{6.8}$$

which is the fundamental equation for the ABC model fitting.

Several assumptions are made for the ABC model:

- The excess electron and hole concentrations are assumed to be the same, i.e., $n = p$. This is true in the case of a single QW, but not necessarily for multi-QWs. For the latter, the electrons and holes may be distributed differently over multi-QWs of LED whereas the total amounts of the electrons and holes are equal due to electric charge conservation. Most holes accumulate in the QW close to the p-side of the LED with a small amount transported to the other QWs due to the lower mobility of the holes. Conversely, the electrons are distributed more homogeneously over the multi-QWs. Therefore, $n \neq p$ in each individual QW of the multi-QW LED.

- The electron and hole concentrations are assumed to be much larger than the equilibrium carrier concentration. This is valid under strong excitation, but may cause deviations at small operation current of the LED.

- The RRCs A, B and C are assumed to be independent on the carrier concentration n. This may deviate from the fact that RRCs may not be constant at different operation currents of the LED.

These assumptions flow into the inaccuracy of the fitting method according to the ABC model which should always be taken into consideration.

Electrical efficiency

The WPE, as the overall efficiency of the LEDs, can be split into two components, the EQE and *electrical efficiency* (EE). Referring to Equ. 6.1 and Equ. 6.2, the EE is calculated as the ratio between the WPE and the EQE:

$$\mathrm{EE} = \frac{E_{\mathrm{ph}}}{qV}. \tag{6.9}$$

The resistance connected in series with the diode in the LEDs may consume energy reducing the EE. The p-contact resistance as an important series resistance has been

optimized to enhance the EE in our work (section 4.4). However, the EE has not been specifically analysed in this work.

6.1.2. Principle of ABC model fitting

The equations for the fit of the EL and PL data will be derived in this section one by one.

By inserting Equ. 6.8 into Equ. 6.3, the relation between EQE and the carrier concentration n can be written as

$$\mathrm{EQE} = \mathrm{CIE} \cdot \mathrm{LEE} \cdot \frac{Bn^2}{An + Bn^2 + Cn^3} \tag{6.10}$$

In the case of EL, the recombination rate R is equal to the carrier injection rate G_{inj} in steady state, $R = G_{\mathrm{inj}}$.

$$R = An + Bn^2 + Cn^3, \tag{6.11}$$

$$G_{\mathrm{inj}} = \frac{\mathrm{CIE} \cdot I}{qV_{\mathrm{QW}}} \tag{6.12}$$

where I, q and V_{QW} are the operation current, the elementary charge and the QW volume, respectively. Therefore, the relation between the current density j and the carrier concentration n can be written as

$$j \cdot \mathrm{CIE} = qd_{\mathrm{QW}} \left(An + Bn^2 + Cn^3 \right) \tag{6.13}$$

with d_{QW} representing the QW thickness.

Multiplying Equ. 6.10 with Equ. 6.13, the carrier concentration n can be expressed by other parameters as:

$$n = \sqrt{\frac{\mathrm{EQE} \cdot j}{Bqd_{\mathrm{QW}}\mathrm{LEE}}} \tag{6.14}$$

Inserting Equ. 6.14 into Equ. 6.13, we obtain a relation between j and $\sqrt{j \cdot \mathrm{EQE}}$:

$$j = \frac{A}{\mathrm{CIE}}\sqrt{\frac{qd_{\mathrm{QW}}}{B \cdot \mathrm{LEE}}}\sqrt{j \cdot \mathrm{EQE}} + \frac{1}{\mathrm{CIE} \cdot \mathrm{LEE}}\left(\sqrt{j \cdot \mathrm{EQE}}\right)^2 + \frac{C}{\mathrm{CIE}}\sqrt{\frac{1}{qd_{\mathrm{QW}}B^3\mathrm{LEE}^3}}\left(\sqrt{j \cdot \mathrm{EQE}}\right)^3. \tag{6.15}$$

j is a cubic polynomial function of $\sqrt{j \cdot \mathrm{EQE}}$ with the constant term being zero. By applying a polynomial fit to the curve of j versus $\sqrt{j \cdot \mathrm{EQE}}$, one obtains the coefficients of all terms in Equ. 6.15. CIE $\cdot$ LEE is determined from the coefficient of the quadratic term and the IQE is calculated as the ratio between the EQE and

CIE · LEE. The latter two parameters can not be obtained separately from these equations. A good estimation of LEE for a certain structure can be achieved by Monte Carlo ray tracing. It is reported to be about 23 % for on-wafer measurements of a c-plane LED [Lee07]. An enhanced LEE is expected for the two semipolar LEDs due to the 3D GaN surface morphology or the sapphire structurization. As a rough estimate, we have assumed 40 % of LEE for both structures. Therefore, the CIE is acquired as the ratio between CIE · LEE and the assumed LEE. Two equations are acquired from the coefficients of the linear and cubic terms with three variables, the RRCs A, B and C. Therefore, not only the EL fit but also a measurement of, for example, the differential carrier lifetime are necessary in order to determine all three RRCs independently [Dav10]. However, time-dependent experiments were beyond the experimental possibilities of this thesis.

In order to check our EL evaluation, we applied a similar fitting procedure to PL data. The fitting principle of the PL data is explained as follows. The ratio of the integrated PL intensity I_{PL} and the power of the excitation source P_{PL} is proportional to the IQE:

$$\frac{I_{\mathrm{PL}}}{P_{\mathrm{PL}}} = \eta_1 \frac{Bn^2}{An + Bn^2 + Cn^3} \tag{6.16}$$

with η_1 denoting an unknown constant. The carrier generation rate G is proportional to the power of the excitation source:

$$G = \eta_2 P_{\mathrm{PL}} \tag{6.17}$$

with η_2 denoting another unknown constant. In steady state, the carrier generation rate is equal to the recombination rate, $G = R$. Considering Equ. 6.11, we get

$$\eta_2 P_{\mathrm{PL}} = An + Bn^2 + Cn^3. \tag{6.18}$$

Multiplying Equ. 6.16 with Equ. 6.18, the carrier concentration n can be expressed by other parameters as:

$$n = \sqrt{\frac{\eta_2 I_{\mathrm{PL}}}{\eta_1 B}} \tag{6.19}$$

By inserting Equ. 6.19 into Equ. 6.18, one can derive a relation between the parameters I_{PL} and P_{PL} as:

$$P_{\mathrm{PL}} = A\sqrt{\frac{1}{B\eta_1\eta_2}}\sqrt{I_{\mathrm{PL}}} + \frac{1}{\eta_1}\left(\sqrt{I_{\mathrm{PL}}}\right)^2 + C\sqrt{\frac{\eta_2}{B^3{\eta_1}^3}}\left(\sqrt{I_{\mathrm{PL}}}\right)^3 \tag{6.20}$$

Similar as Equ. 6.15, P_{PL} is a cubic polynomial function of $\sqrt{I_{\mathrm{PL}}}$ with the constant term being zero. Both, P_{PL} and I_{PL} can be obtained from the PL experiment. By applying again a polynomial fit to the curve of P_{PL} versus $\sqrt{I_{\mathrm{PL}}}$, one obtains the value of $\frac{1}{\eta_1}$ as the coefficient of the quadratic term with which the absolute value of IQE can be calculated according to Equ. 6.16.

Logarithmic asymptotes

The rates of the SRH recombination, the band-to-band recombination and the Auger recombination are proportional to n, n^2 and n^3, respectively. Therefore, the SRH recombination dominates at low n, detrimental for the emission efficiency. An optimal emission efficiency occurs when the band-to-band recombination catches up with the carrier concentration increased to a proper range. The superlattice structure of the QWs helps confine the carriers increasing the local carrier concentration in order to prevent the poor emission efficiency at low n. However, the emission efficiency drops again when the Auger recombination dominates at high n.

For low n,

$$\mathrm{IQE}_{\mathrm{low}\,n} = \frac{Bn}{A} = \frac{B \cdot \mathrm{CIE} \cdot j}{A^2 q d_{\mathrm{QW}}}. \tag{6.21}$$

For high n,

$$\mathrm{IQE}_{\mathrm{high}\,n} = \frac{B}{Cn} = \frac{B q^{1/3} d_{\mathrm{QW}}^{1/3} j^{-1/3}}{C^{2/3} \mathrm{CIE}^{1/3}}. \tag{6.22}$$

The slopes at low and high carrier concentrations in the double logarithmic-scaled diagram of the IQE versus the current density j should be 1 and $-\frac{1}{3}$, respectively, according to Equ. 6.21 and Equ. 6.22. These slope values will be determined from the experimental EL data in the next section to check any deviations from the ABC model.

6.1.3. Results and discussions

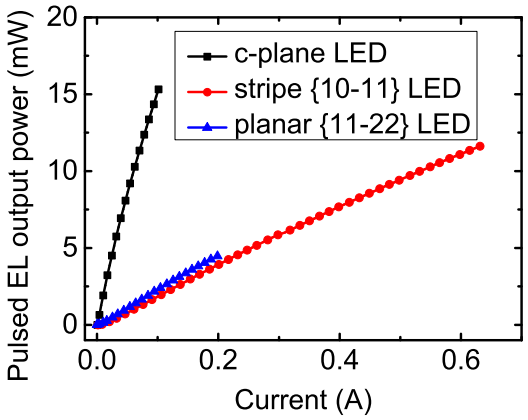

Figure 6.2.: Output power against current of the pulsed EL for c-plane, stripe $\{10\bar{1}1\}$ and planar $\{11\bar{2}2\}$ LED. First published in [Wan16].

The electroluminescence was measured in pulsed mode to avoid diode heating at large current densities. The chosen pulse width was 1 µsec with a duty cycle of 1 %. The c-plane LED, the stripe $\{10\bar{1}1\}$ LED which we studied here in detail and the planar $\{11\bar{2}2\}$ LED emit at 435 nm, 430 nm and 428 nm, respectively. As seen in Fig. 6.2, the c-plane LED has much higher output power in pulsed EL than the two semipolar ones. We have applied the fitting method to all three structures to analyse whether the lower luminescence efficiency of the semipolar LEDs on foreign substrates is caused by lower CIE or lower IQE.

For the simple c-plane LED, two sister wafers with almost the same emission wavelength (Fig. 6.3) were taken, one characterized right in our group and the other by T. Meyer in the characterization labs of Osram OS (Regensburg). A tight fit was obtained for the EQE curve of the former. CIE · LEE is determined to be 0.18 as the reverse value of the coefficient of the quadratic term in Equ. 6.15. Thus, the CIE is calculated to be 78 % with the assumed LEE of 23 % according to the simulation of Monte Carlo ray tracing (Table 6.1). The IQE is acquired as the ratio between the EQE and CIE · LEE. Similar IQE data versus current density have been measured from the sister wafer by T. Meyer [Mey14] nicely confirming our evaluation method (Fig. 6.4). From these results, we estimate a maximum error range of our IQE value of about 30 %.

Tight fits were obtained for the EQE curves of the two semipolar structures as well (Fig. 6.5, left). CIE · LEE is determined to be 1.7 % for both, the stripe $\{10\bar{1}1\}$ LED and the planar $\{11\bar{2}2\}$ LED. The corresponding CIE values are 4 % calculated with the assumed LEE values of 40 % for these two structures (Table 6.1). Surprisingly, the CIE of the semipolar LEDs is much lower than 78 % of the c-plane LEDs! As seen in Fig. 6.5, both, the EQE and the IQE raise fast and start to decrease at a smaller current density for the c-plane LED as compared to the semipolar ones. The IQE of the semipolar LEDs is lower than that of the c-plane LED at low current density but is similar and even higher at high current density. This can not explain the much higher EQE of the c-plane LED at all current densities. Obviously, the poor carrier injection is responsible for the not satisfying performance of the semipolar LEDs rather than the spectra and hence the crystal quality of the InGaN/GaN QWs.

The slope of the double logarithmically plotted IQE against the current density j falls mainly into the predicted range, from 1 until $-\frac{1}{3}$, for all three samples (Fig. 6.6). The only exception is the derivative value above 1 at low current densities for the stripe $\{10\bar{1}1\}$ LED. This may be due to the deviation of the LED behaviour from the ABC model or the relatively large measurement error of the electroluminescence output power at low current densities.

As mentioned, it is impossible to determine all three RRCs, A, B and C independently only from EL. $3.6\times10^{-12}\,\mathrm{cm^3s^{-1}}$ is a typical B value for c-plane LEDs emitting at ∼430 nm (Table 6.1). In fact, a larger B is expected for semipolar structures at least due to the smaller piezoelectric fields within the QWs. However, the B

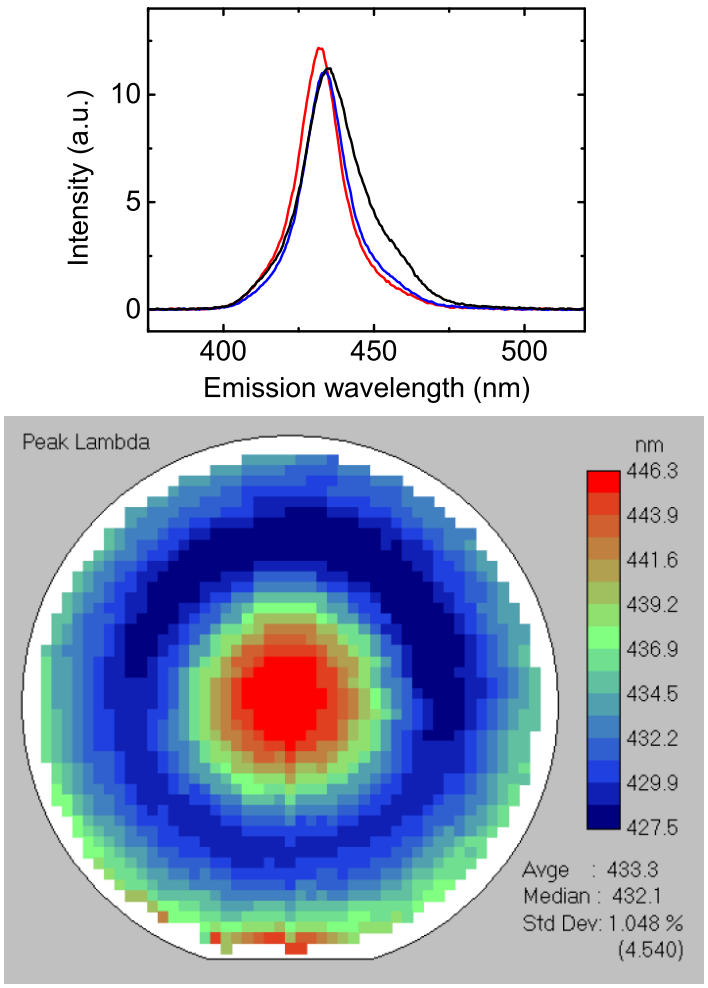

Figure 6.3.: Two c-plane sister wafers were grown in our group. One is processed and characterized in our group and the other by T. Meyer in OSRAM OS, Regensburg. Three EL spectra of the former (upper) measured at different contacts located 1–1.5 cm away from the wafer center. The emission wavelength of the EL emission mapping over the whole wafer from the latter (lower).

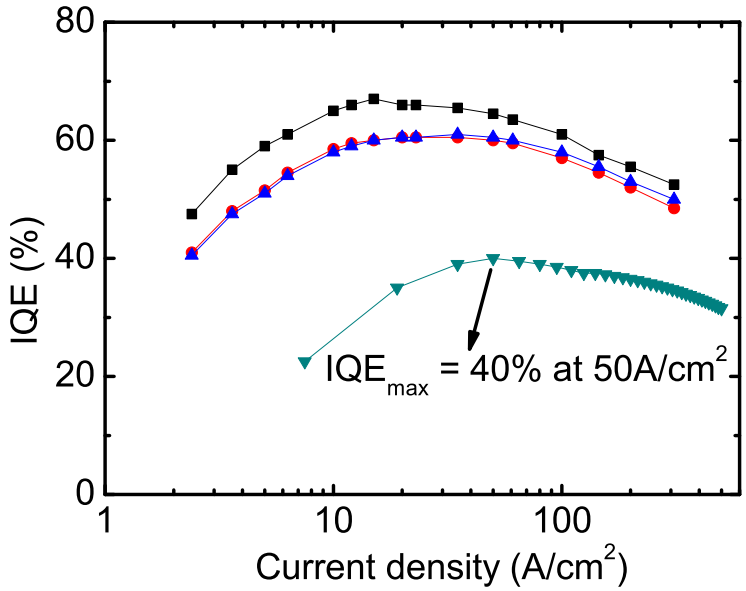

Figure 6.4.: The IQE curves of the two c-plane LEDs grown as sister wafers by our group, one characterized right in our group (the green curve) and the other in the labs of OSRAM OS (the black, red and blue curves). The upper three IQE curves belong to different measurement spots on the wafer: The black curve from the wafer center, the red and blue curves from the wafer edge.

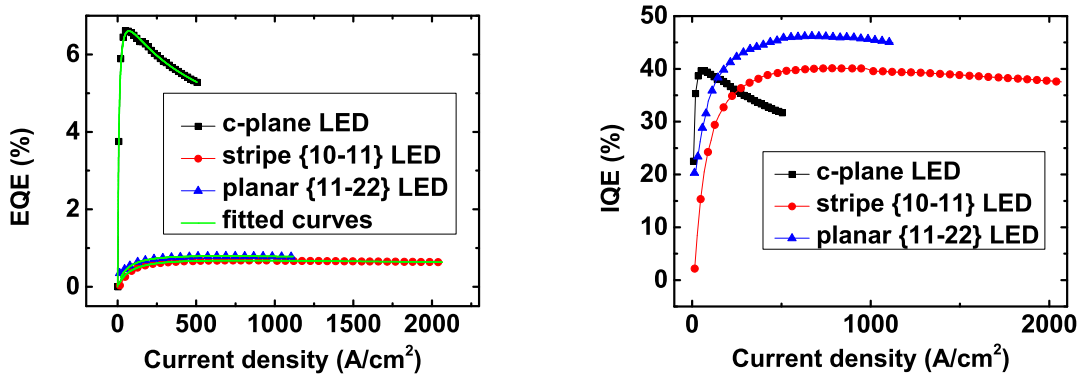

Figure 6.5.: The EQE (left) and the IQE (right) dependent on the current density for the c-plane LED, the stripe $\{10\bar{1}1\}$ LED and the planar $\{11\bar{2}2\}$ LED. First published in [Wan16].

Table 6.1.: The values of the LEE, CIE and all three RRCs, A, B and C, for the c-plane LED grown and investigated according to the ABC model by OSRAM OS (Regensburg) [Sch13] and all samples investigated according to the ABC model in this work. They are our c-plane, stripe $\{10\bar{1}1\}$, planar $\{11\bar{2}2\}$ LEDs with the reference p-GaN and the improved p-GaN and the $\{20\bar{2}\bar{1}\}$ and $\{10\bar{1}\bar{1}\}$ LEDs on the GaN native substrate. EL data of the last two samples is obtained from publications of Electrical and Computer Engineering Department in University of California [Zha11, Zha10a]. The LEE for the wafer-level measurement is estimated according to the Monte Carlo ray tracing whereas the LEE for the chip-level measurement is taken from [Sch13]. The A, B and C values for the c-plane LED of OSRAM OS are taken directly from [Sch13]. The B value is assumed to be the same for all other LEDs as the input to calculate the corresponding A and C.

	LEE	B ($\mathrm{cm^3 s^{-1}}$)	CIE	A ($\mathrm{s^{-1}}$)	C ($\mathrm{cm^6 s^{-1}}$)
c-plane LED of OSRAM OS	–	3.6×10^{-12}	–	1.3×10^{6}	1.3×10^{-31}
our c-plane LED	23 %	3.6×10^{-12}	78 %	1.8×10^{7}	5.4×10^{-31}
stripe $\{10\bar{1}1\}$ LED	40 %	3.6×10^{-12}	4 %	2.6×10^{7}	2.8×10^{-31}
reference planar $\{11\bar{2}2\}$ LED	40 %	3.6×10^{-12}	4 %	7.1×10^{6}	6.3×10^{-31}
improved planar $\{11\bar{2}2\}$ LED	40 %	3.6×10^{-12}	10 %	2.2×10^{6}	5.9×10^{-31}
$\{20\bar{2}\bar{1}\}$ LED on GaN	75 %	3.6×10^{-12}	90 %	2.6×10^{6}	1.1×10^{-31}
$\{10\bar{1}\bar{1}\}$ LED on GaN	75 %	3.6×10^{-12}	(178 %)	1.7×10^{7}	3.6×10^{-31}

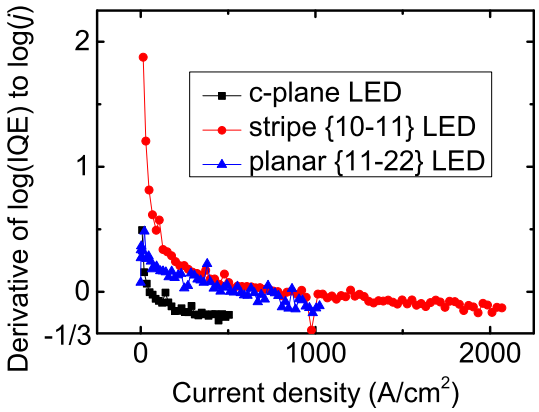

Figure 6.6.: Slope of the double logarithmic plot of the IQE against current density j for c-plane, stripe $\{10\bar{1}1\}$ and planar $\{11\bar{2}2\}$ LED.

value has not been reported for the semipolar structures to the best of the author's knowledge. Therefore, we made a worst case assumption taking the same B value of $3.6\times10^{-12}\,\mathrm{cm^3s^{-1}}$ for the stripe $\{10\bar{1}1\}$ and the planar $\{11\bar{2}2\}$ LED to check if reasonable values for A and C can be obtained. The c-plane LED contains 5 QWs, which means a total QW thickness of 2.2 nm $\times5$ = 11 nm whereas the stripe $\{10\bar{1}1\}$ and planar $\{11\bar{2}2\}$ LED have a total QW thickness of 2.5 nm and 20.5 nm, respectively. The calculated A and C values for all three samples are close to those of the c-plane LED from OSRAM OS, with the biggest differences as a factor of 20 and 5.7 for A and C, respectively.

For the PL measurements, we employed a 405 nm laser diode as excitation source to excite the carriers only in the QWs. The excitation power P_{PL} was varied from 1.4 mW to 104 mW by varying the driving current of the 405 nm laser diode. A stripe $\{10\bar{1}1\}$ structure with 5-fold InGaN/GaN QWs is employed in the PL measurement since the PL spectrum of single QW-structure is so weak that it is covered by the spectral tail of the 405 nm laser diode. The quantum efficiency keeps increasing with increasing excitation power since the 405 nm laser diode does not have sufficient power to reach the high carrier concentration where the Auger recombination is expected to dominate. Therefore, the cubic term in Equ. 6.20 is skipped for the fit of the PL data. Otherwise, the coefficients of the linear and the cubic terms are obtained as negative values without a physical meaning. Reasonable fits were obtained for the c-plane and the stripe $\{10\bar{1}1\}$ LED whereas the trend of the IQE curve dependent on the current density does not really follow the ABC model for the planar $\{11\bar{2}2\}$ LED which still needs more investigations (Fig. 6.7). The lack of the data points over a sufficiently large range of the carrier concentration would increase the error of the fitting. Nevertheless, the PL fit results in fairly the same IQE values for the c-plane and the stripe $\{10\bar{1}1\}$ LEDs and a relatively lower IQE value for the planar $\{11\bar{2}2\}$ LED (Fig. 6.7, right). The $\sim$35 % lower IQE of the planar $\{11\bar{2}2\}$ LED is definitely not the root reason for its inferior EL performance taking the big difference of the EL output power between the c-plane LED and the semipolar ones into account (see Fig. 6.2).

Another method to calculate the IQE is to take the ratio of the PL intensities at RT and low temperature assuming pure radiative recombinations at low temperature. Such PL measurements were performed with a 405 nm laser driving current of 50, 100, and 150 mA at RT and 13 K. The IQE evaluated by this method (Fig. 6.8) is much larger than the corresponding electroluminescence efficiency (cf. Fig. 6.5, left) which may be taken as a confirmation that in LEDs, other problems, probably related to the features of the *pn*-junction, lead to extremely small wall plug efficiencies.

As indicated by the fits of the EL and PL data, the poor CIE rather than the IQE is the main reason for the low EQE of the semipolar LEDs. The low CIE is presumably due to the inferior conductivity of the *p*-layers or the electron spill over caused by the non-optimized AlGaN electron blocking layer in the semipolar LEDs. Moreover, the

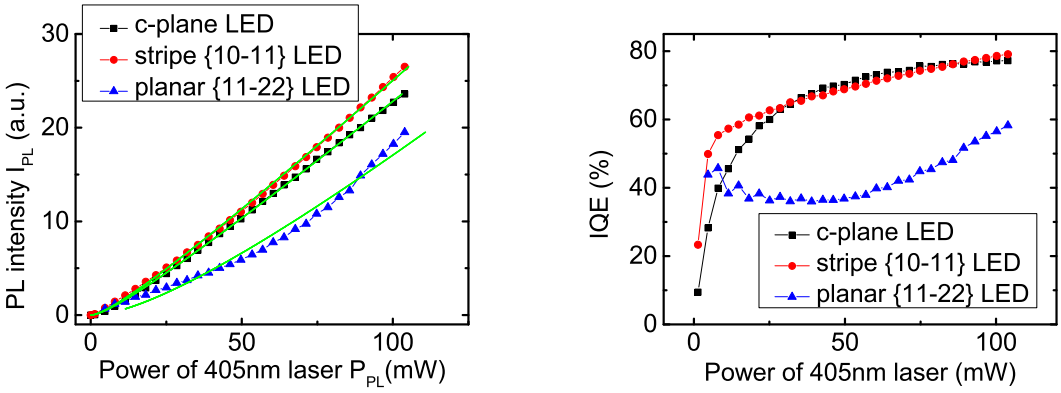

Figure 6.7.: The PL intensity I_{PL} dependent on the excitation power P_{PL} with the corresponding fitted curves (left) and the IQE estimated by the fit of the PL data (right) for the c-plane LED, the stripe $\{10\bar{1}1\}$ LED and the planar $\{11\bar{2}2\}$ LED. First published in [Wan16].

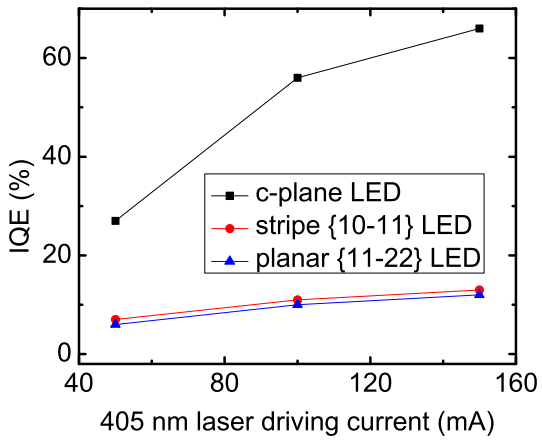

Figure 6.8.: Highest possible IQE at RT for *c*-plane, stripe $\{10\bar{1}1\}$ and planar $\{11\bar{2}2\}$ LEDs. The IQE values were calculated from the ratio of the PL intensities at RT and 13 K when exciting the samples with the 405 nm laser diode with driving currents of 50 mA, 100 mA and 150 mA, which correspond to the excitation densities of about 10, 100, and 200 W/cm^2, respectively.

stacking faults generated within the epilayers under the active region run in parallel to the QWs in the *c*-plane LED, but intersect the QWs in the semipolar LEDs [Far15] probably acting as a channel for leakage current.

The maximum values of IQE determined according to EL fit, PL fit, PL intensity ratio at low temperature (LT) and RT and EQE for our c-plane LED, the stripe $\{10\bar{1}1\}$ LED and the reference planar $\{11\bar{2}2\}$ LED are collected for a good overview (Table 6.2).

Table 6.2.: The maximum values of IQE determined according to EL fit, PL fit, PL intensity ratio at LT and RT and EQE for our c-plane LED, the stripe $\{10\bar{1}1\}$ LED and the reference planar $\{11\bar{2}2\}$ LED.

	maximum value of			
	IQE by EL fit	IQE by PL fit	IQE by PL ratio $\frac{\text{LT}}{\text{RT}}$	EQE
our c-plane LED	40%	78%	66%	6.6%
stripe $\{10\bar{1}1\}$ LED	46%	79%	12%	0.7%
reference planar $\{11\bar{2}2\}$ LED	40%	59%	11%	0.8%

CIE improvement via *p*-GaN optimization

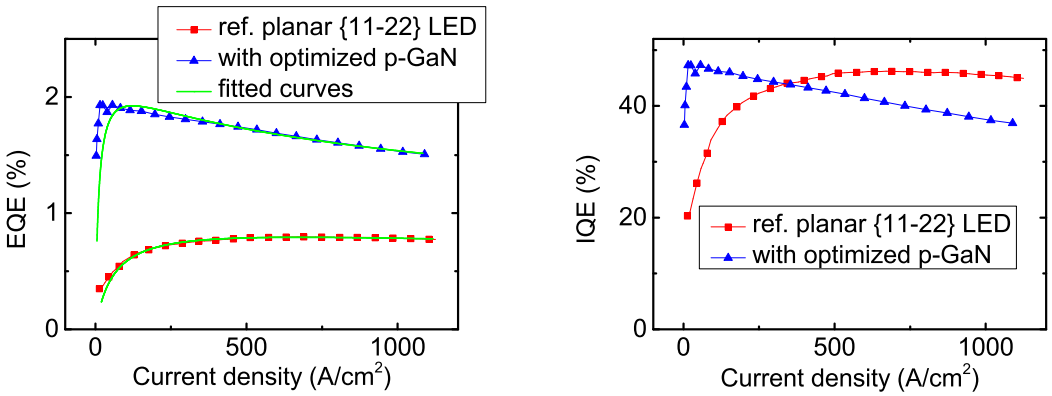

Figure 6.9.: The EQE (left) and the IQE (right) at different current densities for the planar $\{11\bar{2}2\}$ LED with the reference and optimized *p*-GaN. First published in [Wan16].

Actually lots of investigations have been done to suppress the *n*-type background carrier density aiming at better conductivity of the *p*-GaN on the planar $\{11\bar{2}2\}$ structure [Mei16]. The intentionally undoped $\{11\bar{2}2\}$ GaN may have an intrinsic *n*-doping concentration as high as $8\times10^{18}\,\text{cm}^{-3}$. In the *p*-GaN layer, the background *n*-type doping compensates the *p*-type one reducing its *p*-conductivity. Via the optimization of the growth rate and the growth temperature, the background *n*-doping concentration

could be reduced to $9 \times 10^{17}\,\mathrm{cm}^{-3}$ according to Hall measurements. Correspondingly, the EQE of the pulsed EL gets doubled by applying the optimized growth conditions for the p-GaN layer in the planar $\{11\bar{2}2\}$ LED (Fig. 6.9, left). The fit yields a CIE of 10 %, much higher than the 4 % CIE of the reference $\{11\bar{2}2\}$ LED discussed above. Meanwhile, fairly the same IQE values were determined for both LEDs as expected from the same QW growth conditions (Fig. 6.9, right).

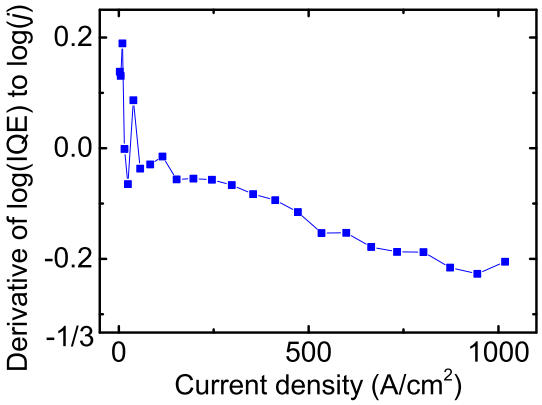

Figure 6.10.: Slope of the double logarithmic plot of the IQE against current density j for the planar $\{11\bar{2}2\}$ LED with improved p-GaN.

As discussed in section 6.1.2, the slope of the double logarithmic plot of the IQE against the current density j should be in the range from 1 to $-\frac{1}{3}$ according to the ABC model. The corresponding slope falls completely into this range for the $\{11\bar{2}2\}$ LED with the improved CIE indicating that the ABC model can describe this sample very well (Fig. 6.10). Again, the RRCs A and C are calculated from the coefficients of the linear and cubic terms of Equ. 6.15 (Table 6.1) assuming the B value of $3.6{\times}10^{-12}\,\mathrm{cm}^3\mathrm{s}^{-1}$, the same as the c-plane LED from OSRAM OS.

The IQE and the CIE of semipolar LEDs on GaN substrates

Is the low CIE an intrinsic problem of the semipolar GaN? To answer this question, we notice that Electrical and Computer Engineering Department in University of California, St. Barbara reported high-efficient semipolar LEDs grown on a native GaN substrate. Pulsed EL data with a duty cycle of 1 % was published in two papers, one for a $\{20\bar{2}\bar{1}\}$ LED [Zha11] and the other for a $\{10\bar{1}\bar{1}\}$ LED [Zha10a]. Hence, our fitting procedure could be nicely applied to the data in the former publication (Fig. 6.11, left). A LEE of 75 % is assumed since the EL measurement was conducted on the chip-level sample [Sch13]. CIE · LEE was determined to be 68 % leading to CIE > 68 %. Hence, this LED does not suffer from the poor carrier injection. The estimated IQE reaches its maximum of ∼80 % at a current density of $10\,\mathrm{A/cm}^2$ for the $\{20\bar{2}\bar{1}\}$ sample (Fig. 6.11, right). For the $\{10\bar{1}\bar{1}\}$ LED, the fit deviates from the EQE curve

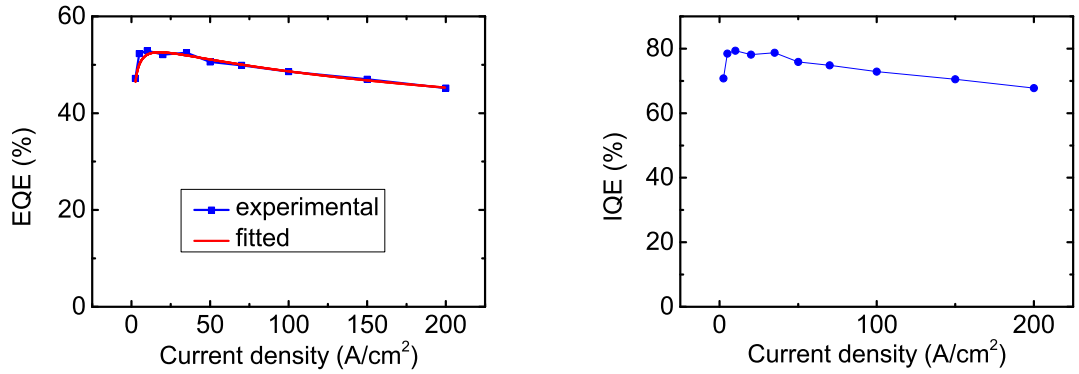

Figure 6.11.: The EQE curve according to the pulsed EL data and its fit (left) and the IQE curve determined by the fitting (right) dependent on the current density for the $\{20\bar{2}\bar{1}\}$ LED on the native GaN substrate.

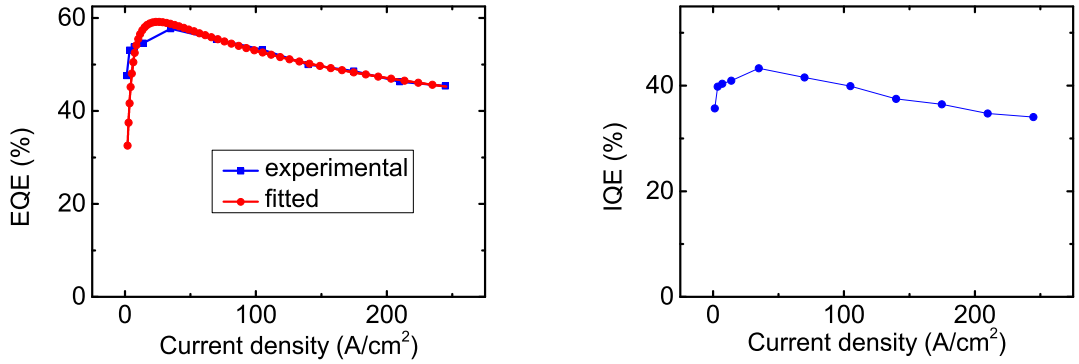

Figure 6.12.: The EQE curve according to the pulsed EL data and its fit (left) and the IQE curve determined by the fitting (right) dependent on the current density for the $\{10\bar{1}\bar{1}\}$ LED on the native GaN substrate.

according to the pulsed EL result much at low currents for the $\{10\bar{1}\bar{1}\}$ LED, leading to a large error bar of this fitting (Fig. 6.12, left). CIE · LEE is determined to be 1.3, i.e. beyond the theoretical limit of 100 % due to the large error, consequently leading to a CIE of 178 % exceeding its physical limit. The estimated IQE is anyway plotted in Fig. 6.12, right. We see that poor carrier injection limits the performance of the semipolar LEDs on the foreign substrate, but not the ones on the GaN native substrate.

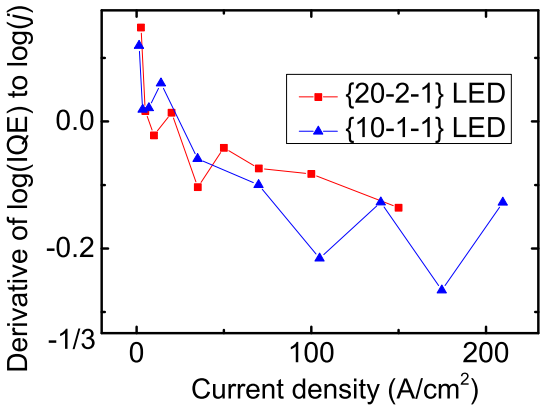

Figure 6.13.: Slope of the double logarithmic plot of the IQE against current density j for the $\{20\bar{2}\bar{1}\}$ and $\{10\bar{1}\bar{1}\}$ LEDs on the GaN native substrate.

The slope of the double logarithmic plot of the IQE against the current density j again falls completely into the expected range, from 1 to -$\frac{1}{3}$, for both semipolar LEDs on the GaN substrate (Fig. 6.13). Both the $\{20\bar{2}\bar{1}\}$ and $\{10\bar{1}\bar{1}\}$ LEDs contain three-fold QWs with an InGaN well thickness of 3 nm leading to d_{QW} of 9 nm. The B value of $3.6\times10^{-12}\,\mathrm{cm^3s^{-1}}$ is assumed to calculate the corresponding RRCs A and C, listed in Table 6.1.

6.1.4. Summary

Pulsed EL measurements were applied to c-plane, $\{10\bar{1}1\}$ and $\{11\bar{2}2\}$ LEDs. The chosen pulsing mode was a pulse width of 1 µsec and a duty cycle of 1 %. The fit of the pulsed EL data according to the ABC model allows to obtain the IQE and CIE values. The IQE is comparable for all three structures whereas the CIE is determined to be 78 % for the c-plane LED, but only about 4 % for its semipolar counterparts. IQE values obtained by fitting resonant PL data confirm these findings. Hence, a poor charge carrier injection is responsible for the lower efficiency of our semipolar LEDs grown on foreign substrates as compared to c-plane LEDs. The CIE was increased from 4 % to 10 % for a planar $\{11\bar{2}2\}$ LED by optimizing the p-GaN growth conditions contributing directly to the improved EL behaviour. The low CIE value is not an

intrinsic problem of the semipolar InGaN/GaN-based LEDs since the $\{20\bar{2}\bar{1}\}$ LED on the native GaN substrate shows a CIE value larger than 68 %.

6.2. Electron beam-induced current

The analysis of the electron beam-induced current (EBIC) applied in a SEM is a powerful LED analysis tool, capable to reveal the position and the material quality of the buried *pn*-junction as well as the minority carrier properties [Han81, Don83]. In EBIC, electron-hole pairs are generated by the incident electron beam and get separated by the internal electrical field within the space charge region of the *pn*-junction, leading to a current as the detected EBIC signal. This is similar to how a solar cell works except that the electron-hole pairs are generated by the electron beam instead of light. Since the EBIC signal is locally resolved as a consequence of the local excitation with the e-beam, one is able to apply spot-to-spot correlation between the EBIC signal and the locally-resolved QW characterization via CL. Consequently, two important aspects of the LED structure, the local *pn*-junction quality and the QW quality, are collected simultaneously enabling a good understanding which issue is essential to improve the LED performance.

It is challenging to detect the EBIC signal since it is very tiny, typically in the range of picoampere [Kna16]. On one hand, a current amplifier is integrated directly in the sample holder to suppress the stray capacitances and spurious interference (Fig. 6.14). On the other hand, contacts with low contact resistances are required. Hence, deposition of proper metal stacks and subsequent annealing procedure have been chosen for the contact preparation. Firstly, the *n*-GaN is exposed within half of the sample surface area by etching the layers above away with reactive ion etching. Then, metal stacks of Ti(15 nm)/Al(220 nm)/Ni(40 nm)/Au(50 nm) are deposited to form a single *n*-contact covering almost the whole exposed *n*-GaN surface (Fig. 6.15). Rectangular *p*-contacts distribute periodically over the *p*-GaN surface, formed via photolithography and metal evaporation of Pd(20 nm)/Au(100 nm). Finally, both, the *n*- and *p*-contact are annealed in N_2 atmosphere at a temperature of 500 °C for 5 min.

A weak EBIC signal indicates a reduced amount of separated charge carriers either due to a higher immediate recombination caused by higher defect density or disturbed internal electrical field within the space charge region when for example the doping profile of the *pn*-junction is imperfect. Two arrangements can be chosen for the EBIC measurement, top view and cross-sectional view (Fig. 6.16). In the former case, the electron beam is scanned over the device surface, telling the inhomogeneity of the *pn*-junction quality within a pretty large area ($\approx$mm^2) around the contact. This is very helpful to find out the local damage in terms of LED failure analysis. For the stripe LEDs, we got the chance to know if the *pn*-junction quality is homogeneous

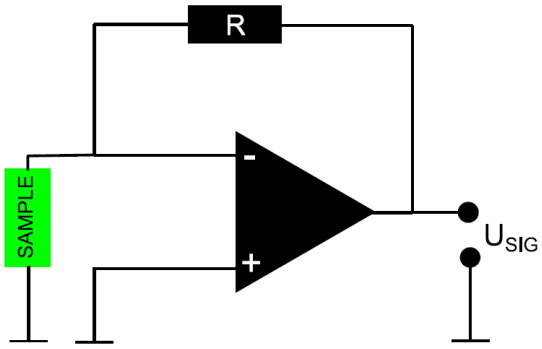

Figure 6.14.: EBIC measurement circuit with the current amplifier integrated on the sample holder.

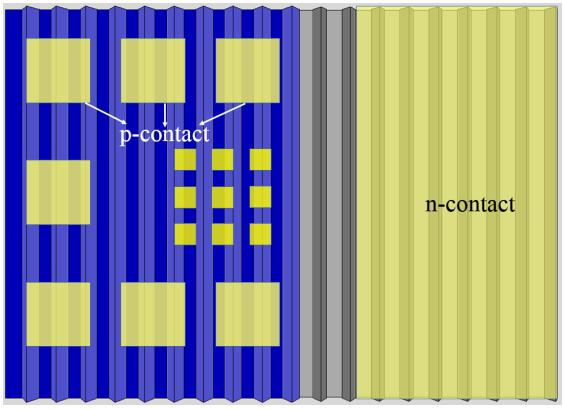

Figure 6.15.: Contact arrangement on the stripe LED surface for the EBIC measurement.

from stripe to stripe, along the stripes and perpendicular to the stripes over the facet. Actually, the homogeneity of the *pn*-junction quality over the facet is very interesting. Higher defect density was observed at the base of the stripes close to the SiO_2 epi-mask [Wun08a]. A higher indium concentration in the QW is found at the stripe apex (section 5.1). These are obvious reasons to expect different *pn*-junction quality at least at the base and the apex. In the case of the cross-sectional EBIC measurement, the electrons are scanned over the cross section perpendicular to the *pn*-junction, capable to determine the *pn*-junction position accurately. Moreover, the incident electrons don't need to penetrate through the p-(Al)GaN layers to reach the *pn*-junction as in the case of the top-view EBIC measurement, without being affected by the thickness variation of the p-(Al)GaN layers.

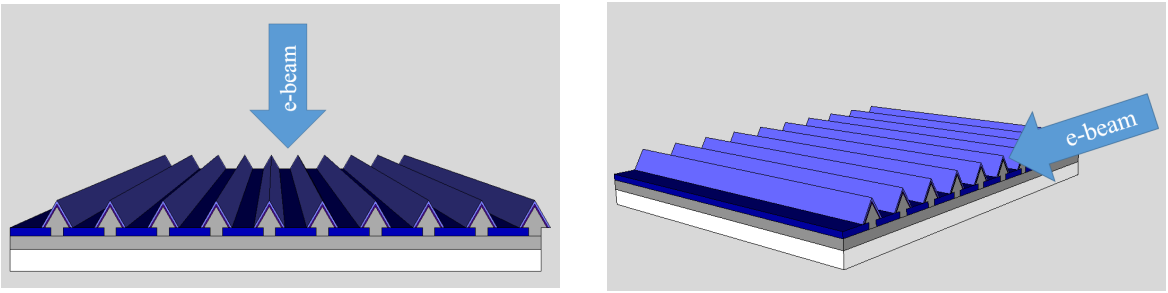

Figure 6.16.: Two arrangements of the EBIC measurements: top view (left) and cross-sectional view (right) with the stripe LED as an example.

6.2.1. Results and Discussions

EBIC and CL were applied on the same location of one stripe LED with 5QWs on the $\{10\bar{1}1\}$ facet without a *p*-AlGaN EBL (Fig. 6.17). Both, the EBIC and CL ex-

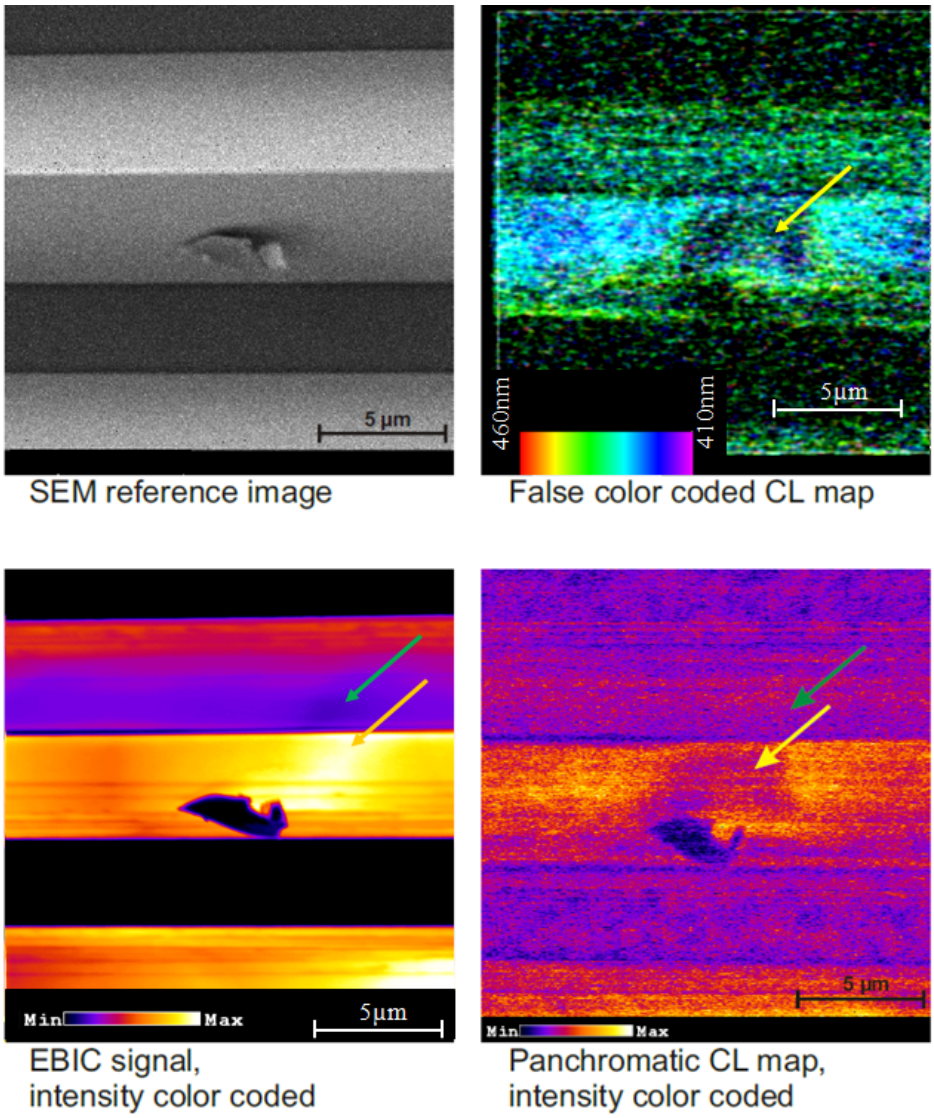

Figure 6.17.: Top view images of the SEM reference (upper left), the EBIC signal (lower left), the false color-coded CL map (upper right) and the panchromatic CL map (lower right) from the same location of the stripe $\{10\bar{1}1\}$ LED without *p*-AlGaN EBL.

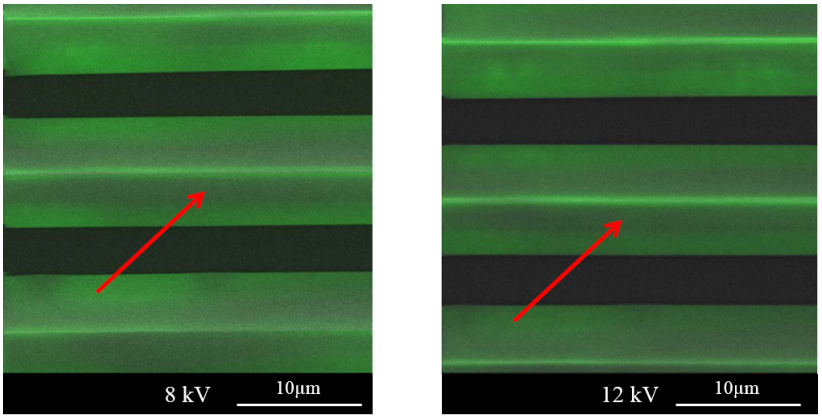

Figure 6.18.: Top view of the EBIC signal from the identical position of the sample investigated in Fig. 6.17. The acceleration voltage of the excitation electron was chosen to be 8 kV (left) and 12 kV (right).

periments were done by M. Knab in the Institute of Quantum Matter/Semiconductor Physics Group of Ulm University, Germany. The false color-coded CL image presents the dependency of the emission intensity on the emission wavelength. The light wavelength is indicated by the color which is actually not the light color in reality. The panchromatic CL map shows the total intensity at different positions regardless of the emission wavelength.

A dust particle on the stripe allows to retrieve the same position among different experiments so that a spot-to-spot correlation is possible. The EBIC signal is vanishing at the apex of the stripe as well as the corresponding CL signal. TEM shows crystal relaxation of the compressively strained QWs at the apex leading to a locally defective crystal structure, more indium incorporation and bending the QWs upwards (see section 5.4). The local defects disturb the pn-junction and the QW, responsible for the vanishing EBIC and CL signal. The higher indium concentration explains the red-shifted wavelength. The EBIC and CL signals fluctuate in the same way over most of the area on the lower part of the stripe. This may be caused either by a corresponding fluctuation of the QW quality and the *pn*-junction quality or a *p*-GaN thickness fluctuation. We conducted EBIC experiments with two different acceleration voltages of the excitation electron beam as 8 kV and 12 kV to exclude the latter case (Fig. 6.18). When the fluctuation of the EBIC and CL signals is caused by the *p*-GaN thickness variation, the contrast of the EBIC signal should get lighter and finally disappear when the electron penetration depth increases with increasing acceleration voltage. At 12 kV, the electron penetration depth is above 1.5 µm, much thicker than the *p*-GaN thickness of ∼200 nm and thick enough to eliminate the contrast caused by the *p*-GaN thickness fluctuation. However, the same contrast is observed under the two acceleration voltages. Therefore, the EBIC and CL fluctuation over the facet indeed indicates the corresponding fluctuation of the QW quality and the *pn*-junction quality rather than the *p*-GaN thickness fluctuation. In some regions, an anti-correlation

of the EBIC and CL signal - bright EBIC, dark CL and vice versa - also exists, for example, in the region marked by the yellow arrow and the higher part of the stripe (Fig. 6.17). The anti-correlation of bright EBIC and dark CL yields the information of a functional, high-quality *pn*-junction and defective QWs with less radiative recombination efficiency or easy carrier escape over a low barrier. The other combination of dark EBIC and bright CL indicates the disturbance of the *pn*-junction while the QW is o.k. [Kna16]. This is presumably due to the local disturbance of the p-doping profile.

EBIC contrast caused by AlGaN EBL inhomogeneity

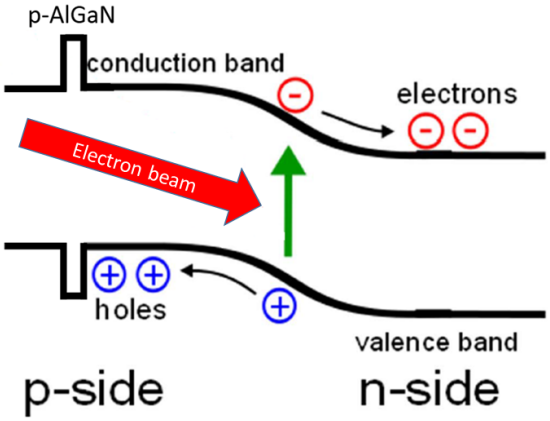

Figure 6.19.: Schematic procedure of the EBIC measurement in the LED with the *p*-AlGaN EBL.

As mentioned, electrons and holes are separated by the built-in field in the space charge region and flow to the *n*-side and the *p*-side of the *pn*-junction, respectively, forming the EBIC signal. The holes have to overcome the energetic barrier of the *p*-AlGaN acting as a hole blocking layer in the EBIC measurement (Fig. 6.19). Obviously, the inhomogeneity of the *p*-AlGaN layer will contribute to the contrast of the EBIC signal as well as that of the *pn*-junction.

Indeed, we observed irregular features in the EBIC signal of an LED which contains a *p*-AlGaN EBL (Fig. 6.20). The growth temperature was 1030 °C for the *p*-AlGaN layer. TEM was employed in order to find out the structural inhomogeneity of the *p*-AlGaN layer corresponding to the additional EBIC contrast as compared to the sample without the *p*-AlGaN discussed above. The *p*-AlGaN layer is ∼3 nm thick, ∼36 nm above the topmost QW. Intersecting defects through the *p*-AlGaN EBL are observed (Fig. 6.21). The darker contrast at some locations indicates a locally lower Al content. The periodic atomic alignment is disturbed at some other locations indicating some crystal structure transition from wurtzite to cubic (Fig. 6.22). These TEM features seem to correlate quite nicely with the EBIC results.

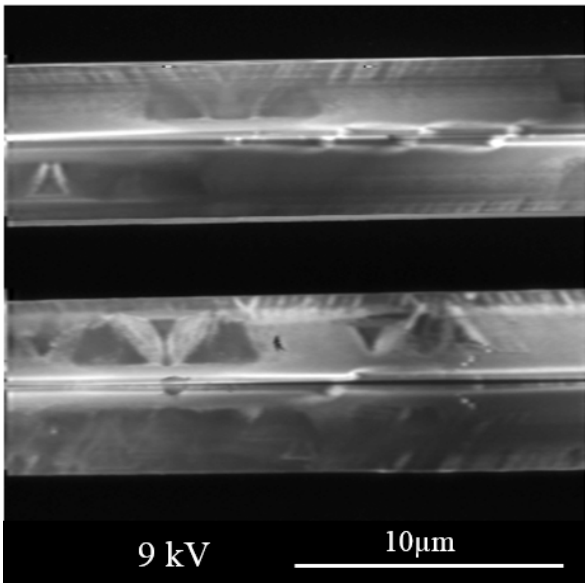

Figure 6.20.: Top view of the EBIC measurements for the stripe $\{10\bar{1}1\}$ LED with defective p-AlGaN EBL.

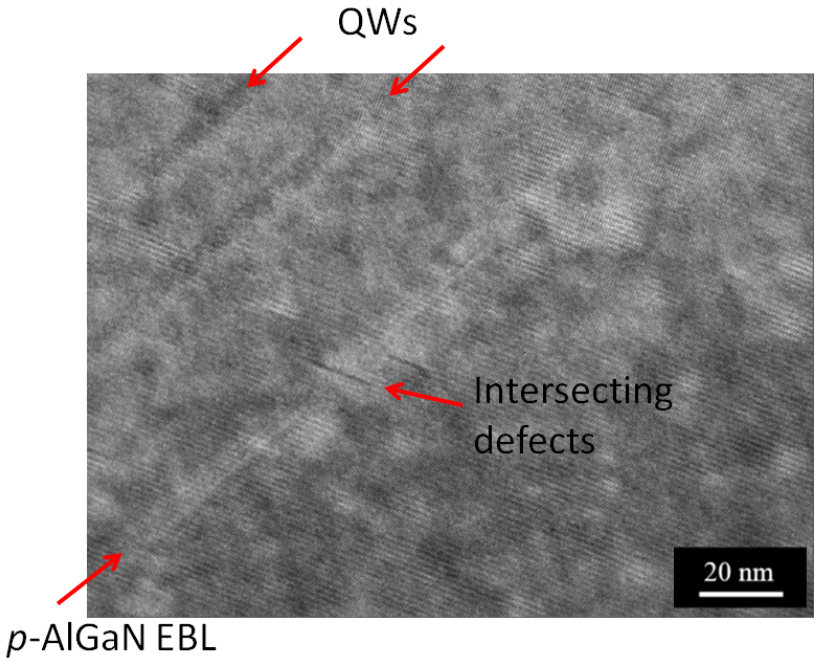

Figure 6.21.: TEM cross-section investigation of LED structure: defects intersecting the p-AlGaN EBL.

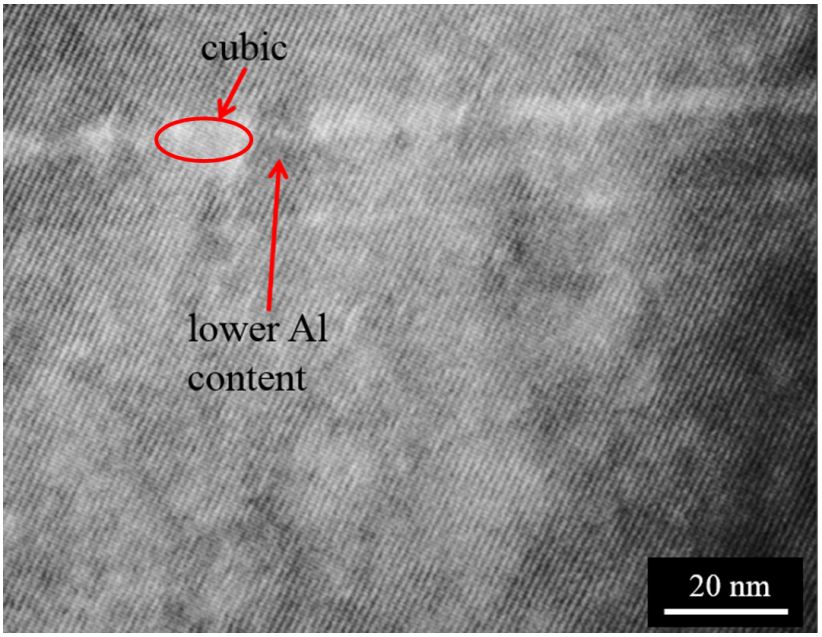

Figure 6.22.: TEM cross-section investigation of LED structure: locations in the *p*-AlGaN EBL with lower Al content and with cubic crystal structure.

By decreasing the growth temperature from 1030 °C to 980 °C for the *p*-AlGaN EBL we could suppress the development of such irregular features of the EBIC contrast (Fig. 6.23). This may be a consequence of a lower Al content at 980 °C resulting in better crystal quality.

6.2.2. Summary

A spot-to-spot correlation between EBIC and CL results was conducted for the stripe $\{10\bar{1}1\}$ LED without AlGaN EBL to obtain a thorough understanding of the LED structure in two respects, the *pn*-junction quality and the QW quality. A local high defect density was found at the apex leading to dark EBIC and CL signals. The inhomogeneity in the *pn*-junction as well as in the AlGaN EBL contributes to the EBIC contrast. Irregular features were observed in the EBIC top-view image when incorporating an AlGaN EBL into the stripe $\{10\bar{1}1\}$ LED, partly caused by basal plane stacking faults penetrating through it, as confirmed in TEM measurements on the same sample type. AlGaN EBL grown at a lower temperature helps to get rid of the irregular features in the EBIC measurement, speculatively due to better crystal quality with a lower Al content.

Both correlation and anti-correlation are found between EBIC and CL signals: vanishing signals for both methods indicate defective *pn*-junction and QWs while anti-correlation can be caused by a disturbed *pn*-junction with a good QW or vice versa.

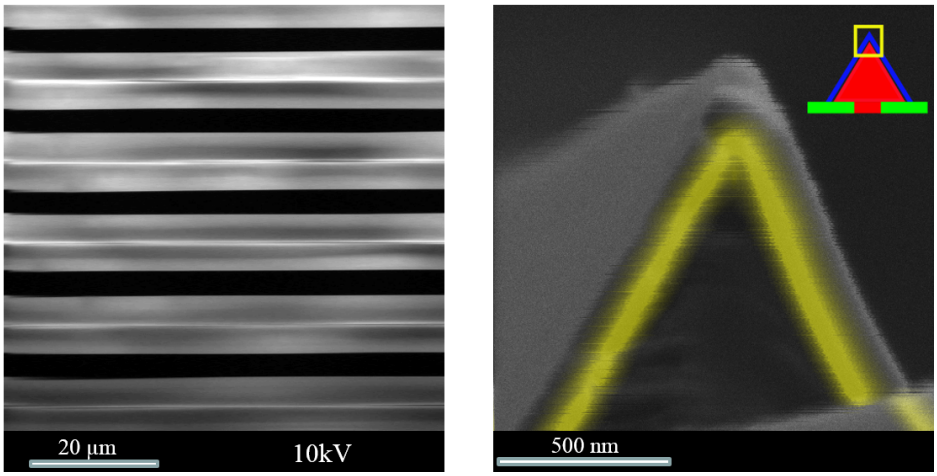

Figure 6.23.: Top view (left) and cross-sectional view (right) of the EBIC measurements for the stripe $\{10\bar{1}1\}$ LED with the *p*-AlGaN EBL grown at temperature of 980 °C.

7. Summary and Outlook

In this thesis, investigations of InGaN/GaN based 3D $\{10\bar{1}1\}$ LEDs, luminescence conversion structures and two LED evaluation methods, fitting of the EL data according to the famous ABC model and EBIC, are systematically carried out.

We found out how the electrical properties of a stripe $\{10\bar{1}1\}$ LED is affected by an individual functional layer: the SiO_2 epi-mask, the spacer, the main p-GaN layer and the p-contact layer. The insulation of the SiO_2 epi-mask is sufficient to block any significant leakage current flowing through it directly into n-GaN. A spacer thickness of 35 nm is found to be best to achieve the optimal EL output power for the stripe $\{10\bar{1}1\}$ LEDs. Enhancement of vertical growth in the spacer increases the EL output power, presumably due to a better Mg profile at the apex. SIMS analysis revealed the Mg concentration of the 3D semipolar p-GaN, indicating a higher Mg doping concentration on the $\{10\bar{1}1\}$ facet by a factor of 2.7 as compared to the $\{11\bar{2}2\}$ facet under the same growth conditions. The In incorporation efficiency is found to be about 30 % higher on the $\{10\bar{1}1\}$ facet than on the $\{11\bar{2}2\}$ facet by both methods of SIMS and PL. The EL output power is low with a too low Mg concentration of $3\times10^{19}\,\mathrm{cm}^{-3}$, probably due to an inferior hole injection efficiency, and stays almost constant with the Mg concentration ranging from $4\times10^{19}\,\mathrm{cm}^{-3}$ until $1.3\times10^{20}\,\mathrm{cm}^{-3}$ for the 3D LEDs with the $\{10\bar{1}1\}$ facet. The p-type contact performance was improved by excessive Mg doping.

Luminescence conversion structures with semipolar InGaN/GaN QWs based on our 3D inverse pyramidal structure were investigated. By choosing low temperature, a high V/III ratio and a small filling ratio of the SiO_2 growth mask, $\{11\bar{2}2\}$ facets can be suppressed on GaN inverse pyramids in favor of $\{10\bar{1}1\}$ facets. InGaN/GaN QWs grown on the latter show a higher crystalline quality leading to a 30 % increase of the conversion rate η_c for green InGaN based converter structures. It is confirmed by transmission experiments that the absorption fraction η_a increases monotonously with more QWs but the conversion rate η_c decreases when the number of QWs is too high. The structure with 15 QWs offers a good balance between these two parameters achieving the strongest green emission based on our current epitaxy conditions. The conversion efficiency is greatly dependent on the fact whether the sample is excited from the epi-side or the sapphire-side. When the late grown QW is put close to the excitation source, η_c increases by nearly 90 % compared to that with the excitation light coupled into the converter from the other substrate side. We conclude that the thermal load is the main mechanism responsible for the QW degradation in the green

converter. The InGaN growth conditions (reactor pressure, TMIn molar flow and TEGa molar flow) are optimized in order to increase the growth temperature for the same QW emission wavelength and hence increase η_c for the conversion structure.

Pulsed EL measurements with a duty cycle of 1 % were applied to *c*-plane, $\{10\bar{1}1\}$ and $\{11\bar{2}2\}$ LEDs to avoid diode heating. The fit of the EL data according to the ABC model allows us to obtain the IQE and CIE values. The IQE is comparable for all three structures whereas the CIE is determined to be 78 % for the *c*-plane LED, but only about 4 % for its semipolar counterparts. IQE values obtained by fitting resonant PL data confirm these findings. Hence, a poor charge carrier injection is responsible for the lower efficiency of our semipolar LEDs grown on foreign substrates as compared to *c*-plane LEDs. The CIE was increased from 4 % to 10 % for the planar $\{11\bar{2}2\}$ LED by optimizing the *p*-GaN growth condition contributing directly to the improved EL behavior. The low CIE value is not an intrinsic problem of the semipolar InGaN/GaN-based LEDs since $\{20\bar{2}\bar{1}\}$ LEDs on native GaN substrate (data taken from literature) show a CIE value larger than 68 %. A spot-to-spot correlation between EBIC and CL results was conducted for the stripe $\{10\bar{1}1\}$ LED without AlGaN EBL to obtain a thorough understanding of the LED structure in two respects, the *pn*-junction quality and the QW quality. A local high defect density was found at the apex leading to dark EBIC and CL signals. Some inhomogeneity in the *pn*-junction as well as in the AlGaN EBL contributes to the EBIC contrast. Irregular features were observed in the EBIC top-view image when incorporating an AlGaN EBL into the stripe $\{10\bar{1}1\}$ LED, partly caused by basal plane stacking faults penetrating through it, as confirmed in TEM measurements on the same sample type. AlGaN EBL grown at a lower temperature helps to get rid of the irregular features in the EBIC measurement, speculatively due to better crystal quality with a lower Al content. Both correlation and anti-correlation are found between EBIC and CL signals: vanishing signals for both methods indicate defective *pn*-junction and QWs while anti-correlation can be disturbed pn-junction with a good QW or vice versa.

We obtained improvement and a good understanding of electrical and luminescent properties of 3D semipolar LEDs by this work. Further investigations of LED's epitaxial growth to improve the CIE is planned as an outlook. A correlation between the CIE and the EBIC result may lighten the investigation.

ïżŁ

Bibliography

[Adh04] J. Adhikari, D.A. Kofke. *Molecular simulation study of miscibility of ternary and quaternary InGaAlN alloys.* J. Appl. Phys. **95**, 6129, 2004.

[Ama89] H. Amano, M. Kito, K. Hiramatsu, I. Akasaki. *P-type conduction in Mg-doped GaN treated with low-energy electron beam irradiation (LEEBI).* Jpn. J. Appl. Phys. **28**, L2112, 1989.

[Ama90] H. Amano, M. Kitoh, K. Hiramatsu, I. Akasaki. *Growth and luminescence properties of Mg-doped GaN prepared by MOVPE.* J. Electrochem. Soc. **137**, 1639, 1990.

[Bhu03] A.G. Bhuiyan, A. Haoto, A. Yamamoto. *Indium nitride (InN): A review on growth, characterization, and properties.* J. Appl. Phys. **94**, 2779, 2003.

[Blo74] S. Bloom, G. Harbeke, E. Meier, I.B. Ortenburger. *Band Structure and Reflectivity of GaN.* Phys. Status Solidi B **66**, 161, 1974.

[Bul06] K.A. Bulashevich, S.Y. Karpov, R.A. Suris. *Analytical model for the quantum-confined Stark effect including electric field screening by non-equilibrium carriers.* Phys. Status Solidi B **243**, 1625, 2006.

[Cho01] H.K. Cho, J.Y. Lee, N. Sharma, C.J. Humphreys, G.M. Yang, C.S. Kim, J.H. Song, P.W. Yu. *Effect of growth interruptions on the light emission and indium clustering of InGaN/GaN multiple quantum wells.* Appl. Phys. Lett. **79**, 2594, 2001.

[Cru09] S.C. Cruz, S. Keller, T.E. Mates, U.K. Mishra, S.P. DenBaars. *Crystallographic orientation dependence of dopant and impurity incorporation in GaN films grown by metalorganic chemical vapor deposition.* J. Cryst. Growth **311**, 3817, 2009.

[Dai09] Q. Dai, M.F. Schubert, M.H. Kim, J.K. Kim, E.F. Schubert, D.D. Koleske, M.H. Crawford, S.R. Lee, A.J. Fischer, G. Thaler, M.A. Banas. *Internal quantum efficiency and nonradiative recombination coefficient of GaInN/GaN multiple quantum wells with different dislocation densities.* Appl. Phys. Lett. **94**, 111109, 2009.

[Dav10] A. David, M.J. Grundmann. *Influence of polarization fields on carrier lifetime and recombination rates in InGaN-based light-emitting diodes.* Appl. Phys. Lett. **97**, 033501, 2010.

[Don83] C. Donolato. *Evaluation of diffusion lengths and surface recombination velocities from electron beam induced current scans.* Appl. Phys. Lett. **43**, 120, 1983.

[Far15] S. Faraji. *Epitaxy and characterization of semi-polar (10$\bar{1}$1) and (20$\bar{2}$1) GaN-based hetero-structures on (11$\bar{2}$3) and (22$\bar{4}$3) patterned sapphire substrate.* Master thesis, Universität Ulm, Institut für Optoelektronik der Fakultät für Ingenieurwissenschaften und Informatik, 2015.

[Fik14] M. Fikry. *Epitaxial growth and characterization of coaxial GaN/InGaN/GaN nano-structures.* Dissertation, Universität Ulm, 2014.

[Fis09] A.M. Fischer, Z. Wu, K. Sun, Q. Wei, Y. Huang, R. Senda, D. Iida, M. Iwaya, H.Amano, F.A. Ponce. *Misfit strain relaxation by stacking fault generation in InGaN quantum wells grown on m-plane GaN.* Appl. Phys. Express **2**, 041002, 2009.

[For08] K. Forghani. *Investigations on MOVPE growth of AlGaN heterostructures for UV LED applications.* Masterarbeit, Universität Ulm, Institut für Optoelektronik der Fakultät für Ingenieurwissenschaften und Informatik, 2008.

[Fuj04] T. Fujii, Y. Gao, R. Sharma, E.L. Hu, S.P. DenBaars, S. Nakamura. *Increase in the extraction efficiency of GaN-based light-emitting diodes via surface roughening.* Appl. Phys. Lett. **84**, 855, 2004.

[Fuj08] K. Fujito, K. Kijomi, T. Mochizuki, H. Oota, H. Namita, S. Nagao, I. Fujimura. *High-quality nonpolar m-plane GaN substrates grown by HVPE.* Phys. Status Solidi A **5**, 1056, 2008.

[Göt96] W. Götz, N.M. Johnson, C. Chen, H. Liu, C. Kuo, W. Imler. *Activation energies of Si donors in GaN.* Appl. Phys. Lett. **68**, 3144, 1996.

[Gal11] B. Galler, M. Sabathil, A. Laubsch, T. Meyer, L. Hoeppel, G. Kraeuter, H. Lugauer, M. Strassburg, M. Peter, A. Biebersdorf, U. Steegmueller, B. Hahn. *Green high-power light sources using InGaN multi-quantum-well structures for full conversion.* Phys. Status Solidi C **8**, 2369, 2011.

[Grz01] Izabella Grzegory. *High pressure growth of bulk GaN from solutions in gallium.* J. Phys.: Condens. Matter **13**, 6875, 2001.

[Han81] J.I. Hanoka, R.O. Bell. *Electron-beam-induced currents in semiconductors.* Ann. Rev. Mater. Sci. **11**, 353, 1981.

[Her08] J. Hertkorn, F. Lipski, P. Brückner, T. Wunderer, S.B. Thapa, F. Scholz, A. Chuvilin, U. Kaiser, M. Beer, J. Zweck. *Process optimization for the effective reduction of threading dislocations in MOVPE grown GaN using in situ deposited SiN_x masks.* J. Cryst. Growth **310**, 4867, 2008.

[Her09] J. Hertkorn. *Verbesserung der lateralen Stromführung in hocheffizienten Halbleiterlichtquellen.* Dissertation, Universität Ulm, Institut für Optoelektronik der Fakultät für Ingenieurwissenschaften und Informatik, 2009.

[Hol06] D. Holec. *Critical thickness calculations for $In_xGa_{1-x}N/GaN$ systems.* Dissertation, University of Cambridge, 2006.

[Hol07] D. Holec, P.M.F.J. Costa, M.J. Kappers, C.J. Humphreys. *Critical thickness calculations for InGaN/GaN.* J. Cryst. Growth **303**, 314, 2007.

[Hsu12] P. Shan Hsu, M.T. Hardy, E.C. Young, A.E. Romanov, S.P. DenBaars, S. Nakamura, J.S. Speck. *Stress relaxation and critical thickness for misfit dislocation formation in $\{10\bar{1}0\}$ and $\{303\bar{1}\}$ InGaN/GaN heteroepitaxy.* Appl. Phys. Lett. **100**, 171917, 2012.

[Jeo13] J. Jeong, J. Jang, J. Hwang, C. Jung, J. Kim, K. Lee, H. Lim, O. Nam. *Improved performance of semi-polar $(11\bar{2}2)$ GaN-based light-emitting diodes grown on SiN_x interlayer.* J. Cryst. Growth **370**, 114, 2013.

[Jho01] Y.D. Jho, J.S. Yahng, E. Oh, D.S. Kim. *Measurement of piezoelectric field and tunneling times in strongly biased InGaN/GaN quantum wells.* Appl. Phys. Lett. **79**, 1130, 2001.

[Köh05] K. Köhler, T. Stephan, A. Perona, J. Wiegert, M. Maier, M. Kunzer, J. Wagner. *Control of the Mg doping profile in III-N light-emitting diodes and its effect on the electroluminescence efficiency.* J. Appl. Phys. **97**, 104914, 2005.

[Kau00] U. Kaufmann, P. Schlotter, H. Obloh, K. Köhler, M. Maier. *Hole conductivity and compensation in epitaxial GaN:Mg layers.* Phys. Rev. B **62**, 10867, 2000.

[Kim07] T.K. Kim, S.K. Shim, S.S. Yang, J.K. Son, Y.K. Hong, G.M. Yang. *Influence of growth parameters on the properties of InGaN/GaN multiple quantum well grown by metalorganic chemical vapor deposition.* Curr. Appl. Phys. **7**, 469, 2007.

[Kim13] D.S. Kim, S. Lee, D. Young Kim, S.K. Sharma, S.-M. Hwang, Y. Gon Seo.

Highly stable blue-emission in semipolar $(11\bar{2}2)$ *InGaN/GaN multi-quantum well light-emitting diode.* Appl. Phys. Lett. **103**, 021111, 2013.

[Kna16] M. Knab, M. Hocker, T. Felser, I. Tischer, J. Wang, F. Scholz, K. Thonke. *EBIC investigations on polar and semipolar InGaN LED structures.* Phys. Status Solidi B **253**, 126, 2016.

[Kos10] I.L. Koslow, J. Sonoda, R.B. Chung, C.-C. Pan, S. Brinkley, H. Ohta, S. Nakamura, S.P. DenBaars. *High power and high efficiency blue InGaN light emitting diodes on free-standing semipolar* $(30\bar{3}\bar{1})$ *bulk GaN substrate.* Jpn. J. Appl. Phys. **49**, 080203, 2010.

[Lee07] T.-X. Lee, K.-F. Gao, W.-T. Chien, C.-C. Sun. *Light extraction analysis of GaN-based light-emitting diodes with surface texture and/or patterned substrate.* Optics Express **15**, 6670, 2007.

[Li17] Y. Li, H. Qi, T. Meisch, M. Hocker, K. Thonke, F. Scholz, U. Kaiser. *Formation of* I_2*-type basal-plane stacking faults in* $In_{0.25}Ga_{0.75}N$ *multiple quantum wells grown on a* $(10\bar{1}1)$ *semipolar GaN template.* Appl. Phys. Lett. **110**, 022105, 2017.

[Lip10] F. Lipski, T. Wunderer, S. Schwaiger, F. Scholz. *Fabrication of freestanding* $2'$*-GaN wafers by hydride vapour phase epitaxy and self-separation during cooldown.* Phys. Status Solidi A pages 1287–1291, 2010.

[Liu06a] R. Liu, J. Mei, S. Srinivasan, H. Omiya, F.A. Ponce, D. Cherns, Y. Narukawa, T. Mukai. *Misfit dislocation generation in InGaN epilayers on free-standing GaN.* Jpn. J. Appl. Phys. **45**, L549, 2006.

[Liu06b] R. Liu, J. Mei, S. Srinivasan, F.A. Ponce, H. Omiya, Y. Narukawa, T. Mukai. *Generation of misfit dislocations by basal-plane slip in InGaNâĹŢGaN heterostructures.* Appl. Phys. Lett. **89**, 201911, 2006.

[Mei07a] J. Mei, R. Liu, F.A. Ponce, H. Omiya, T. Mukai. *Basal-plane slip in InGaNâĹŢGaN heterostructures in the presence of threading dislocations.* Appl. Phys. Lett. **90**, 171922, 2007.

[Mei07b] J. Mei, F.A. Ponce, R.S. Qhalid Fareed, J.W. Yang, M.A. Khan. *Dislocation generation at the coalescence of aluminum nitride lateral epitaxy on shallow-grooved sapphire substrates.* Appl. Phys. Lett. **90**, 221909, 2007.

[Mei16] T. Meisch, R. Zeller, S. Schörner, K. Thonke, L. Kirste, T. Fuchs, F. Scholz. *Doping behavior of* $(11\bar{2}2)$ *GaN grown on patterned sapphire substrates.* Phys. Status Solidi B **253**, 164, 2016.

[Mey13] D.J. Meyer, D.A. Deen, D.F. Storm, M.G. Ancona, D.S. Katzer, R. Bass,

J.A. Roussos, B.P. Downey, S.C. Binari, T. Gougousi, T. Paskova, E.A. Preble, K.R. Evans. *High electron velocity submicrometer AlN/GaN MOS-HEMTs on freestanding GaN substrates.* IEEE Electron Dev. Lett. **34**, 199, 2013.

[Mey14] T. Meyer. Private Communication, 2014. OSRAM OS.

[Mil05] Alan Mills. *Phosphors development for LED lighting.* III-Vs Review **18**, 32, 2005.

[Mis03] C.R. Miskys, M.K. Kelly, O. Ambacher, M. Stutzmann. *Freestanding GaN-substrates and devices.* Phys. Status Solidi C **0**, 1627, 2003.

[Mor09] M.A. Moram, C.S. Ghedia, D.V.S. Rao, J.S. Barnard, Y. Zhang, M.J. Kappers, C.J. Humphreys. *On the origin of threading dislocations in GaN films.* J. Appl. Phys. **106**, 073513, 2009.

[Nak92] S. Nakamura, T. Mukai, M. Senoh, N. Iwasa. *Thermal annealing effects of p-type Mg-doped GaN films.* Jpn. J. Appl. Phys. **31**, L139, 1992.

[Nak00] S. Nakamura, S. Chichibu. *Introduction to nitride semiconductor blue lasers and light emitting diodes.* Taylor and Francis, London, 2000.

[Nak13] S. Nakamura, M.R. Krames. *History of gallium-nitride-based light-emitting diodes for illumination.* Proc. IEEE **101**, 2211, 2013.

[Neu05] Barbara Neubert, Peter Brückner, Frank Habel, Ferdinand Scholz, Till Riemann, Jürgen Christen, Martin Beer, Joseph Zweck. *GaInN quantum wells grown on facets of selectively grown GaN stripes.* Appl. Phys. Lett. **87**, 182111, 2005.

[Oka09] N. Okada, A. Kurisu, K. Murakami, K. Tadatomo. *Growth of semipolar (11$\bar{2}$2) GaN layer by controlling anisotropic growth rates in* r*-plane patterned sapphire substrate.* Appl. Phys. Express **2**, 091001, 2009.

[Oka12] N. Okada, K. Uchida, S. Miyoshi, K. Tadatomo. *Green light-emitting diodes fabricated on semipolar (11$\bar{2}$2) GaN on* r*-plane patterned sapphire substrate.* Phys. Status Solidi A **209**, 469, 2012.

[Per09] P. Perlin, G. Franssen, J. Szeszko, R. Czernecki, G. Targowski, M. Kryśko, S. Grzanka, G. Nowak, E. Litwin-Staszewska, R. Piotrzkowski, M. Leszczyński, B. Łucznik, I. Grzegory, R. Jakieła, M. Albrecht, T. Suski. *Nitride-based quantum structures and devices on modified GaN substrates.* Phys. Status Solidi A **206**, 1130, 2009.

[Pip07] J. Piprek, editor. *Nitride Semiconductor Devices - Principles and Simula-*

tions. Wiley VCH Verlag GmbH, 1. edition, 2007.

[Pow93] R.C. Powell, N.-E. Lee, Y.-W. Kim, J.E. Greene. *Heteroepitaxial wurtzite and zinc-blende structure GaN grown by reactive-ion molecular beam epitaxy: Growth kinetics, microstructure, and properties.* J. Appl. Phys. **73**, 189, 1993.

[Sch07] U. Schwarz, M. Kneissl. *Nitride emitters go nonpolar.* Phys. Status Solidi (RRL) **1**, A44, 2007.

[Sch11a] F. Scholz. *Compound semiconductors: Physics, technology and device concepts.* Universität Ulm, Institut für Optoelektronik, 2011.

[Sch11b] S. Schwaiger, S. Metzner, T. Wunderer, I. Argut, J. Thalmair, F. Lipski, M. Wieneke, J. Blaesing, F. Bertram, J. Zweck, A. Krost, J. Christen, F. Scholz. *Growth and coalescence behaviour of semipolar* $\{11\bar{2}2\}$ *GaN on pre-strucured r-plane sapphire substrates.* Phys. Status Solidi B **248**, 588, 2011.

[Sch12] F. Scholz, S. Schwaiger, J. Däubler, I. Tischer, K. Thonke, S. Neugebauer, S. Metzner, F. Bertram, J. Christen, H. Lengner, J. Thalmair, J. Zweck. *Semipolar GaInN quantum well structures on large area substrates.* Phys. Status Solidi B **249**, 464, 2012.

[Sch13] D. Schiavon. *Analysis of the green gap problem in the III-nitride LEDs.* Dissertation, Universität Ulm, 2013.

[Sch14] F. Scholz, T. Meisch, M. Caliebe, S. Schörner, K. Thonke, L. Kirste, S. Bauer, S. Lazarev, T. Baumbach. *Growth and doping of semipolar GaN grown on patterned sapphire substrates.* J. Cryst. Growth **405**, 97, 2014.

[SH11] P. Shan Hsu, E.C. Young, A.E. Romanov, K. Fujito, S.P. DenBaars, S. Nakamura, J.S. Speck. *Misfit dislocation formation via pre-existing threading dislocation glide in* $(11\bar{2}2)$ *semipolar heteroepitaxy.* Appl. Phys. Lett. **99**, 081912, 2011.

[SH12a] P. Shan Hsu, M.T. Hardy, F. Wu, I. Koslow, E.C. Young, A.E. Romanov, K. Fujito, D.F. Feezell, S.P. DenBaars, J.S. Speck, S. Nakamura. *444.9 nm semipolar* $(11\bar{2}2)$ *laser diode grown on an intentionally stress relaxed InGaN waveguiding layer.* Appl. Phys. Lett. **100**, 021104, 2012.

[SH12b] P. Shan Hsu, M.T. Hardy, E.C. Young, A.E. Romanov, S.P. DenBaars, S. Nakamura, J.S. Speck. *Stress relaxation and critical thickness for misfit dislocation formation in* $(10\bar{1}0)$ *and* $(30\bar{3}1)$ *InGaN/GaN heteroepitaxy.* Appl. Phys. Lett. **100**, 171917, 2012.

[She07] Y.C. Shen, G.O. Mueller, S. Watanabe, N.F. Gardner, A. Munkholm, M.R. Krames. *Auger recombination in InGaN measured by photoluminescence.* Appl. Phys. Lett. **91**, 141101, 2007.

[Sho52] W. Shockley, W.T. Read. *Statistics of the recombinations of holes and electrons.* Phys. Rev **87**, 835, 1952.

[Sta98] C. Stampfl, Chris G. Van de Walle. *Energetics and electronic structure of stacking faults in AlN, GaN, and InN.* Phys. Rev. B **57**, R15052, 1998.

[Str99] G.B. Stringfellow. *Organometallic vapor-phase epitaxy: theory and practice.* Academic Press, San Diego, 1999.

[Tha10] S.B. Thapa. *Studies of AlN grown by MOVPE for electronic and optoelectronic applications.* Dissertation, Universität Ulm, 2010.

[Try09] E. Trybus, W.A. Doolittle, M. Moseley, W. Henderson, D. Billingsley, G. Namkoong, D.C. Look. *Extremely high hole concentrations in* c*-plane GaN.* Phys. Status Solidi C **6**, S788, 2009.

[Tya09] A. Tyagi, F. Wu, E.C. Young, A. Chakraborty, H. Ohta, R. Bhat, K. Fujito, S.P. DenBaars, S. Nakamura, J.S. Speck. *Partial strain relaxation via misfit dislocation generation at heterointerfaces in (Al,In)GaN epitaxial layers grown on semipolar (11$\bar{2}$2) GaN free standing substrates.* Appl. Phys. Lett. **95**, 251905, 2009.

[Uch13] K. Uchida, S. Miyoshi, K. Yamane, N. Okada, K. Tadatomo, N. Kuwano. *Evaluation of* {11$\bar{2}$2} *semipolar multiple quantum wells using relaxed thick InGaN layers with various In compositions.* Jpn. J. Appl. Phys. **52**, 08JC07, 2013.

[Vur03] I. Vurgaftman, J.R. Meyer. *Band parameters for nitrogen-containing semiconductors.* J. Appl. Phys. **94**, 3675, 2003.

[Wan13] J. Wang, D. Zhang, R.A.R. Leute, T. Meisch, D. Heinz, I. Tischer, M. Hocker, K. Thonke, F. Scholz. *InGaN/GaN based semipolar green converters.* J. Cryst. Growth **370**, 120, 2013.

[Wan14] J. Wang, Y. Gao, S. Alam, F. Scholz. *Mg doping of 3D semipolar InGaN/GaN-based light emitting diodes.* Phys. Status Solidi A **211**, 2645, 2014.

[Wan16] J. Wang, T. Meisch, D. Heinz, R. Zeller, F. Scholz. *Internal quantum efficiency and carrier injection efficiency of c-plane,* {10$\bar{1}$1} *and* {11$\bar{2}$2} *InGaN/GaN-based light-emitting diodes.* Phys. Status Solidi B **253**, 174, 2016.

[Wei01] A. Weimar, A. Lell, G. Brüderl, S. Bader, V. Härle. *Investigation of low-resistance metal contacts on p-type GaN using the linear and circular transmission line method.* Phys. Status Solidi A **183**, 169, 2001.

[Wu11] Z.H. Wu, T. Tanikawa, T. Murase, Y.-Y. Fang, C.Q. Chen, Y. Honda, M. Yamaguchi, H. Amano, N. Sawaki. *Partial strain relaxation by stacking fault generation in InGaN multiple quantum wells grown on (1$\bar{1}$01) semipolar GaN.* Appl. Phys. Lett. **98**, 051902, 2011.

[Wu13] L.L. Wu, D.G. Zhao, D.S. Jiang, P. Chen, L.C. Le, L. Li, Z.S. Liu, S.M. Zhang, J.J. Zhu, H. Wang, B.S. Zhang, H. Yang. *Effects of thin heavily Mg-doped GaN capping layer on ohmic contact formation of p-type GaN.* Semicond. Sci. Technol. **28**, 105020, 2013.

[Wun06] T. Wunderer, P. Br/"uckner, B. Neubert, F. Scholz, M. Feneberg, F. Lipski, M. Schirra, K. Thonke. *Bright semipolar GaInNâĹŢGaN blue light emitting diode on side facets of selectively grown GaN stripes.* Appl. Phys. Lett. **89**, 041121, 2006.

[Wun08a] T. Wunderer, J. Hertkorn, F. Lipski, P. Brückner, M. Feneberg, M. Schirra, K. Thonke, I. Knoke, E. Meissner, A. Chuvilin, U. Kaiser, F. Scholz. *Optimization of semipolar GaInN/GaN blue/green light emitting diode structures on* {1$\bar{1}$01} *GaN side facets.* Proc. of SPIE 6894; Gallium Nitride Materials, Devices III (H. Morkoç, C.W. Litton, J.-I. Chyi, Y. Nanishi, E. Yoon, Eds.) pages 68940V–1–9, 2008.

[Wun08b] T. Wunderer, F. Lipski, J. Hertkorn, P. Bückner, F. Scholz, M. Feneberg, M. Schirra, K. Thonke, A. Chuvilin, U. Kaiser. *Bluish-green semipolar GaInN/GaN light emitting diodes on 1$\bar{1}$01 GaN side facets.* Phys. Status Solidi C **5**, 2059, 2008.

[Wun09] T. Wunderer, F. Lipski, J. Hertkorn, S. Schwaiger, F. Scholz. *Fabrication of 3D InGaN/GaN structures providing semipolar GaN planes for efficient green light emission.* Phys. Status Solidi C **6**, S490, 2009.

[Wun10] T. Wunderer. *Dreidimensionale Licht emittierende GaInN/GaN-Strukturen mit reduziertem piezoelektrischen Feld.* Dissertation, Universität Ulm, 2010.

[Wun11] T. Wunderer, M. Feneberg, F. Lipski, J. Wang, R.A.R. Leute, S. Schwaiger, K. Thonke, A. Chuvilin, U. Kaiser, S. Metzner, F. Bertram, J. Christen, G.J. Beirne, M. Jetter, P. Michler, L. Schade, C. Vierheilig, U.T. Schwarz, A.D. Draeger, A. Hangleiter, F. Scholz. *Three-dimensional GaN for semipolar light emitters.* Phys. Status Solidi B **248**, 549, 2011.

[Yan14] Q. Yan, P. Rinke, A. Janotti, M. Scheffler, Chris G. Van de Walle. *Effects of strain on the band structure of group-III nitrides.* Phys. Rev. B **90**, 125118,

2014.

[You10] E.C. Young, C.S. Gallinat, A.E. Romanov, A. Tyagi, F. Wu, J.S. Speck. *Critical thickness for onset of plastic relaxation in* $(11\bar{2}2)$ *and*$(20\bar{2}1)$ *semipolar AlGaN heterostructures.* Appl. Phys. Express **3**, 111002, 2010.

[Zha10a] Y. Zhao, J. Sonada, I. Koslow, C.-C. Pan, H. Ohta, J.-S. Ha, S.P. DenBaars, S. Nakamura. *Optimization of device structures for bright blue semipolar* $(10\bar{1}\bar{1})$ *light emitting diodes via metalorganic chemical vapor deposition.* Jpn. J. Appl. Phys. **49**, 070206, 2010.

[Zha10b] Y. Zhao, J. Sonoda, C.-C. Pan, S. Brinkley, I. Koslow, K. Fujito, H. Ohta, S.P. DenBaars, S. Nakamura. *30-mW-class high-power and high-efficiency blue semipolar* $(10\bar{1}\bar{1})$ *InGaN/GaN light-emitting diodes obtained by backside roughening technique.* Appl. Phys. Express **3**, 102101, 2010.

[Zha11] Y. Zhao, S. Tanaka, C.-C. Pan, K. Fujito, D. Feezell, J.S. Speck, S.P. DenBaars, S. Nakamura. *High-power blue-violet semipolar* $(20\bar{2}\bar{1})$ *InGaN/GaN light-emitting diodes with low efficiency droop at* $200\,A/cm^2$. Appl. Phys. Express **4**, 082104, 2011.

A. Publications

1 M. Knab, M. Hocker, T. Felser, I. Tischer, J. Wang, F. Scholz, K. Thonke. *EBIC investigations on polar and semipolar InGaN LED structures.* Phys. Status Solidi B **253**, 126, 2016.

2 R.A.R. Leute, D. Heinz, J. Wang, T. Meisch, M. Müller, G. Schmidt, S. Metzner, P. Veit, F. Bertram, J. Christen, M. Martens, T. Wernicke, M. Kneissl, S. Jenisch, S. Strehle, O. Rettig, K. Thonke, F. Scholz. *Embedded GaN nanostripes on c-sapphire for DFB lasers with semipolar quantum wells.* Phys. Status Solidi B **253**, 180, 2016.

3 F. Scholz, M. Caliebe, G. Gahramanova, D. Heinz, M. Klein, R.A.R. Leute, T. Meisch, J. Wang, M. Hocker, K. Thonke. *Semipolar GaN-based heterostructures on foreign substrates.* Phys. Status Solidi B **253**, 13, 2016.

4 J. Wang, T. Meisch, D. Heinz, R. Zeller, F. Scholz. *Internal quantum efficiency and carrier injection efficiency of c-plane,* $\{10\bar{1}1\}$ *and* $\{11\bar{2}2\}$ *InGaN/GaN-based light-emitting diodes.* Phys. Status Solidi B **253**, 174, 2016.

5 R.A.R. Leute, J. Wang, T. Meisch, J. Biskupek, U. Kaiser, F. Scholz. *Blue to true green LEDs with semipolar quantum wells based on GaN nanostripes.* Phys. Status Solidi C **12**, 376, 2015.

6 J. Wang, Y. Gao, S. Alam, F. Scholz. *Mg doping of 3D semipolar InGaN/GaN-based light emitting diodes.* Phys. Status Solidi A **211**, 2645, 2014.

7 SK.S. Rahman, R.A.R. Leute, J. Wang, T. Meisch, M. Klein, F. Scholz, K. Koyama, M. Ishii, H. Takeda. *LEDs on HVPE grown GaN substrates: Influence of macroscopic surface features.* AIP Advances **4**, 077119, 2014.

8 R.A.R. Leute, D. Heinz, J. Wang, F. Lipski, T. Meisch, K. Thonke, J. Thalmair, J. Zweck, F. Scholz. *GaN based LEDs with semipolar QWs employing embedded sub-micrometer sized selectively grown 3D structures.* J. Cryst. Growth **370**, 101, 2013.

9 B. Neuschl, J. Helbing, K. Thonke, T. Meisch, J. Wang, F. Scholz. *Optical absorption of polar and semipolar InGaN/GaN quantum wells for blue to green converter structures.* J. Appl. Phys. **116**, 183507, 2014.

10 J. Wang, D. Zhang, R.A.R. Leute, T. Meisch, D. Heinz, I. Tischer, M. Hocker, K. Thonke, F. Scholz. *InGaN/GaN based semipolar green converters.* J. Cryst. Growth **370**, 120, 2013.

11 T. Wunderer, M. Feneberg, F. Lipski, J. Wang, R.A.R. Leute, S. Schwaiger, K. Thonke, A. Chuvilin, U. Kaiser, S. Metzner, F. Bertram, J. Christen, G.J. Beirne, M. Jetter, P. Michler, L. Schade, C. Vierheilig, U.T. Schwarz, A.D. Draeger, A. Hangleiter, F. Scholz. *Three-dimensional GaN for semipolar light emitters.* Phys. Status Solidi B **248**, 549, 2011.

12 T. Wunderer, J. Wang, F. Lipski, S. Schwaiger, A. Chuvilin, U. Kaiser, S. Metzner, F. Bertram, J. Christen, S. S. Shirokov, A. E. Yunovich, F. Scholz. *Semipolar GaInN/GaN light-emitting diodes grown on honeycomb patterned substrates.* Phys. Status Solidi C **7**, 2140, 2010.

B. Curriculum Vitae

CV was removed for data privacy protection reasons.

C. Acknowledgements

Acknowledgements were removed for data privacy protection reasons.

C. Acknowledgements

Acknowledgements were removed for data privacy protection reasons.